Università degli Studi di Napoli "Federico II"

PhD on Novel Technologies for Material, Sensors and Imaging

XXII cycle

Development of a Multiparametric Lidar with the Depolarization Sensor

Libera Nasti

Coordinator
Prof. Antonello Andreone

Tutor
Prof. Nicola Spinelli
Co-tutor
Dr.Xuan Wang

College year 2008/2009

Contents

Introduction

The topic of this work was the design, the realization and the calibration of the depolarization sensor added in the Napoli Lidar (Light Detection and Ranging) system. In addition a complete rebuilding of the receiving system was operated, and a new characterization of all the components of the apparatus was done.

From the advent of Lidar technology in 1970 the study of the composition of the atmosphere gets a speed up. Lidar is an active sensor that sends into the atmosphere a short laser pulse and measures the elastic and Raman shifted optical backscattered power from molecules and aerosols. From the delay of the received pulse, the position of the scattering elements is obtained. Analyzing the backscattered radiation some important optical properties of the atmospheric aerosols can be derived: backscattering and extinction coefficients, position and altitude of the layers, colour index and so on.

In this context, a depolarization-sensitive Lidar can help to characterize the particle's shape. The discrimination of the shape of the aerosols is very important, for example to distinguish the phase of the clouds (ice-clouds are strongly asymmetric scatterers while low clouds are made by spherical water's drops) and the type of aerosols (Saharan dust is constituted by non-spherical particles while urban aerosols by little spherical particles).

The depolarization measurements can be performed by using a linearly polarized laser source and a hardware configuration of the receiving system including two channels detecting simultaneously the backscattered radiation in the parallel and orthogonal direction with respect to the laser beam.

The total depolarization ratio, due both to molecular and aerosol contributions, is simply the calibrated ratio of the orthogonal signal to the parallel one. So, a key question to obtain high quality depolarization measurements is performing a good calibration of the Lidar system.

In this work different calibration techniques were analyzed by simulating lidar signals in different atmospheric conditions. In Napoli the sensor was realized and then calibrated while in Potenza the depolarization sensor was only calibrated. These two systems were calibrated with different techniques, due to different apparatus conditions.

My scientific activity was spent for the most in the Atomic and Laser Applications Laboratory in Physics Department of University Federico II of Napoli.

A period of three months was also spent in C.N.R.-I.S.A.C.(Istituto di Scienze Atmosferiche e Climatiche), in Bologna, where some theoretical models about the atmospheric dynamic were developed. Two months period was also spent in C.N.R.-I.M.A.A. (Istituto di Metodologie per l'Analisi Ambientale- Tito Scalo-Potenza), working under the supervision of Dr. Gelsomina Pappalardo.

Chapter 1

Atmospheric aerosols and their interactions with the radiation

In this chapter a brief classification of the aerosols present in atmosphere will be done. Then, the interactions radiation-aerosols will be described, including elastic and inelastic processes, and a particular attention will be devote to the depolarization effect on the scattered radiation induced by different kinds of particulate.

1.1 Aerosols

The aerosols are liquid or solid particles of matter suspended in a gas. In the case of atmospheric aerosols they can be distinguished in different classes, depending on their origin, constitution, dimensions, shape, mass and chemical composition. In fig.1.1 a rough classification is presented as a function of their dimensions:

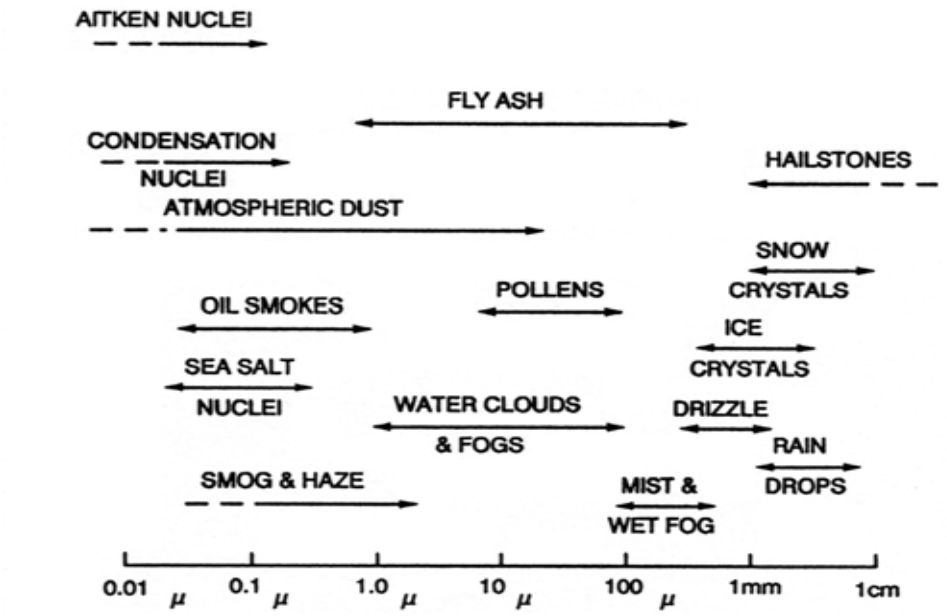

Fig.1.1 Classification of the aerosols as a function of their dimensions

The global cycle of the aerosols is: emission from the surface, permanence or transport in the atmosphere, possible changes in nature and in the composition after cross, chemical or photochemical reactions, and then fall down.

The principal sources of aerosols are: vegetal transpiration, marine salts, desertic dust, fossil combustion products, biomass combustion products, biogenic and anthropic VOC (Volatile Organic Compounds), interplanetary dust and volcanic ash. Some sources can be predominant with respect to others, depending on which hemisphere of the world we are, and if we are dealing about a urban or a rural site.

The aerosols have particular properties from different points of view:

- Optical: they act as scattering elements and reflect part of the incident solar radiation, and can cause a net effect of cooling toward the climate of earth surface;
- Chemical-Physical: they influence some important reactions occurring in the atmosphere;
- Toxicological: they act collecting pollutants on their surface, and the smallest ones, easily inhaled, favour the input of the pollutants into the live organisms.

We can group the aerosols in two principal categories: the *dust* and the *igroscopic particles.*

In the category of *dust* we include the aerosol constituted by mineral of various nature: interplanetary rubble, volcanic ash, industrial residues, desertic and erosion powders.

The igroscopic particles are aerosols that can act as condensation-nuclei of water vapour, of different dimensions. According to Junge classification [1.1], these nuclei can be divided in three categories as a function of their dimensions:

- Aitken nuclei, with a radius smaller than $0.1\mu m$;
- Large nuclei, with a radius between 0.1 and 1 μm ;
- Giant nuclei, with a radius greater than 1 μm .

The formation mechanism of the clouds promoted by these aerosols can be schematically represented as follows: a dry aerosol containing soluble compounds becomes humid when the relative humidity increases, forming a film on the boundary until the real drop is created.

Inside the category of igroscopic particles there are the organic aerosols of vegetal origin, organic and inorganic ash, particles derived by photochemical reactions between the combustion and atmospheric gases like the sulphur bioxide and the nitrogen dioxide, the marine salt particles like the crystals of sodium chloride, calcium sulphate and magnesium.

The removal mechanisms of the aerosols from the atmosphere can be classified in the following forms:

- Coagulation: it happens when two particles collide giving rise to a lower number of bigger particles;
- Sedimentation: fall down of the particles;
- Wash-out: removal of the particle caused by rain or snow.

1.2 Aerosols-radiation interactions

The aerosols-radiations interactions cover a wide range of physical phenomena concerning the physics of matter. Most of them can be classified as absorption processes or scattering processes that can be also divided in elastic (Rayleigh and Mie) and inelastic (Raman) scattering processes. From the scattered radiation some important information, concerning the target elements, can be retrieved. Lidar technique, as an active remote sensing technology, uses the scattered light to retrieve important information on the nature and on the vertical distribution of the scatter elements, aerosols and molecules, present in the atmosphere.

1.2.1 Absorption process

To examine the absorption process, let's consider a beam of monochromatic light of wavelength λ and intensity $I(\lambda)$ that propagates in the z direction. The intensity of the radiation will be attenuated going through the atmospheric layer of depth dz, due to the absorption and the scattering by molecules and aerosols. The corresponding change of the intensity is expressed by the following relation:

$$dI(\lambda) = -\alpha(\lambda, z) \cdot I(\lambda) \cdot dz \tag{1.1}$$

Where:

- The negative sign indicates the attenuation of the beam;
- α is known as the extinction or attenuation coefficient, and it express the reduction of the energy flux for unity of length in the direction of propagation of the light beam. It represents the total attenuation of the beam intensity caused both by the absorption and by the scattering. Dimensionally it is the inverse of a length $\left[L^{-1}\right]$.

Integrating the expression (1.1) between the altitude $z = 0$ and z, we obtain a law very common in the remote sensing, well-known as the *Lambert-Beer law,* that describes the trend of the intensity of a plane monochromatic wave going through the atmosphere as a function of the altitude:

$$I(\lambda, z) = I_o \exp\left[-\int_0^z \alpha(\lambda, z')dz'\right] \tag{1.2}$$

Where:

- I_0 is the intensity of the radiation at the altitude $z = 0$, or $I(\lambda,0)$;
- $\int_0^z \alpha(\lambda, z)dz$ is known as the optical depth of the medium, that, in general, can be indicated as $\int_0^z \left(\sum_i N_{a,i}\sigma_{a,i} + \sum_j N_{s,j}\sigma_{s,j}\right)dz$, where $N_{a,i}(N_{s,j})$ is the numerical densities of the ith absorption specie (jth scattered specie) and $\sigma_{a,i}(\sigma_{s,j})$ the relative cross-sections.

From the ratio between the intensities $I(\lambda, z)$ and $I_o = I(\lambda, 0)$, we can obtain another important parameter to characterize the optical proprieties of the atmosphere: the *atmospheric trasmittivity* :

$$T(\lambda, z) = \exp\left[-\int_0^z \alpha(\lambda, z)dz\right] \tag{1.3}$$

This parameter gives information about the optical density of the atmosphere and therefore about the capability of the atmosphere in transmitting over a certain range, a determined wavelength.

Estimation of the transmissivity and in particular of the optical depth gives informations about the concentration of the scattered and absorption components. The following figure shows the absorption bands of the main components of the atmosphere as a function of the wavelength:

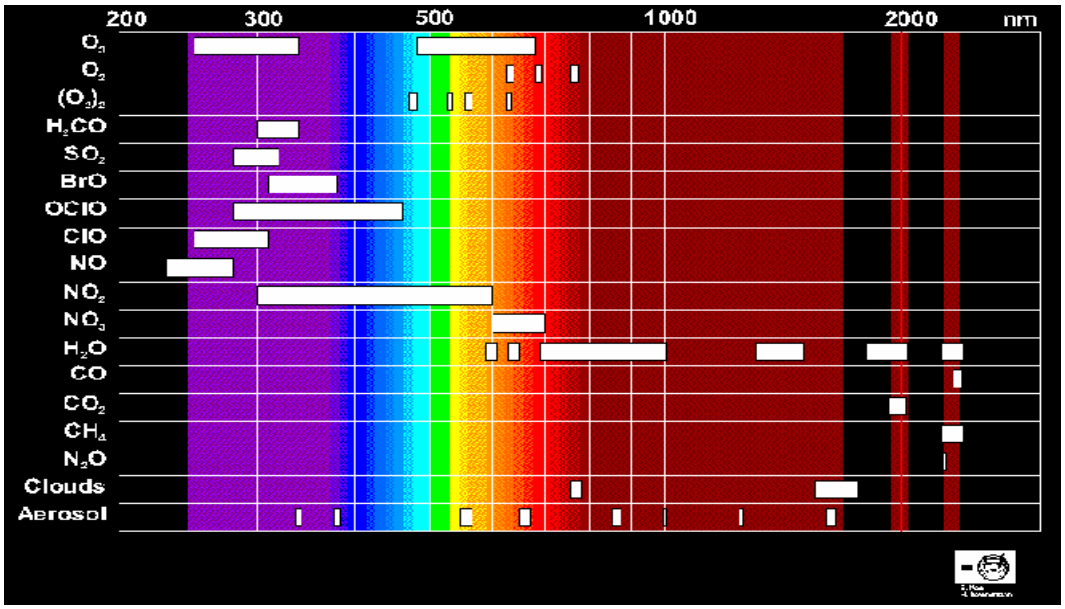

Fig.1.1 Absorption of the atmospheric constituents in function of the wavelength

1.2.2 Scattering process

The scattering process is the physical phenomenon by which a particle that is posed along the path of an electromagnetic wave first subtracts energy from the incident wave, and then irradiates it within the total solid angle targeted in the particle position.

This process really happens if the refraction index of the particle is different from that one of the surrounding media, in this way the particle constitutes a discontinuity for the incident wave.

The physical principle of the scattering can be explained trough the electromagnetic theory [1.2]. The electromagnetic field induces an oscillation of the electrons of the particle at the same frequency of the incident wave. Oscillating charges (dipoles) radiate electromagnetic

waves. If these electromagnetic waves are at the same frequency of the incident electromagnetic wave, these waves are said to be *elastically* scattered and the scattering is said to be *elastic*, or, if the scattered waves have different wavelength these waves are said to be *anelastically* scattered and the scattering is said to be *inelastic*.

The shape of the spatial distribution of the scattered field depends on the relation between the incident wavelength and the dimension of the scattered centre, while the symmetry properties with respect to the direction of the incident wavelength are linked to the isotropy of the scattered particle.

As we previously saw, the atmospheric particles are very different for dimensions, distribution and optical properties. This makes extremely complex and various the scattered properties (angular dependence and intensity of the scattered radiation), in particular when the dimensions of the scattered centre are comparable to the wavelength of the incident radiation. In order to simplify the treatment it is useful to introduce a parameter x, linked to the relative dimensions of the scattered particle and the wavelength of the incident radiation, defined as:

$$x = \frac{2\pi}{\lambda} a = ka \tag{1.4}$$

Where a represents the linear dimension of the particle and λ the incident wavelength.

According to (1.4), the shape of the distribution is influenced by the ratio between the refractive index of the particle and that one of the medium.

The *x* parameter influences strongly the shape of the distribution of the scattered field. If the dimensions of the particles are very smaller than the wavelength of the incident wave $x << 1$, the scattered radiation field is almost uniformly distributed around the particle and the dominating scattering process is described by the Rayleigh theory. As the dimensions of the particles grow up, a forward peak appears in the direction of the propagation of the wave and the distribution of the wave loses its symmetry (increasing the ratio between the forward intensity and the backward intensity), until it become independently on the wavelength, when the dimensions of the particles are much bigger than λ. Under these circumstances the Mie theory gives a suitable description of the scattering processes. The situation is schematically represented in fig. 1.2:

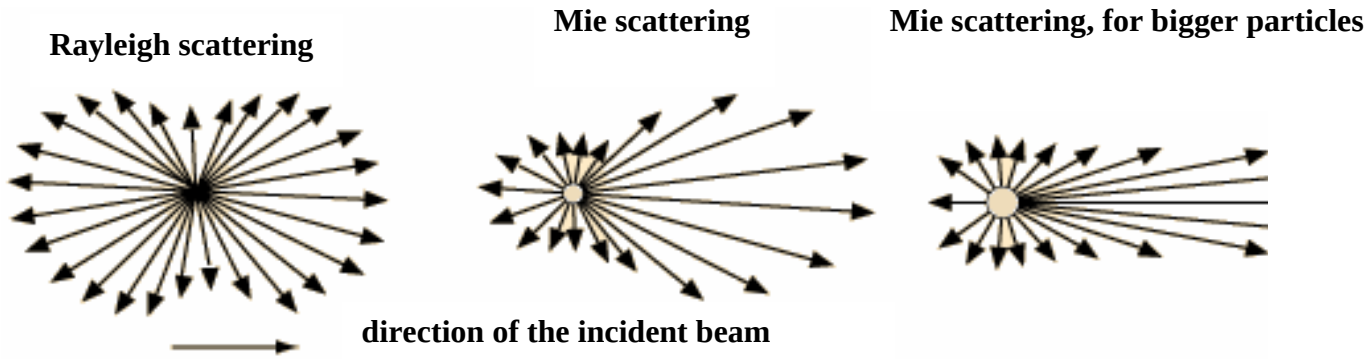

Fig. 1.2 Angular distribution of the scattered radiation varying the x parameter

In the following, three typologies of scattering will be described in detail, distinguished as a function of the dimension *a* of the particle and of the wavelength λ of the incident radiation.

If $a << \lambda$, the scatter process is described by the Rayleigh theory, from the name of the physics who first described the scattering properties by small particles.

In this process the scattering intensity in this process varies with the square power of the volume of the particle and is inversely proportional to the fourth power of the wavelength.

In the atmosphere, the principal scattering agents are the gas molecules. The second kind of scattering refers to particles dimensions comparable to the wavelength of the incident wave, and is described by the Mie theory. Although this theory is strictly applicable only to isotropic spheres, it is possible to extend the treatment also to particles of irregular shapes, with some corrections.

The complete theory is based on a development in series, and the first term corresponds to the Rayleigh scatter process.

A third typology of scattering is the Raman scattering, producing scattered radiation at a wavelength slightly different from the incident one. The Raman scattering is easily detectable if the incident beam is monochromatic: in the scattered radiation, peaks at different frequencies with respect to that one of the incident wave appear, corresponding to the rotovibrationals transitions of the target molecules.

1.3 Rayleigh theory

Let's assume the single molecule as a dielectric and isotropic sphere, of linear dimension much lower then the wavelength of the incident radiation. The molecule interacts with the primary wave, subtracting energy and scattering it around the space. Let's consider an ideal model, in which the molecular mass is concentrated in the atomic nucleus, placed in the centre, with a positive charge, while the electronic cloud, shared with the atoms constituting the molecule, balances the charge.

The attraction between charges of opposite sign constitutes an elastic attractive force.

When the molecule is subjected to an electric field, the charges are subjected to a forced oscillation and it will be created an induced moment of dipole $\vec{p}$, that oscillates in resonance and parallel to the incident electromagnetic field. The scattering phenomenon is based just on the polarizability of the molecule.

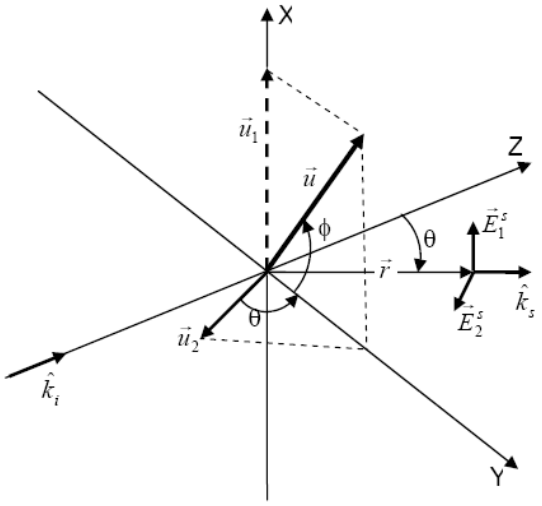

Fig.1.3 Scheme of the elastic Rayleigh scattering

In fig.1.3 the Rayleigh scattering scheme is represented: the molecule is placed in the origin of the reference system OXYZ. When it is invested by an incident electromagnetic field $\overrightarrow{E_i}$, linearly polarized along $\vec{u}$ direction, that propagates along $\overrightarrow{k_i}$ direction, the molecules produces a dipole momentum: $\vec{p} = q\vec{\delta}$, where:

- q represents the charge displaced by the effect of the incident field (in the following it is considered the simple case $q = e$);
- $\vec{\delta} = \delta \hat{u}$ represents the displacement of the charge from its equilibrium position due to the effect of the incident field.

With reference to the figure 1.3 it's possible to write $\vec{p}$ in term of its components:

$$p_x = e\delta_x = \left[\frac{e^2}{m(\omega_0^2 - \omega^2)} E_0 \sin \omega t \right] \sin \phi \tag{1.5}$$

$$p_y = e\delta_y = \left[\frac{e^2}{m(\omega_0^2 - \omega^2)} E_0 \sin \omega t \right] \cos \phi \tag{1.6}$$

Where:

- δ_x and δ_y are the solutions of the forced oscillations equation of the single electronic charge along *x* and *y* and constitute the response of a bound electron to the field $\vec{E_i}$ incident on to the molecule;
- E_0 is the amplitude of the electric field incident on the molecule;
- *e* and *m* are the electronic charge and mass, respectively;
- ω_0 is the resonance frequency, equal to $\omega_0 = \left(\frac{e^2}{4\pi\varepsilon_0 r^3 m} \right)^{\frac{1}{2}}$, with r the radius of the electronic shell;
- ω is the frequency of the incident electromagnetic field.

The oscillating dipole, produced by the incident wave, generates a secondary wave, whose electric field at large distance $\left(R \gg \frac{\lambda}{2\pi} \right)$, is given by the following expression:

$$\vec{E}_s = \frac{-e}{4\pi\varepsilon_0 c^2 R} \left[\hat{k}_s \times (\hat{k}_s \times \vec{u}) \right] \tag{1.7}$$

Where:

- $\vec{k}_s = \frac{2\pi}{\lambda} \hat{k}_s$ defines the propagation vector of the scattered field;

- $\vec{u}$ is the instantaneous acceleration of the electric dipole, at the delayed time $(t - R/c)$, whose explicit expression is obtained deriving the solution of the forced oscillation of the single charge equation two times with respect to the time.

Inserting the expression for $\vec{u}$ in the previous equation, it stands that:

$$\vec{E}_s = \frac{\omega^2 p_0}{4\pi\varepsilon_0 c^2 R} \sin\omega(t - R/c)\left[\hat{u}_2 \cos\vartheta\cos\phi + \hat{u}_1 \sin\phi\right] \tag{1.8}$$

Where:

- $p_0 = \frac{e^2}{m(\omega_0^2 - \omega^2)} E_0$ is the maximum value of the momentum dipole;
- ϑ is the scattering angle, or the angle between the $\vec{k}_i$ direction of the incident wave and the direction $\vec{k}_s$ of the scattered wave in the scattering plane YZ;
- ϕ is the polarizing angle of the incident field;
- $\hat{u}_1$ and $\hat{u}_2$ are orthogonal unit vectors, that represent the directions of the components of the acceleration $\vec{u}$ in the plane orthogonal to the scattering direction (parallel and orthogonal components with respect to the scattering plane);
- R is any distance along the scattering direction.

From (1.8) it is possible to get the expression of the mean power radiated per unit of wavelength and per unit of area orthogonal with respect to the direction of propagation, or the mean spectral irradiance, induced by the scattered field at the distance R, defined by the Poynting's vector averaged over an optical period of $2\pi\omega^{-1}$, [Watt m^{-2}]:

$$\overline{S} = \frac{1}{2} c\varepsilon_0 E_{os}^2 \tag{1.9}$$

Where E_{os} is the amplitude of the scattered field.

From the expression (1.8) we get:

$$\overline{S} = \frac{\pi^2 c}{2\varepsilon_0 \lambda^4 R^2}\left[\frac{e^2}{m(\omega_0^2 - \omega^2)}\right]^2 E_0^2\left[\cos^2\phi\cos^2\vartheta + \sin^2\phi\right] \tag{1.10}$$

Usually the atmospheric scattering is described in term of radiance $J(\vartheta,\phi)$, defined as the radiative power per unit of solid angle and per unit of area $[Watt \cdot sr^{-1} \cdot m^{-2}]$. This quantity has the advantage to be independent on R and to give an indication of the electromagnetic density of energy radiated by a source. As $\overline{S} = J/R^2$, it results: $J = \overline{S}R^2$, or from (1.10):

$$J(\vartheta) = \frac{\pi^2 c}{2\varepsilon_0 \lambda^4}\left[\frac{e^2}{m(\omega_0^2 - \omega^2)}\right]^2 E_0^2\left[\cos^2\vartheta\cos^2\phi + \sin^2\phi\right] \tag{1.11}$$

In the specific case of a plane not polarized wave, it results:

$$J(\vartheta) = \frac{\pi^2 c}{2\varepsilon_0 \lambda^4}\left[\frac{e^2}{m(\omega_0^2 - \omega^2)}\right]^2 E_0^2\left[\cos^2\vartheta + 1\right] \tag{1.12}$$

It's important to focus on the fact that the angular dependence of the scattered light intensity is modulated by the term: $\frac{1}{\lambda^4}$, so a short wavelength light is stronger scattered than the long wavelength light: this is the reason why the sky in the morning appears blue. In addiction, the angular dependence of the intensity of the scattered light is proportional to $(1+\cos^2\vartheta)$ for incident not polarized light. This means that the maximum intensity of the scattered light corresponds to the forward direction ($\vartheta = 0^0$) and the backward direction ($\vartheta = 180^0$) with respect to the incident direction. A useful parameter to describe the scattering is the *angular cross-section,* defined as the surface, on the incident wave-front, crossed by a power equal to that one scattered by the molecule per unit of solid angle, around the angle ϑ. In symbols:

$$\sigma(\vartheta)\overline{S}' = J(\vartheta) \tag{1.13}$$

The angular cross-section is equal to the ratio between the scattered radiance $J(\vartheta)$ and the irradiance of the incident wave, $\overline{S}' = \frac{1}{2}\varepsilon_0 c E_0^2$

Removing in (1.11) and (1.12) the dependence from the frequency ω introducing the square of the complex index of refraction of the medium *n* and utilizing the (1.13), it results, [1.3]:
For incident linearly polarized light:

$$\sigma(\vartheta) = \frac{\pi^2}{N^2\lambda^4}(n^2 - 1)^2[\cos^2\vartheta\cos^2\phi + \sin^2\phi] \tag{1.14}$$

and for incident not polarized light:

$$\sigma(\vartheta) = \frac{\pi^2}{2N^2\lambda^4}(n^2-1)^2[\cos^2\vartheta + 1] \tag{1.15}$$

Where:

- n is the refraction index of the gas;
- N is the number of the oscillating dipoles per unit of volume, or the numerical density of the diffusers;
- λ is the wavelength of the incident and scattered light.

Integrating the (1.14) and the (1.15) over all the solid angle, we get the *total Rayleigh cross section* for a single, isotropic molecule illuminated by linear polarized light:

$$\sigma = \frac{8\pi^3(n^2-1)^2}{3N^2\lambda^4} \tag{1.16}$$

In the remote sensing field it is useful to introduce the *backscattering cross-section*, or that one corresponding to the backward direction of scattering $(\vartheta = 180°)$. It is:

$$\sigma^{\pi}(\lambda) = \frac{d\sigma(\vartheta=\pi)}{d\Omega} = \frac{\pi^2(n^2-1)^2}{N^2\lambda^4} \tag{1.17}$$

That has an order of magnitude of $10^{-28} cm^2 sr^{-1}$ for the visible radiation.

Another important parameter is the *scattering coefficient* β_A, defined as the total intensity subtracted from a beam by a collection of N suspended particles per unit of volume, per unit of irradiance of the volume, or:

$$\beta_A = \sigma N \tag{1.18}$$

And, under the (1.16)

$\beta_A = \frac{8\pi^3(n^2-1)^2}{3N\lambda^4}$, from that we can get for the backscattering coefficient:

$$\beta_A(\vartheta=\pi) = \frac{\pi^2(n^2-1)^2}{N\lambda^4} \tag{1.19}$$

The coefficient $\beta_A(\pi) = \beta$ represents the portion of the incident energy that is backscattered from the atmospheric target, per unit of solid angle and per unit of optical depth $\left[L^{-1}sr^{-1}\right]$.

From the equations (1.17) and (1.19) it results that, if the cross-section is known, one measurements of the *backscattering coefficient* allows determining the targets' density.

This treatment is valid if we consider an atom or a molecule as a single oscillator; this condition is fulfilled if the targets can be considered little with respect to the incident wavelength.

1.4 Mie theory

Mie theory describes the scattering phenomena when the dimensions of the scattered centers are of the order of magnitude of the incident radiation's wavelength. As the linear dimension of the particles grows up, the intensity of the scattered light becomes a complex function of the x parameter, of the refraction index and of the shape of the involved particles. Mie theory can be considered an evolution of the Rayleigh theory, where the distribution of the scattered radiation is uniform around the scattered centre and, as x becomes bigger, this symmetry is lost.

In Mie regime each particle is considered as a composition of many molecules and the scattering from such particle can be examined as an extension of the scattering by one molecule. Invested by the radiation, the molecules constituting the scattering particle, become oscillating dipoles, that generate secondary waves, said partial waves, and their amplitudes constitute terms of a convergent series, which square sum represents the Mie function of the scattered intensity for a specific scattering angle. If the dimension of the particle is comparable with respect to the wavelength, the phase of the primary wave is not uniform around the particle, and this determines a spatial and temporal phase difference between the different partial waves. This produces interference phenomena between the partial waves and induces a variation in the scattered intensity with the angle of scattering. So, an increment in the ratio between the forward intensity and the backward intensity is observed when the dimension of scatterers grows. The geometry of Mie scattering (fig.1.3), can be represented in a reference system OXYZ, where the volume constituted by N particles is put in the origin of the axes. Let's assume that the incident radiation travels in the positive X direction, while the observation direction is given by the straight line OD in XZ plane, at an angle ϑ, the scattering angle, with respect to the X axis. The distance OD between the particle and the detector in D can be considered large enough to neglect the volume occupied by the scattered centres.

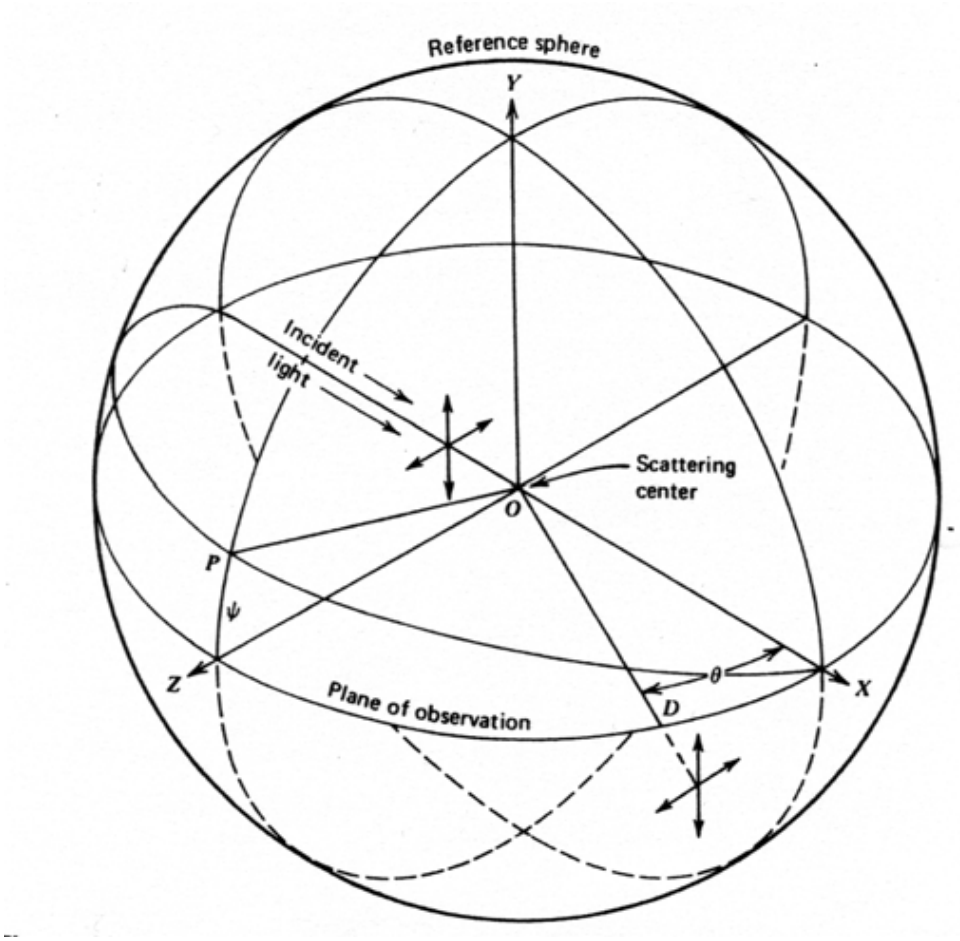

Fig 1.3 Mie scattering geometry

The light scattered by the particle at ϑ angle can be considered as constituted by two components of intensity $I_{\perp}(\theta)$ and $I_{\square}(\theta)$, polarized orthogonal and parallel with respect to the plane of observation XZ, respectively; these components result proportional to the two Mie intensity function distributions, i_1 and i_2. For a spherical and isotropic particle, these are expressed as infinite series of terms, [1.4]:

$$i_1(x,m,\theta) = |S_1|^2 = \left| \sum_{n=1}^{\infty} \frac{2n+1}{n(n+1)} (a_n \pi_n + b_n \tau_n) \right|^2 = |\mathrm{Re}(S_1) + \mathrm{Im}(S_1)|^2$$

$$i_2(x,m,\theta) = |S_2|^2 = \left| \sum_{n=1}^{\infty} \frac{2n+1}{n(n+1)} (a_n \tau_n + b_n \pi_n) \right|^2 = |\mathrm{Re}(S_2) + \mathrm{Im}(S_2)|^2$$

Where:

- x is the characteristic parameter of the particle's dimension;

- m is the complex refraction index of the particle;
- θ is the observation angle (scattering angle);
- S_1 and S_2 are the complex amplitudes of the observed scattering waves, depending only by θ;
- a_n and b_n are complex functions of Riccati-Bessel;
- π_n and τ_n are functions that contain the first and second order derivatives of the Legendre's polynomials of order n.

The Mie theory establishes that the scattering angular cross-section of a particle is:

$$\sigma_p(\vartheta,\phi) = \frac{\lambda^2}{4\pi^2}\left[i_2 \cos^2\psi + i_1 \sin^2\psi \right] \tag{1.20}$$

In symbols: $\sigma_p(\vartheta,\psi) I_i = J_S(\vartheta,\psi)$, where $J_S = I_S R^2$, with I_S the irradiance of the scattered field.

When the particle is irradiated by plane polarized light, with the electric field tilted by a ψ angle with respect to the observation plane XZ (as $\psi < \frac{\pi}{2}$), the intensity of the scattered light in this plane (irradiance) is: $I_s(\vartheta,\psi) = \frac{I_i}{R^2}\frac{\lambda^2}{4\pi^2}(i_1(\vartheta)\sin^2\psi + i_2(\vartheta)\cos^2\psi)$. (1.21)

In the two extreme cases, where the electric field makes an angle $\psi = \frac{\pi}{2}$ and $\psi = 0$ with XZ plane, the scattered intensity in this plane is given by the following expressions, respectively:

$$I_{s,\parallel}(\vartheta,\psi) = \frac{I_i}{R^2}\frac{\lambda^2}{4\pi^2} i_2(\vartheta)\cos^2\psi \quad ; \quad I_{s,\perp}(\vartheta,\psi) = \frac{I_i}{R^2}\frac{\lambda^2}{4\pi^2} i_1(\vartheta)\sin^2\psi \tag{1.22}$$

These quantities represent the components of the scattered intensity, polarized in the parallel and in orthogonal directions respectively. For the not-polarized case, the scattered intensity has the following expression:

$$I_s(\theta,\psi) = \frac{I_\perp(\theta,\psi) + I_\parallel(\theta,\psi)}{2} = \frac{I_i}{R^2}\frac{\lambda^2}{4\pi^2}\left(\frac{i_1 + i_2}{2}\right) \tag{1.23}$$

and the angular cross-section is given by:

$$\sigma_p(\theta) = \frac{I_{\perp}(\theta) + I_{\square}(\theta)}{2I_i} = \frac{\lambda^2}{4\pi^2}\left(\frac{i_1 + i_2}{2}\right) \tag{1.24}$$

I_i is the irradiance of the incident light.

The treatment until now done concerns the scattering of a monochromatic and plane wave by a homogeneous and spherical particle in a homogeneous medium, and for this case the Mie theory leads to a rigorous solution. In particular if we observe the light backscattered by a homogenous sphere from a linearly polarized wave, we can see no-change in the polarization properties (this means no-change in the polarization direction). If the scattering centre differs from a sphere, a depolarization in the backscattered light appears.

The real case is much complex, as the real atmosphere is characterized by scattering agents that differ for composition, shape and dimensions, and therefore it is necessary to consider a polidispersion of homogeneous spheres, as a generalization of the solution. In this case, the concentration *N* of the diffusers is substituted by a distribution function. Considering the total volume backscattering coefficient, defined as the total intensity removed from a beam of light by a unit of volume of suspended particles, per unit of irradiance of the volume, and taking into account the different cross-section of the particles, it results, for the polydispersive case:

$$\beta_p(\theta) = \int_{r_1}^{r_2} N(r)\sigma_p(\theta, r)\,dr \tag{1.25}$$

Where $N(r)dr$ represents the number of particles characterized by an index of refraction *n,* having a radius between *r* and *r+dr,* and the limits of integrations define the interval of variability of the radius for the distributions of the scattering elements.

The principal difference between the elastic scattering from molecules and from particles is in the order of magnitude of the cross section: the dielectric spheres of radius much bigger than the dimensions of the molecules have bigger cross-sections.

1.5 Raman scattering

Raman scattering is a-non linear optical process producing in the spectra of the scattered radiation, bandwidths shifted with respect to the incident frequency, of a quantity corresponding to the rotovibrationals frequencies of the target molecule.

Rotovibrationals frequencies between molecular levels are strictly dependent on the kind of chemical bonds between the atoms constituting the molecule, therefore the Raman scattering allows to distinguish the specific molecular target, throw the study of its specific rotovibrationals spectra. Hitting a gas sample with a monochromatic radiation of frequency ν, the molecule feels a transition from an initial state $|m\rangle$ to an intermediate virtual state $|j\rangle$. If this excited state is not stationary, the molecule decays to the final state $|n\rangle$ through a radiative relaxation. If the state $|n\rangle$ coincides with the initial state $|m\rangle$, a radiation of the same frequency of the incident one is emitted, (again Rayleigh scattering), otherwise we go to the Raman case. In this case, indicating with v the vibrational quantum number, it's possible to distinguish two possible transitions relative to the situation in which the final state of the molecule is a vibration state immediately up or down with respect to the initial state. In the first case ($\Delta V = +1$), we can speak of anti-Stokes process, in the other case, ($\Delta V = -1$), we can speak of Stokes process.

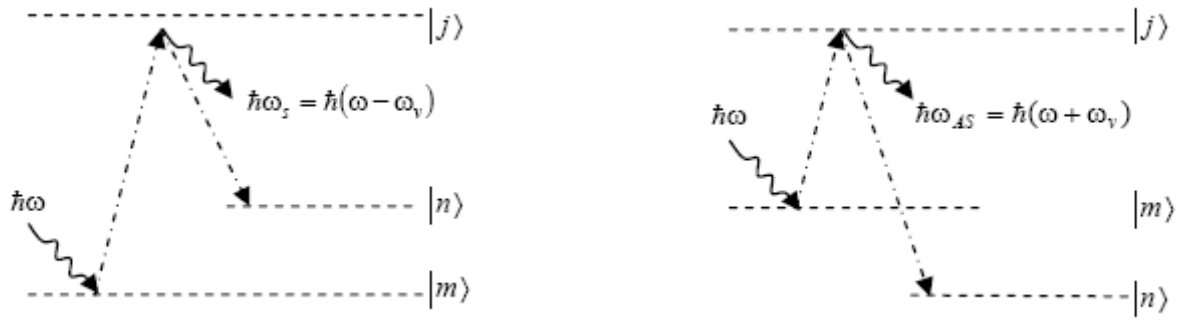

Fig.1.4 a) Stokes process b) Anti-Stokes process

The Stokes lines correspond to the case in which the energy of the final state $|n\rangle$ is higher with respect to the one of the initial state $|m\rangle$; the anti-Stokes lines correspond to the opposite case.

Obviously, the intensities of the two kinds of lines depend on the distribution of the population of the energy levels and the Stokes lines are more intense than the anti-Stokes ones because the highest levels are less populated.

Together with the variation of the vibrational states it's necessary to consider the variation of the rotational spectra. If we indicate with J the rotational quantum number, the allowed transactions, for a biatomic molecule, are those corresponding to $\Delta J = 0, \pm 2$.

Therefore, the Raman spectrum is composed by three branches:

1. the S branch, correspondent to $\Delta J = +2$;
2. the Q branch, correspondent to $\Delta J = 0$;
3. the O branch, correspondent to $\Delta J = -2$.

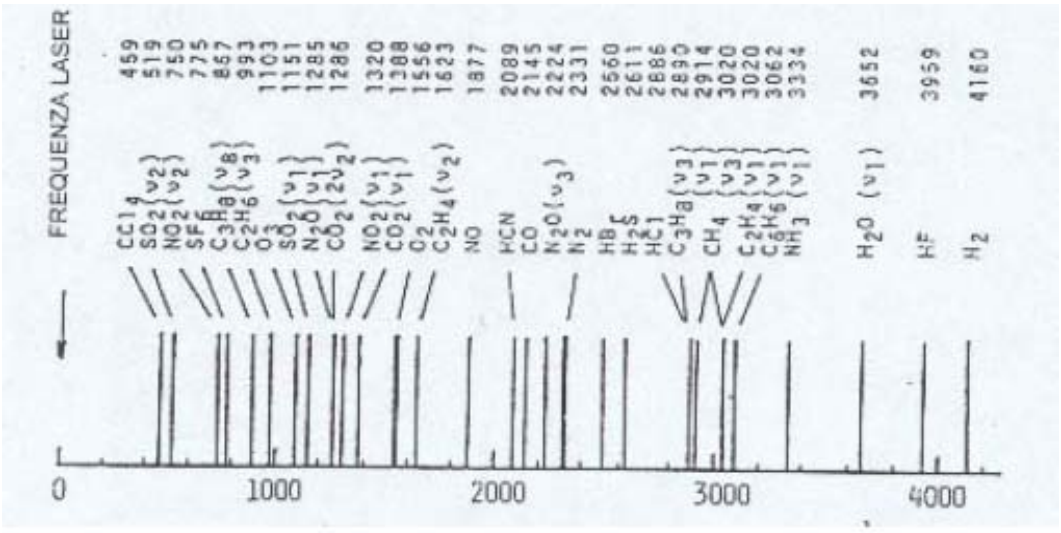

Fig.1.5 Frequency-shift of the Q-branch of the vibrational Raman spectra, of molecules typically present in the atmosphere

1.6 Conclusion

In this chapter the principal phenomena of interactions of light beams with the atmosphere relevant for the optical remote-sensing have been discussed.

The most relevant phenomena we have seen are the elastic interaction between radiation and matter described by the Rayleigh and Mie theories (depending by the relative dimensions of the scatter elements and the wavelength of the radiation), and the inelastic Raman scattering.

1.7 References

[1.1] C.E.Junge, *Air chemistry and Radioactivity,* Academic Press, New York,1963

[1.2]M.Born and E.Wolf, *Principle of Optics,* 3d ed., Pergamon, Oxford, 1965

[1.3] R. Measure, *Laser Remote Sensing: Fundamental and Applications*

[1.4] T.G.Klyne, *Atmospheric Transmission, Emission and Scattering,* Pergamon Press

Chapter 2

Lidar technology as a reliable tool to obtain aerosol optical properties

In this chapter it is presented the Lidar technology and the advantages of its use in the atmospheric monitoring. It is introduced the Lidar equation describing the response of a Lidar apparatus to the atmospheric processes considered in this thesis under the hypothesis of single scattering and some inversion algorithms of this equation are presented allowing the retrieval of the aerosol optical parameters characterizing the investigated atmosphere (extinction and backscattering coefficients).

2.1 The Lidar technique

From the advent of Lidar (Light Detection and Ranging) in 1970s the study of the composition of the atmosphere gets a speed up.

Lidar is an active sensor that sends into the atmosphere a short laser pulse and measures the elastic and Raman shifted optical backscattered power from molecules and aerosols (see fig.2.1).

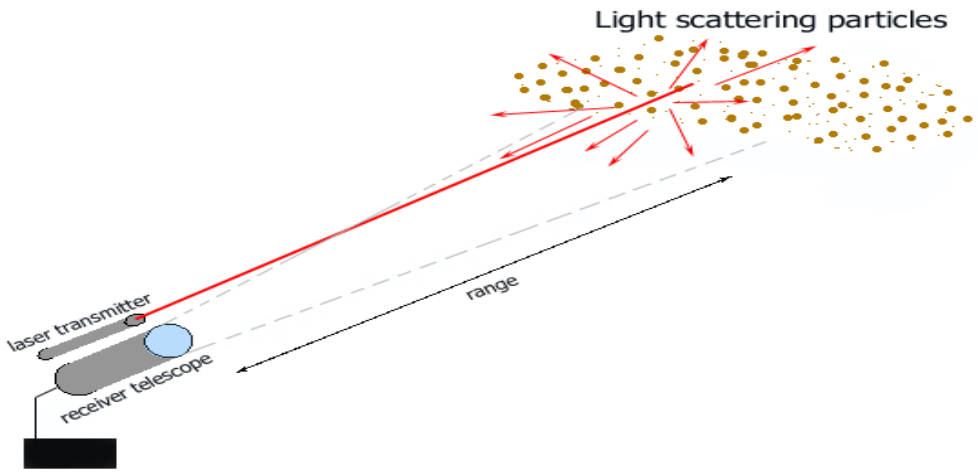

Fig.2.1 Simple scheme of a Lidar optical

From the delay of the received pulse, the position of the scattering element is obtained from the formula: $z = \frac{ct}{2}$, where z is the altitude of the scattering element, c is the speed of the light and t is the time between the sent and the returned pulse. The backscattered optical power is recorded as a function of the time, and therefore of the altitude, obtaining in this way the vertical profiles of atmospheric parameters with a spatial resolution that is linked to the pulse duration of the laser.

The Lidar technique consists in sending into the atmosphere an intense monochromatic laser pulse which is scattered in all directions by the molecules and the aerosol particles suspended in the atmosphere. This scattering process is essentially caused by $N_{2,}$ O_2 and H_20 (Rayleigh and Raman scattering) and by the aerosol particle suspended in the atmosphere (Mie scattering). The fraction of radiation that is backscattered to Lidar station is called the Lidar signal. This signal is collected by a telescope and detected by a series of photomultipliers, after the separation of the different wavelengths.

The intensity of the received signal depends on the backscattering and absorption properties of the investigated atmosphere.

Several relevant optical proprieties of the atmospheric aerosols can be derived by analyzing the backscattered radiation.

2.2 The Lidar equation

As soon as the light pulse is sent into the atmosphere, it propagates and it is progressively attenuated by the molecular absorption and by the scattering processes of Rayleigh, Raman and Mie. The Lidar equation describes the detected signal and represents the relation between the optical signal, the parameters connected to the scattering and the absorption of the laser pulse and the instrumental parameters.

With the intent to obtain the formal expression of the equation, in the following all the different factors that modify the laser pulse that is sent into the atmosphere are discussed.

Let’s consider a Lidar system in a monostatic configuration, this means that the axis of the telescope and of the laser overlap, so the field of view of the telescope includes the divergence of the laser. Let’s suppose, also, the working conditions are those of single scattering, which is a reasonable hypothesis in clear sky condition.

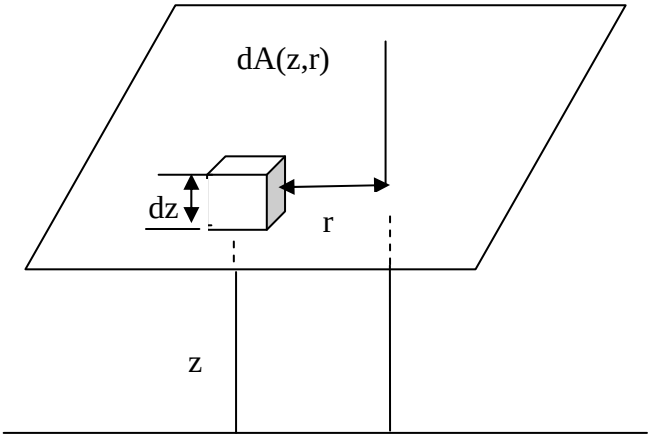

Fig2.2 Scheme of receiving process of the backscattering radiation

According to fig.2.2 the power collected by the receiving system, in the spectral width $[\lambda, \lambda + d\lambda]$, from an atmospheric cell between $[z, z + dz]$, is given by the following equation:

$$P(\lambda, \lambda_L, z) = \int J(\lambda, \lambda_L, z, r) \cdot \Delta\lambda \cdot \Delta z \cdot p(\lambda, z, r) \cdot dA(z, r) \tag{2.1}$$

Where:

- λ is the detected wavelength and λ_L is the laser wavelength;
- $\Delta\lambda$ is the observed bandwidth;
- $J(\lambda, \lambda_L, z, r)$ is the spectral radiance at wavelength λ, of an atmospheric volume at r position and at a height z, induced by the laser radiation, in the orthogonal plane of the beam propagation, for a unitary distance interval;
- $p(\lambda, z, r)$ is the probability that the radiation at λ wavelength from $dA(z, r)$ will reach the detector

The probability $p(\lambda, z, r)$ depends on the attenuation phenomena, the optical properties of the receiving system, the transmissivity of the spectral selection system and also on the geometry of the detection system. It can be written as:

$$p(\lambda, z, r) = \frac{A_o}{z^2} \cdot T(\lambda, z) \cdot \xi(\lambda) \cdot \chi(z, r) \tag{2.2}$$

Where:

- A_o is the area of the telescope. $\frac{A_o}{z^2}$ represents the solid angle of the scattered light, in all directions from the altitude z and intercepted by the receiver
- $\xi(\lambda)$ is the total efficiency, optical and electrical, of the detected channel at λ wavelength
- $\chi(z,r)$ is the overlap factor, depending on the geometry of the apparatus. It represents the probability that the radiation coming from r, at a z distance, is effectively detected by the system, supposed that this depends only by the overlap of the laser beam with the field of view of the telescope
- $T(\lambda,z)$ is the atmospheric transmissivity at λ and at z altitude; it has the following expression $T(\lambda,z)=e^{-\int_0^z \alpha(z')dz'}$, where $\alpha(\lambda,z)$ is the extinction coefficient, defined as the reduction of the energy flux for unity of length in the direction of propagation of the beam flux [L^{-1}].

It's useful to point here that the spectral radiance $J(\lambda,\lambda_L,z,r)$ depends on the kind of interaction between the radiation and the target.

Because the kind of interaction that we are studying here is the elastic or inelastic scattering, the radiance is given by:

$$J(\lambda,\lambda_L,z,r)=\beta(\lambda,\lambda_L,z,r)\cdot I(z,r) \tag{2.3}$$

Where:

- $\beta(\lambda,\lambda_L,z,r)$ is the backscattering coefficient, that is the fraction of the incident energy that is backscattered for the unity of the solid angle and for the unity of atmospheric depth $\left[L^{-1}sr^{-1}\right]$;
- $I(z,r)$ is the laser irradiance in position r at distance z

The β coefficient can be expressed in terms of scattering properties, as in the following:

$$\beta(\lambda,\lambda_L,z,r)=\sum_i N_i(z,r)\left(\frac{d\sigma(\lambda_L)}{d\Omega}\right)_i L_i(\lambda) \tag{2.4}$$

Where:

- $N_i(z,r)$ is the density of the i^{th} scattering species;

- $\frac{d\sigma(\lambda_L)}{d\Omega}$ is the scattering differential cross-section at λ_L wavelength, defined as the scattered energy for unity of time and for unity of solid angle around the direction Ω.
- $L_i(\lambda)$ is the emission spectra of the i[th] specie and $(L(\lambda)d\lambda)$ is the fraction of the scattered radiation that belongs to the spectral range $(\lambda, \lambda + d\lambda)$

Therefore, the β coefficient changes depending on the considered scattering.

Replacing in (2.1) the expressions for $p(\lambda, z, r)$ and $J(\lambda, \lambda_L, z, r)$ we can write:

$$P(\lambda, \lambda_L, z) = \Delta z \cdot \frac{A_O}{z^2} \cdot \int_{\Delta\lambda} \xi(\lambda) \cdot d\lambda \cdot \int_{dA} \beta(\lambda, \lambda_L, z, r) \cdot I(r, z) \cdot T(z, r) \cdot \chi(z, r) \cdot dA(z, r) \qquad (2.5)$$

To simplify the (2.5) is useful to assume that:

- In case of scattering the observed radiation, has a narrow bandwidth, comparable to that one of the laser;
- The atmosphere is horizontally homogenous in the overlap region between the field of view of the telescope and the laser beam;
- The laser intensity is homogenous in the interesting area $I(z, r) = I(z)$ on an area $A(z)$;
- The overlap factor χ is 1 in the overlap region between the laser and the field of view of the telescope and 0 elsewhere.

Under these constrains, the optical power received can be written as:

$$P(\lambda, \lambda_{L,}, z) = \Delta z \cdot \frac{A_o}{z^2} \cdot \xi(\lambda) \cdot \beta(\lambda, \lambda_{L,}, z) \cdot T(\lambda, z) \cdot I(z) \cdot A(z) \qquad (2.6)$$

If we suppose that the laser pulse has a rectangular shape and duration τ_L, the irradiance can be written in the following form:

$$I(z) = \frac{E_L \cdot T(\lambda_L, z)}{\tau_L \cdot A(z)} \qquad (2.7)$$

Where:

- E_L is the energy of the laser pulse;
- $T(\lambda_L, z)$ is the transmissivity of the atmosphere at λ_L, at z altitude.

Introducing the optical power, $P_L = \frac{E_L}{\tau_L}$, under the hypothesis of single scattering the received power is:

$$P(\lambda, \lambda_L, z) = P_L \cdot \frac{c\tau_L}{2} \cdot \frac{A_0}{z^2} \cdot \xi(\lambda) \cdot \beta(\lambda, \lambda_L, z) \cdot T(\lambda, z) \cdot T(\lambda_L, z) \tag{2.8}$$

In this equation the chemical-physical properties of the permeable medium act trough the optical parameters: β and T.

It's useful to point here that the equation (2.8) gives an underestimation of the real backscattered signal because it doesn't take in account photons that the telescope collects after a multiple scattering and background photons at the same wavelength.

2.2.1 The optical parameters

In this paragraph a detailed analysis of the optical parameters that characterize the Lidar signal will be reported: the backscattering coefficient β and the extinction coefficient, taking into account the two scattering processes considered in this thesis: the elastic and inelastic scattering phenomena.

2.2.2 Optical parameters for the elastic scattering

In case of elastic scattering the Lidar equation (2.8) becomes:

$$P(\lambda, \lambda_L, z) = P_L \cdot \frac{c\tau_L}{2} \cdot \frac{A_0}{z^2} \cdot \xi(\lambda_L) \cdot \beta(\lambda_L, z) \cdot T^2(\lambda_L, z) \tag{2.9}$$

Therefore, in the elastic case the wavelength of the received optical power is the same of the laser pulse sent in the atmosphere.

The backscattering coefficient β is the sum of two contributions: the molecular one and the aerosol one. The first one is due to the backscatter from molecules described by Rayleigh theory, the second one is described by Mie theory. It results that: $\beta = \beta_a + \beta_m$

$$\beta_{mol} = N_{mol} \frac{d\sigma_R(\theta = \pi)}{d\Omega} \tag{2.10}$$

and:

$$\frac{d\sigma_R(\pi)}{d\Omega} = \frac{\pi^2(n^2-1)^2}{N_{mol}^2\lambda^4} \tag{2.11}$$

is the Rayleigh differential cross section for the angle of diffusion $\theta = \pi$, while N_{mol} is the number of molecules for the unit of volume. This last quantity, well-known from atmospherically models, represents the total molecular concentration in the atmosphere. A simplified expression of the backscattering differential cross-section, for the mixed gases under 100 Km, is the following one:

$$\frac{d\sigma(\pi)}{d\Omega} = 5.45\left(\frac{550}{\lambda(\mu m)}\right)^4 \cdot 10^{-28} cm^2 sr^{-1} \tag{2.12}$$

When the dimensions of the particle are comparable to the wavelength of the radiation the scattering problem becomes more complex. The aerosol backscattering coefficient can be expressed in term of the Fredholm integral:

$$\beta_{aer}(\lambda) = \int_0^\infty \sigma_B(a,\lambda,n) N'_{aer}(a) da \tag{2.13}$$

Where:

- σ_B is the Mie backscattering cross-section of a particle of radius a and refraction index *n*;
- N'_{aer} represents the number of particles with a radius between a and $a + da$ per unity of radius, linked to the total number of particle by the expression:

$$N_{aer} = \int_0^\infty N'_{aer}(a) da \tag{2.14}$$

The dependence of σ_B from a, λ and n, according to Mie theory, can be expressed by:

$$\sigma_B(a,\lambda,n) = \pi a^2 Q_B(x,n) \tag{2.15}$$

where Q_B is the backscattering efficiency, or the ratio between the backscattering cross section and the geometrical cross section; its dependence from the dimension of the scattering element and from the wavelength of the incident radiation is included in the x factor according to the relation:

$$x = \frac{2\pi a}{\lambda} \ .$$

The extinction coefficient α depends from two contributions, the molecular and the aerosol one, and it results:

$$\alpha = \alpha_{mol} + \alpha_{aer} = \alpha_{mol,a} + \alpha_{mol,s} + \alpha_{aer,a} + \alpha_{aer,s} \tag{2.16}$$

In this last formula the indexes a and s refer to the absorption and the scattering respectively. The term $\alpha_{mol,s}$ is connected to the Rayleigh cross-section σ_R by the relation:

$$\alpha_{mol,s} = N_{mol,}\sigma_R \tag{2.17}$$

The term $\alpha_{mol,a}$, describing the absorption by the gas molecules, is a function of λ and it is predominant in the correspondence of the absorption lines of the atmospheric components. In addiction, from the Rayleigh theory it is well-known the link between β_{mol} and α_{mol}, with $\alpha_{mol} = \alpha_{mol,a} + \alpha_{mol,s}$. Because $\alpha_{mol,a}$ is negligible in the visible, it stands:

$$\alpha_{mol} = \frac{\beta_{mol}}{0.119} \tag{2.18}$$

Considering the aerosol contribution and under the assumption that the aerosols can be considered as spherical particles or a homogeneous polidispersion of spheres, it stands that:

$$\alpha_{aer}(\lambda) = \int_0^\infty \sigma_E(a,\lambda,n) N'_{aer}(a) da \tag{2.19}$$

Where σ_E is the extinction cross section for particles of radius a and index of refraction n, considered as the sum of the contributions of the scattering and of the absorption, respectively as:

$$\sigma_{aer,s}(a,\lambda,n) = \pi a^2 Q_s(x,n) \tag{2.20}$$

$$\sigma_{aer,a}(a,\lambda,n) = \pi a^2 Q_a(x,n) \tag{2.21}$$

Where Q_s and Q_a represent respectively the efficiencies of scattering and absorption and can be determined with numerical methods

2.2.2 Optical parameters in inelastic scattering conditions

When the wavelength of the backscattering signal and the laser are different, this means that an inelastic scattering process occurred. Raman scattering is included in this category, and in this case the Lidar equation assumes the following expression:

$$P(\lambda_{R,}z) = P_L \frac{A_o}{z^2} \frac{d\sigma_{\lambda_R}(\pi)}{d\Omega} N_R(z)\xi(z)\frac{c\tau}{2} T(\lambda_R, z)T(\lambda_L, z) \tag{2.22}$$

Where:

- λ_L is the laser wavelength;
- λ_R is the returned wavelength, and $\lambda_L \neq \lambda_R$
- $N_R(z)$ is the numerical density of the molecule that participate to the scattering process. In case of nitrogen, it amounts at 78% of the total atmospheric density.
- $\frac{d\sigma_R(\pi)}{d\Omega}$ is the Raman cross section for the inelastic backscattering cross section at 180°.

The extinction coefficients $\alpha(\lambda_R)$ and $\alpha(\lambda_L)$, in the factors $T(\lambda_R, z)$ and $T(\lambda_{L,}z)$, are influenced by the physical characteristic of the atmosphere, and both depend by the sum of two contributions from aerosol and molecules.

From the (2.20) and the definition of the transmission it results that the total extinction of the collected signal is :

$$\alpha_{tot} = \alpha(\lambda_R) + \alpha(\lambda_L) = \alpha_{aer}(\lambda_R) + \alpha_{mol}(\lambda_R) + \alpha_{aer}(\lambda_L) + \alpha_{mol}(\lambda_L) \tag{2.23}$$

This equation put in evidence the fact that the extinction of the returned signal depend from the extinction coefficients at the two wavelength λ_L and λ_R, that attenuate differently the two beams, because the transmission properties of the atmosphere change with the wavelength. The dependence from the wavelength of the molecular coefficient is expressed by the corresponding cross-sections and can be considered known, while the wavelength dependence of the aerosol coefficients is much more complicated, depending also by the shape and the index of refraction of the particles,. An estimation of the extinction coefficient

at the wavelength of Raman scattering can be obtained from an empirical relation that links the ratio of the extinction coefficients with the inverse ratio of the respective wavelengths:

$$\frac{\alpha_{aer}(\lambda_R)}{\alpha_{aer}(\lambda_L)} = \left(\frac{\lambda_L}{\lambda_R}\right)^k \tag{2.24}$$

k is a variable factor depending from the dimension of the particles along the path of the propagation of the beam.

2.3 Inversion of the Lidar equation

Considering the single-scattering Lidar equation:

$$P(\lambda, \lambda_L, z) = P_L \frac{c\tau_L}{2} \frac{A_0}{z^2} \xi(\lambda) \beta(\lambda, \lambda_L, z) T(\lambda, z) T(\lambda_L, z) \tag{2.25}$$

This equation has two unknowns: the aerosol extinction α_{aer} and backscattering β_{aer} coefficients.

To the purpose of obtain these coefficients, that are strictly connected to the microphysical properties of the atmosphere, several algorithms to invert the Lidar equation have been found. In the following there are reported some algorithms utilized in these thesis for the retrieval of the aerosol's coefficients.

2.3.1 The Ansmann's method to retrieve the extinction coefficient

This method, proposed for the first time by Ansmann [2.1], allows the determination of the extinction coefficient $\alpha_{aer(\lambda_L)}$ when Raman measurements are available. Consider the Lidar equation (2.22), rewritten in compact form as:

$$P(z) = \frac{K}{z^2} N_R(z) T(\lambda_L, z) T(\lambda_R, z) \tag{2.26}$$

K includes the constant factors, independent from the altitude, corresponding to the efficiencies of the collection system (geometric factor), of the transmission optics and of the detectors.

In addiction, the overlap factor $\chi(z)$, in equation (2.5) that depends generally by the altitude was fixed to the unity value.

From (2.26) it is possible to obtain:

$$\frac{P(z)z^2}{N_R(z)} = KT(\lambda_L, z)T(\lambda_R, z) \tag{2.27}$$

Inserting the expression of the atmospheric transmissivity and taking the logarithms, it stands that:

$$\ln\left[\frac{P(z)z^2}{N_R}\right] = \ln K - \int_0^z \left[\alpha_{aer}(\lambda_L, z) + \alpha_{aer}(\lambda_R, z)\right] dr - \int_0^z \left[\alpha_{mol}(\lambda_L, z) + \alpha_{mol}(\lambda_R, z)\right] dr \tag{2.28}$$

and, by deriving both members with respect to z, it stands:

$$\frac{d}{dz}\ln\left[\frac{P(z)z^2}{N_R}\right] = -\left[\alpha_{aer}(\lambda_L, z) + \alpha_{aer}(\lambda_R, z)\right] - \left[\alpha_{mol}(\lambda_L, z) + \alpha_{mol}(\lambda_R, z)\right] \tag{2.29}$$

Let's consider the empirical relation (2.24), with k=1 for aerosol with dimension comparable with the laser wavelength, and k=0 for ice crystals [2.2].

Introducing this relation in (2.29) the following expression can be obtained for $\alpha_{aer}(\lambda_L)$:

$$\alpha_{aer}(\lambda_L) = \frac{\dfrac{d}{dz}\left[\ln\dfrac{N_R(z)}{P(z)z^2}\right] - \alpha_{mol}(\lambda_L, z) - \alpha_{mol}(\lambda_R, z)}{1 + \left(\dfrac{\lambda_L}{\lambda_R}\right)^k} \tag{2.30}$$

The advantage of this method is the possibility to have an expression for $\alpha_{aer}(\lambda_L)$ independent from the backscattering coefficient.

2.3.2 Klett and Fernald's method to determine the backscattering coefficient

Using this method [2.3], is possible to retrieve the aerosol backscattering coefficient β from the Lidar equation in elastic scattering conditions, supposing known a new parameter, the Lidar ratio (LR), that is the ratio between α and β for aerosols:

$$LR = \frac{\alpha_{aer}}{\beta_{aer}} \tag{2.31}$$

Let's introduce a new variable $S(z)$ defined as the logarithm of the Lidar signal multiplied for the square of the altitude (Range Corrected Signal, RCS):

$S(z) = \ln\left[P(z)z^2 \right]$ where the dependence from λ is omitted for brevity.

To express the Lidar equation in a form independent by the receiving system, we consider $S(z)$ at a reference altitude z_0; it stands that:

$$S(z) - S_0 = \ln\left[\frac{\beta}{\beta_0} \right] - 2\int_{z_0}^{z} \alpha(z)dz \tag{2.32}$$

Where $\beta_0 = \beta(z_0)$ and $S_0 = S(z_0)$.

Taking the derivative of the (2.32) with respect to z, it can be obtained that:

$$\frac{dS}{dz} = \frac{1}{\beta}\frac{d\beta}{dz} - 2\alpha(z) \tag{2.33}$$

This equation contains two unknowns and can be reduced to a linear one trough the knowledge of the Lidar ratio. In addiction, because $\beta = \beta_{aer} + \beta_{mol}$, α can be written as

$$\alpha = \alpha_{aer} + \alpha_{mol} = LR \cdot \beta_{aer} + B_R^{-1}\beta_{mol} \tag{2.34}$$

Where, according to Rayleigh theory, $B_R^{-1} = \frac{1}{0.119}$ and describes the constant ratio between α and β in Rayleigh scattering regime.

Substituting the (2.34) in (2.33), it stands that:

$$\frac{dS}{dz} = \frac{1}{\beta}\frac{d\beta}{dz} - 2(LR \cdot \beta_{aer} + B_R^{-1}\beta_{mol}) \tag{2.35}$$

And, because $\beta_{aer} = \beta - \beta_{mol}$, it can be obtained that:

$$\frac{dS}{dz} = \frac{1}{\beta}\frac{d\beta}{dz} - 2LR \cdot \beta + \frac{2}{B_R^{-1}}\int_{z}^{z_m} \beta_{mol}dz - 2\int_{z}^{z_m} LR \cdot \beta_{mol}dz \tag{2.36}$$

Where it was set $S_m = S(z_m)$, and deriving respect to z, it stands that:

$$\frac{dS'}{dz} = \frac{dS}{dz} + \frac{2}{B_R}\beta_{mol}\Big|_{z}^{z_m} - 2LR \cdot \beta_{mol}\Big|_{z}^{z_m} \tag{2.37}$$

From (2.37) and (2.34) the Bernoulli ordinary differential equation can be obtained: $\frac{dS'}{dz} = \frac{1}{\beta}\frac{d\beta}{dz} - 2\beta \cdot LR$

which has the following solution:

$$\beta(z) = \frac{e^{(S'-S'_m)}}{\beta_m^{-1} + 2\int_z^{z_m} LR \cdot e^{(S'-S'_m)} dr'} \tag{2.38}$$

Where $\beta_m = \beta(z_m)$.

If the backscattering coefficient at a reference altitude is known, also the total backscattering coefficient $\beta(z)$ can be obtained.

From the vertical profile of the molecular density $\beta_{mol}(z)$ and then β_{aer} are retrieved.

The possibility to retrieve β_{aer} using this method is linked to the knowledge of the Lidar Ratio, that is a complex function of the altitude z, depending from the wavelength and the chemical-physical properties of the particles (refraction index, distribution of dimensions, relative humidity, and so on).

A classification of possible values of Lidar ratio of aerosols was done by Ackermann [2.4], in function of the relative humidity, for different types of tropospheric aerosols and for signal at 355 nm.

2.3.3 Method of Wandinger for the backscattering coefficient retrieval

This method allows determining the backscattering aerosol coefficient by the simultaneous measurements of the elastic and Raman from N_2 molecules signals [2.5].

Let's consider the Lidar equations (2.9) and (2.22), for the elastic and Raman-shifted signals respectively:

$$P(\lambda_L, z) = P_L \frac{c\tau}{2} \frac{A_0}{z^2} \xi(\lambda_L) \chi(\lambda_L, z)(\beta_{\lambda_L}^{aer} + \beta_{\lambda_L}^{mol}) e^{-2\int_0^z \left[\alpha_{\lambda_L}^{aer}(r) + \alpha_{\lambda_L}^{mol}(r)\right] dr} \tag{2.39}$$

$$P(\lambda_L, \lambda_R, z) = P_L \frac{c\tau}{2} \frac{A_0}{z^2} \xi(\lambda_R) \chi(\lambda_R, z) N_R(z) \frac{d\sigma_{\lambda_R(\pi)}}{d\Omega} e^{-\int_0^z \left[\alpha_{\lambda_L}^{aer}(r) + \alpha_{\lambda_L}^{mol}(r)\right] dr} e^{-\int_0^z \left[\alpha_{\lambda_R}^{aer}(r) + \alpha_{\lambda_R}^{mol}(r)\right] dr} \tag{2.40}$$

Taking the ratio of the signals at two different altitudes:

$$\frac{P_{\lambda_L}(z)P_{\lambda_R}(z_0)}{P_{\lambda_L}(z_0)P_{\lambda_R}(z)} \tag{2.41}$$

where z_o is a reference altitude, and substituting the (2.39) and (2.40) in (2.41), we obtain:

$$\beta_{aer}^{\lambda_L}(z)=\left[\beta_{\lambda_L}^{aer}(z_0)+\beta_{\lambda_L}^{mol}(z_0)\right]\frac{N_R(z)P_{\lambda_L}(z)P_{\lambda_R}(z_0)e^{-\int_{z_0}^{z}\left[\alpha_{\lambda_R}^{aer}(r)+\alpha_{\lambda_R}^{mol}(r)\right]dr}}{N_R(z_0)P_{\lambda_L}(z_0)P_{\lambda_R}(z)e^{-\int_{z_0}^{z}\left[\alpha_{\lambda_L}^{aer}(r)+\alpha_{\lambda_L}^{mol}(r)\right]dr}}-\beta_{\lambda_L}^{mol}(z) \tag{2.42}$$

under the hypothesis that the overlap factors relative to the elastic and Raman channels are the same.

The reference altitude is chosen where $\beta_{mol}^{\lambda_L}(z_0) \gg \beta_{aer}^{\lambda_L}(z_0)$, in order to neglect $\beta_{aer}^{\lambda_L}(z_0)$;this corresponds to clean atmospheric condition, usually satisfied in high troposphere region. To determine β_{aer} from (2.42) the knowledge of the air's density, the atmospheric aerosol and molecular extinction properties and the molecular backscattering properties is needed.

The advantage of this method is that the knowledge of the LR is not necessary, but it is required only the a-priori knowledge of $\beta(z_0)$. The principal disadvantage is the low level of the Raman signal, because the backscattering Raman cross section is lower than the elastic one by about three order of magnitude ($\sigma_{el}=10^{-27}\frac{cm^2}{sr}, \sigma_R=10^{-30}\frac{cm^2}{sr}, \sigma_M=10^{-8}10^{-27}\frac{cm^2}{sr}$) [2.5]. This implies that the signal-to-noise ratio of the Raman signal is very low, and for this reason this method is not suitable for diurnal measurements.

2.4 Other optical parameters

Once the backscattering and the extinction coefficients are retrieved from the Lidar equation some other parameters can be obtained from the combination of them. These other parameters are very useful quantities to describe better the aerosols optical properties. In fact the size, the shape and the composition of aerosol particles influence their scattering characteristics and thus the radiative impact.

These parameters are: colour index, angstrom coefficient and depolarization coefficient.

Colour index: this parameter is defined as:

$$CI = \frac{\ln(\frac{\beta_{355}}{\beta_{532}})}{\ln(\frac{532}{355})} \tag{2.43}$$

It gives information about the dimensions of the particles[2.6].

Angstrom exponent: this parameter, defined as:

$$a^{0} = \frac{\ln(\tau_{355} / \tau_{532})}{\ln(532/355)} \tag{2.44}$$

τ is the optical depth, The Angstrom exponent is a parameter useful in discriminate the kind of aerosols [2.4].

Depolarization coefficient: this parameter, defined as:

$$\delta = \frac{\beta_{\perp}}{\beta_{\square}} \tag{2.45}$$

It is a product of the new Lidar system and it is used to distinguish a spherical aerosol from a non-spherical one (See Chapter 1).

Finally to retrieve the index of refraction, the size distribution and the concentration of the particles it is necessary to solve an inverse problem, concerning Fredholm integrals. Only the availability of a large quantity of experimental data at several wavelengths allows the determination of these quantities [2.7], [2.8].

2.5 Conclusion

In this chapter the working operation and the application of Lidar systems were briefly described.

The single scattering Lidar equation (2.25) was obtained in a monostatic configuration system. This equation relates the Lidar signal with the atmospheric parameters relative to the absorption and to the scattering of the laser beam. Therefore, to solve the Lidar equation in this case, a hypothesis on the relation between the coefficients above mentioned is required (Klett algorithm). We also have seen that if the Raman-shifted signal from nitrogen molecules can be detected, the Ansmann method allows determining the extinction coefficient directly. Finally, it was illustrated a third method of inversion, that permits to obtain an estimation of aerosol backscattering coefficient at the laser wavelength, independently by the Lidar ratio (Wandinger's method).

2.6 References

[2.1] A.Ansmann, U.Wandinger, M.Riebesell, C.Wietkamp, W.Michaelis, *Independent measurements of extinction and backscatter profile in cirrus clouds by using a combined Raman elastic-backscatter LIDAR*, Applied Optics, Vol.31, n.33 (1992)

[2.2] J.Klett, *Stable analytic inversion solution for processing Lidar returns,* Applied Optics, No.2, Vol.20 (1981)

[2.3] J.Klett, *Lidar inversion with variable backscattering/extinction ratio,* Applied Optics, 24, N°11 (1June 1985)

[2.4] J.Ackermann, *The extinction-to-backscatter ratio of tropospheric aerosol: a numerical study,* Journal of Atmospheric and Oceanic Technology, Vol.**15,** 1043-1050, (1998)

[2.5] A.Ansmann, U.Wandinger, *Combined Raman Elastic Backscatter LIDAR for vertical profile of moisture, aerosol extinction, backscatter and Lidar ratio,* Applied Physics, B**55,** 18-28 (1992).

[2.6] D.S.Balis et al., *Optical properties of Saharan dust layers as detected by a Raman lidar at Thessaloniky, Greece,* Geophysical research letters, 31, L13104, doi:10.1029/2004GL019881

[2.7] D.Muller et al., *Microphysical particle parameters from extinction and backscatter Lidar data by inversion with regularization: simulation,* Appl.Opt. 38, 2358-2368 (1999), doi:10.1364/AO.38.002358

[2.8] O.Dubovik et al., *Application of spheroid models to account for aerosol particle nonsphericity in remote sensing of desert dust,* J.Geophys.Res.111, doi.10.1029/2005 JD006619

Chapter 3

The Multiparametric Raman Lidar setup with the depolarization sensor

This chapter is dedicated to the description of the design, the development and the final realization of a Multiparametric Raman Lidar system with the depolarization sensor devoted to the measurement and the characterization of the atmospheric aerosols.

In Napoli a new Lidar system has been realized to improve the performances of the old one, with the final goal to obtain more information about the nature and vertical distribution of aerosols. In particular the design, the project, the realization and the calibration of the depolarization sensor was my doctorate topic and a particular relevance to this aspect will be give in the next chapter.

The Lidar system we realized works in a monostatic configuration for two wavelengths (355 nm and 532 nm), this means that the optical axes of the laser and of the telescope overlap, and the field of view (f.o.v.) of the telescope includes the divergence of the laser. The scattering volume, or the detected atmospheric volume, is defined as the intersection between the laser divergence and the field of view of the telescope.

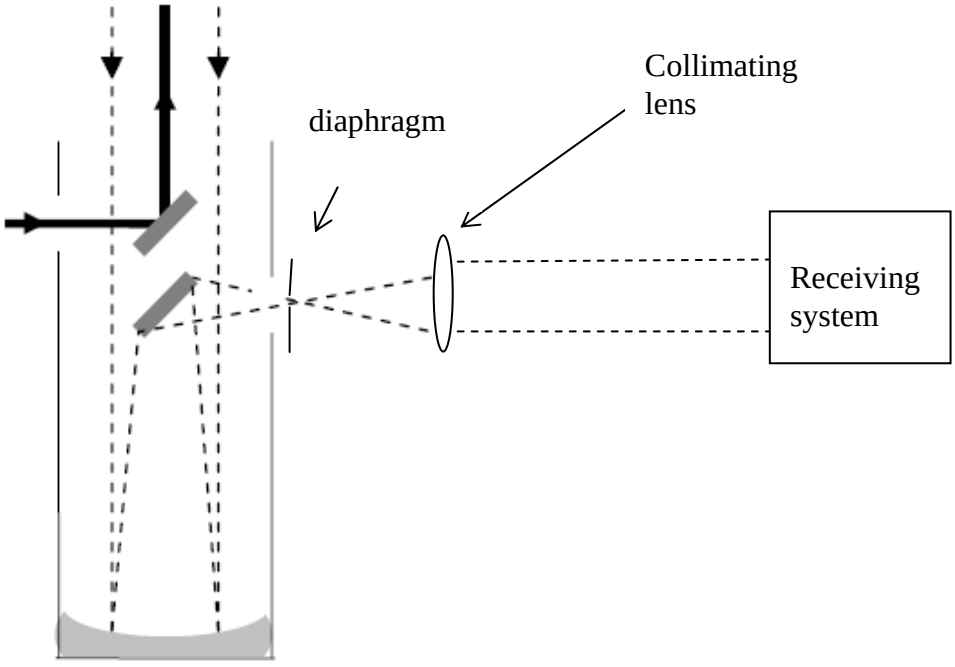

Fig3.1 Monostatic configuration of the Newtonian telescope-laser in Napoli Lidar system

The scheme of the Lidar experimental setup is showed in fig.3.2.

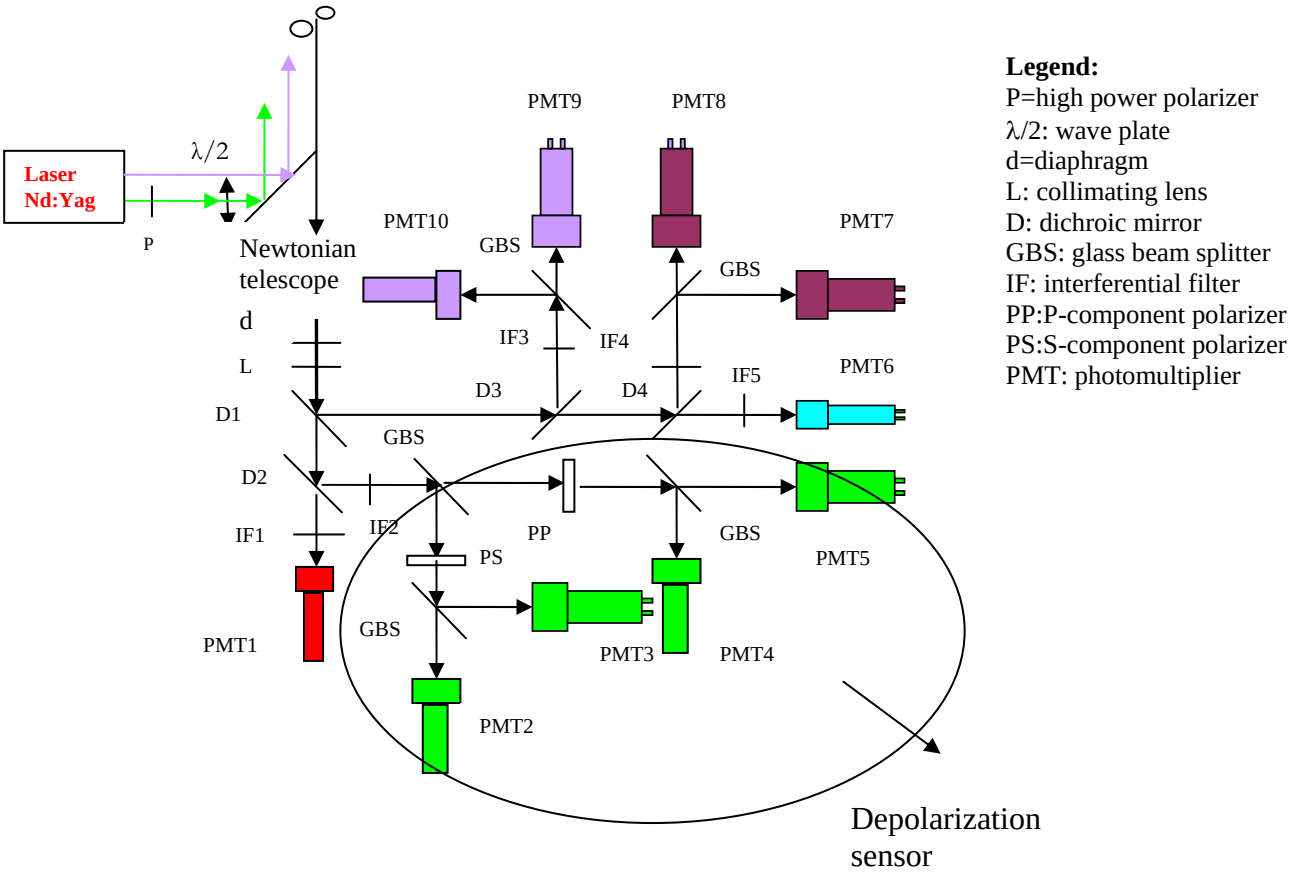

Fig.3.2 Scheme of Napoli Lidar system

The radiation backscattered from the atmosphere is collected by a telescope in Newtonian configuration and focused in a point where a diaphragm is posed. The light is directed to a convergent lens and then sent to a spectral selection system, constituted by dichroics, interferential filters, beam-splitters and polarizing sheets to discriminate the polarization direction of light for the green wavelength; then the radiation is sent to detectors that convert the optical signals into electrical ones, and finally the signals are acquired and analyzed to retrieve the optical properties of the atmospheric aerosols.

In the following paragraphs a detailed analysis of all the components of the Lidar system is presented, justifying the specific choice for each of them.

3.1 The transmission system

Sending mirrors: The laser radiation is sent into the atmosphere through multilayer dielectric mirror-systems that allows obtaining high value of reflectivity for a specific wavelength, and for a particular incident direction. In our case the involved wavelengths are in the green and in UV and the incident angle is 45°. These mirrors have high-power damage thresholds.

Beam expanders: It is a system of lens that expands the beams in order to reduce the divergence of the laser.

Laser source: The light source utilized is a Nd:Yag laser, producing radiation at 1064 nm. Because the Lidar technique is based on Raman, Rayleigh and Mie scattering, which cross-sections are proportional to λ^{-4} for the first two, and $\lambda^{-\delta}$ $(0 < \delta < 4)$ for Mie, in order to have a higher backscattering signal, it's useful to utilize some physical processes that generate higher harmonics (i.e. radiations with smaller wavelengths). This is done through non-linear optical processes: the Nd:Yag laser cavity is followed by a succession of appropriate crystals for the generation of higher harmonic frequencies. In this way the system can operate simultaneously with three different wavelengths: the fundamental (1064nm), the second harmonic (532 nm), the third harmonic (355nm), with a repetition rate of 20 Hz. The technical details of the laser are summarized in Table 3.2:

Laser Nd:Yag (Brillant-mod B)

Wavelength and Energy per pulse	$\lambda = 1064nm$ $E_{MAX} = 600mJ$
	$\lambda = 532nm$ $E_{MAX} = 100mJ$
	$\lambda = 355nm$ $E_{MAX} = 100mJ$
Maximum repetition rate	20 Hz
Divergence	$\square\ 0.5mrad$ for $\lambda = 355nm$
	$\square\ 0.6nm$ for $\lambda = 532nm$
Pulse width	5-7ns
Bandwidth	$0.11cm^{-1}$
Optical pumping	Xenon flash lamps
Polarization state	$> 70\%$ for $\lambda = 1064nm$
	not specified by manufacturer at $\lambda = 355nm$ and $\lambda = 532nm$

Table 3.1 Technical characteristics of the laser source

3.2 The receiving system

The receiving system is constituted by a telescope in Newtonian configuration (see fig. 3.5), which will be described in this paragraph.

The primary mirror of the telescope is a spherical mirror with diameter of 30 cm and a focal length of 120 cm, while the secondary mirror is a plane mirror that sends the radiation to the detection system. The telescope collects the radiation backscattered by the molecules and the aerosols present in the overlap region between the field of view of the telescope and the divergence of the laser, the *volume scattering*. It's important to focus here that the presence of the secondary mirror produces a shadow zone that affects the intensity of the signal at low altitudes. In these conditions the Lidar signal is underestimated and must be corrected by a factor known as the *overlap factor*. The extension of the *overlap* zone is related to the field of view (f.o.v.) of the telescope, that can be changed by changing the aperture of the field diaphragm put in the focal plane of the telescope according to the relation: $f.o.v. \square \frac{d}{F_T}$, where d and F_T are the diameter of the diaphragm and the focal length of the telescope,

respectively. The use of a large aperture diaphragm allows reducing the altitude corresponding to the full overlap of the laser beam and the telescope's f.o.v., but it is detrimental because it produces an increment of the background radiation reducing the signal to noise ratio and inducing also the possible saturations of PMTs. As a compromise we decided to use two different diameters' diaphragms for the alignment, that will be described later, and for the measurement.
In the table 3.2 the principal characteristics of the receiving system are reported:

Telescope

Type	Newtonian
Primary diameter (m)	0.3
Radius of curvature (m)	2.4
Focal length (m)	1.2
Field of view (mrad)	1.54 mrad for measurement
	0.2 mrad for alignment

Table 3.2 Principal characteristics of the receiving system

3.3 Spectral selection system

This part of the receiving system is devolved to the selection of the wavelengths of interest. These are the UV and green wavelengths (355 and 532 nm respectively) for the elastic scattering processes and the Raman-shifted ones (386.7nm and 607 nm for the nitrogen molecules and 407 for water vapour).
Collimating lens: a lens is used to collect all the radiation at the exit of the telescope and to collimate it. It is placed at a distance from the diaphragm equal to its focal length. With reference to fig.3.2, the radiation backscattered by the atmosphere is collected by the telescope and sent, through the collimating lens, to the first dichroic mirror D_1, that transmits the green and the Raman-shifted radiation at 607 nm, while reflects the UV and the Raman-shifted radiation at 407nm and 386 nm. The reflectivity and the trasmittance of all the dichroic mirrors have been measured with a spectrophotometer. In fig. 3.6 the reflectivity of D_1 is reported having as reference the reflectivity of a metallic mirror:

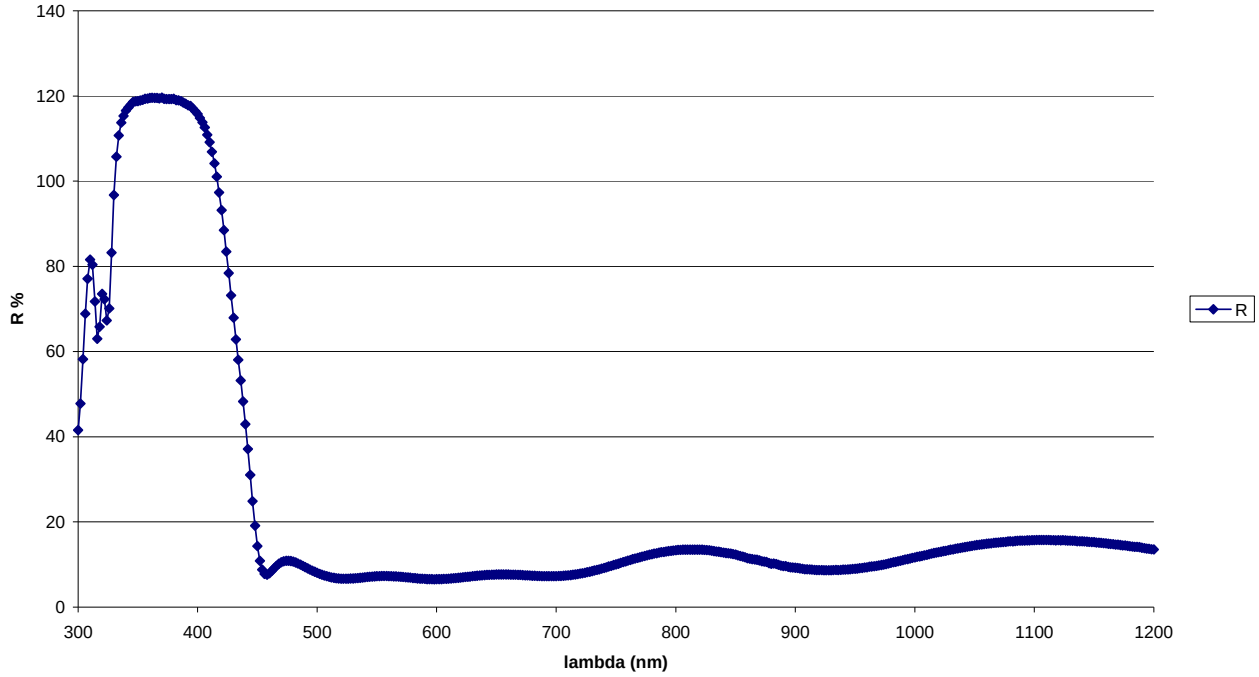

Fig.3.6 Reflectivity of the dichroic mirror D_1

The beam transmitted by D_1 is sent to another dichroic mirror D_2, that reflects the green wavelength and transmits the Raman-shifted at 607 nm. The spectral characteristics of the D_2 mirror are reported in table 3.4.

Size (mm)	25.2 x 35.6
Thickness (mm)	1.1
Reflection Band (nm)	530 - 585nm
Transmission Band (nm)	601 - 800nm
Cut-Off Wavelength (nm)	595nm
Minimum Transmission (%)	>90 in Transmission Band, >2 in Reflection Band

Table 3.4 Table with the spectral characteristics of the D_2 dichroic mirror

The transmitted radiation is filtered at 607nm and detected by PMT_1. The radiation reflected by D_2 is filtered by the interferential filter centred at 532 nm, with a bandwidth of 0.5 nm, and then separated by a glass beam-splitter in two components. Then two polarizes PS and PP select the two state of polarization of the green radiation. Nominally they have an extinction ratio of 1:10^4 for a wavelength range of 400nm-700nm, and a transmission of $25\% \pm 2\%$. One is devoted to filter the P-component of the light (the component transmitted by the glass beam-splitter), this means that this polarizer is aligned with its axis along the direction of the initial polarization of the light, and the other (that one reflected by the glass beam-splitter) selects the S-component of the light, this means that the polarizer is aligned in the orthogonal direction with respect to the initial direction of the laser beam polarization. The alignment of the channels was performed during the night, removing all the optical elements in the receiving system that could have some dependence on the polarization direction of the incident light. Then, the polarizer in the S-channel was rotated, until the minimum signal was detected with the analog detector. Concerning the polarizer in the P-channel, the same procedure was done, but when the minimum of the signal was found, the position of the polarizer was rotate by 90°. With this procedure both the angle between the two channels and the alignment of the two channels with respect to the direction of the laser were ensured. The following step was the insertion of a half wavelength wave plate in the laser beam path and its alignment with the laser polarization direction. This wave plate, was placed in the transmission system immediately after the high power-polarizer (see fig.3.2),; its alignment has been realized by rotating it until the minimum in the S-channel, was found once again.

Coming back to the reflection on the D_1 mirror (UV and Raman shifted UV radiation) we can see that $D_{3,}$ another dichroic mirror, reflects the UV elastic backscattering radiation, and transmits the Raman-shifted UV radiations at 386 and 407 nm.

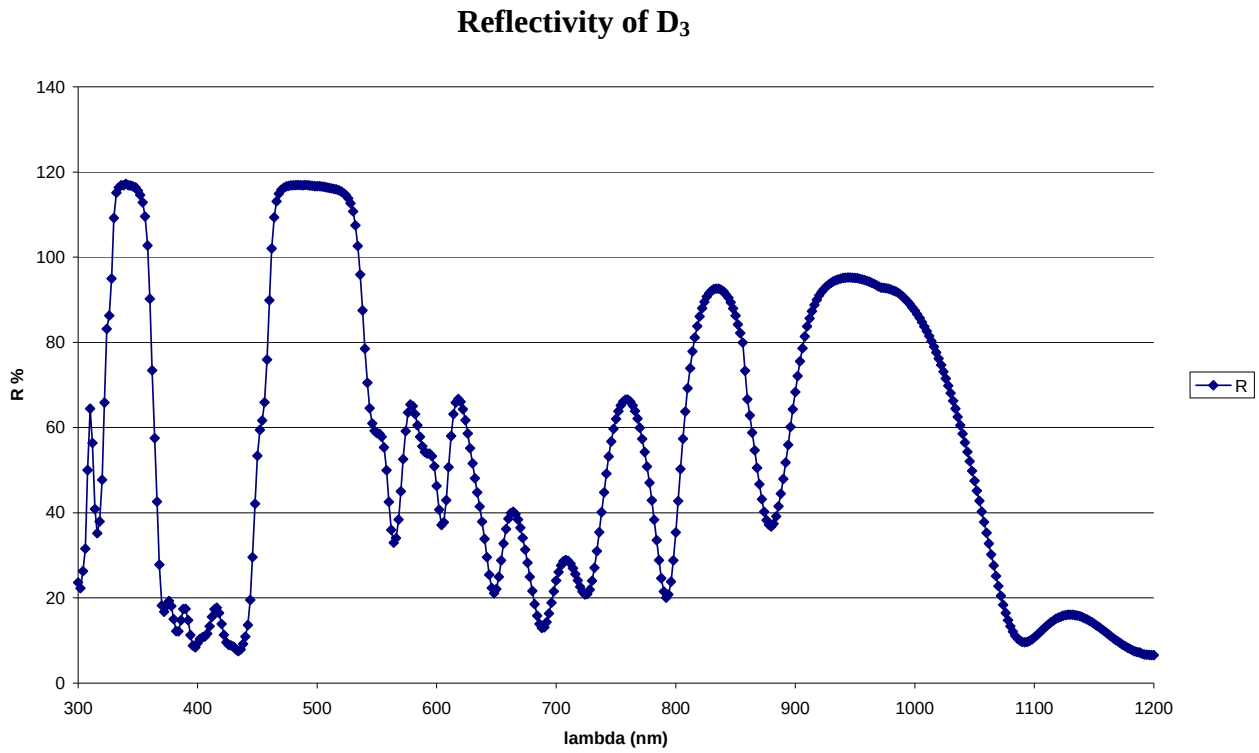

Fig.3.7 Reflectivity of D_3 in function of lambda

The reflection of the D_3 (the UV part of incident radiation) is filtered by an interferential filter IF_3 centered at 354.66 nm, with a bandwidth of 0.57 nm, and then detected by a system of two photomultipliers (PMT_9 and PMT_{10}). The UVelastic radiation detection is splitted in two ranges of detection, with two different PMTs. The detection is splitted, because the impossibility for only one PMT to follow with high efficiency all the dynamic of the signal and it is optimized in order that the one in analog mode detect the signals from low altitudes, while the other one that works in digital mode detects the signals from high altitudes. The Raman shifted UV radiation transmitted by D_3, is directed to D_4, that separates the Nitrogen Raman shifted radiation (at 386.7 nm) from the water vapour Raman shifted radiation (at 407nm). In particular the 386.7 nm radiation is reflected towards the PMT_5 detector, and the 407 nm radiation is transmitted to PMT_6 detection. The reflectivity of D_4 with respect to a metallic mirror is reported in fig.3.8:

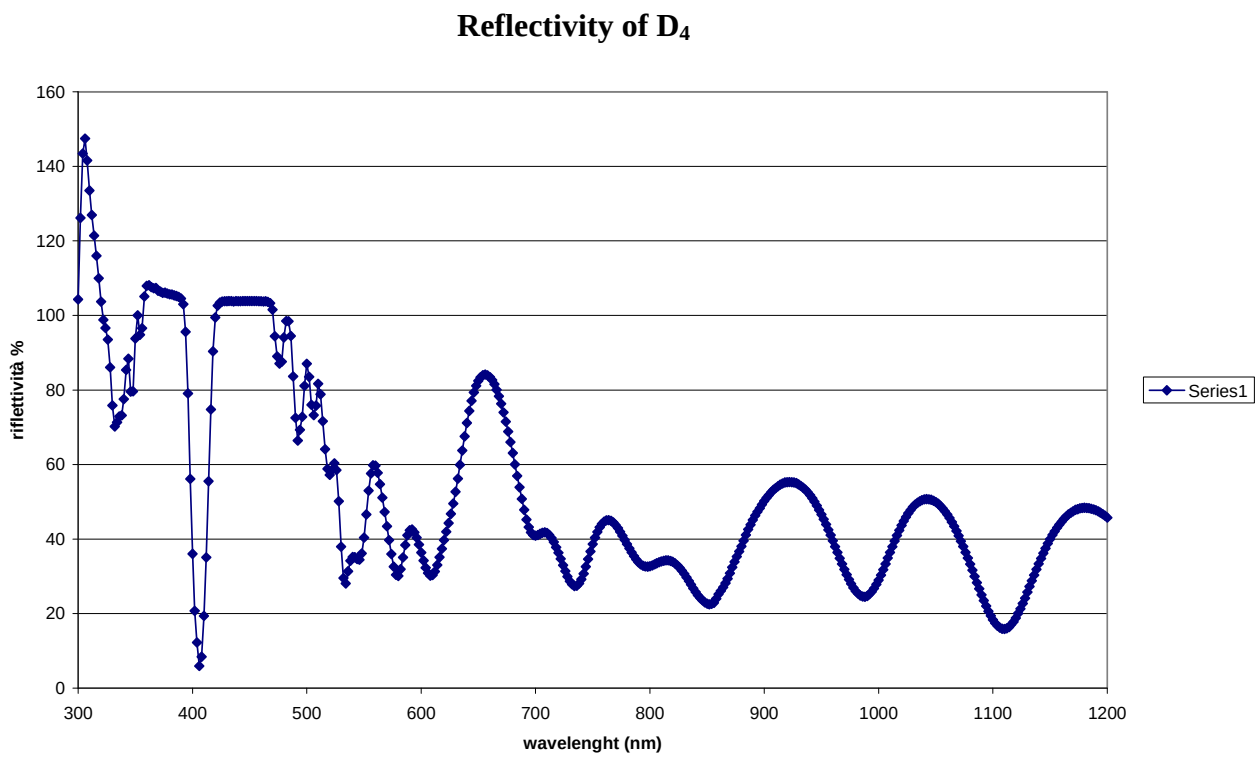

Fig.3.8: Reflectivity of D_4 respect to a metallic mirror

After the interferential filter $IF_{4,}$ centred at 386.7 nm and having a bandwidth of 0.48 nm, also the Raman shifted wavelength at 386.7nm is splitted in two regimes of detection: the first one for the low altitude and the second one for the high altitudes. The water vapour Raman shifted radiation is transmitted by $D_{4,}$ filtered by $IF_{5,}$ centred at 407.8 nm and having a bandwidth of 0.47 nm, and then detected by a cooled detector $PMT_{6.}$.This last detector is cooled because the signal from the water vapour is the most weak and therefore, it is necessary to reduce the background from the PMT.

3.4 Detection and acquisition system

The acquisition of the signals is performed by a system of fast photomultipliers; the radiation incident on each of them is attenuated by neutral filters, in order to avoid saturation phenomena. In particular the saturation phenomena were accurately studied for all the digital PMTs, and for all of them was found a correction in order to take into account the dead-time of the photomultiplier. The correction procedure is described here after.

The count rates for each digital PMTs were correlated with the signal, at the same wavelength, acquired at the same time by another detector working in analogic, linear mode. For count rates not too high, it is possible, to find the correction factor for those cases in which the behaviour of the PMT is “not paralyzable”[3.1].

In this case the correction formula is

$$N = \frac{n}{(1 - n \cdot \tau)} \tag{3.1}$$

N is the corrected count rate, n is the uncorrected count-rate and τ is the characteristic dead-time.

In fig.3.9 the uncorrected digital signal (blue curve), the dead-time corrected (the purple one) and the theoretical signal of PMT_{10}, are reported as a function of the analog one,

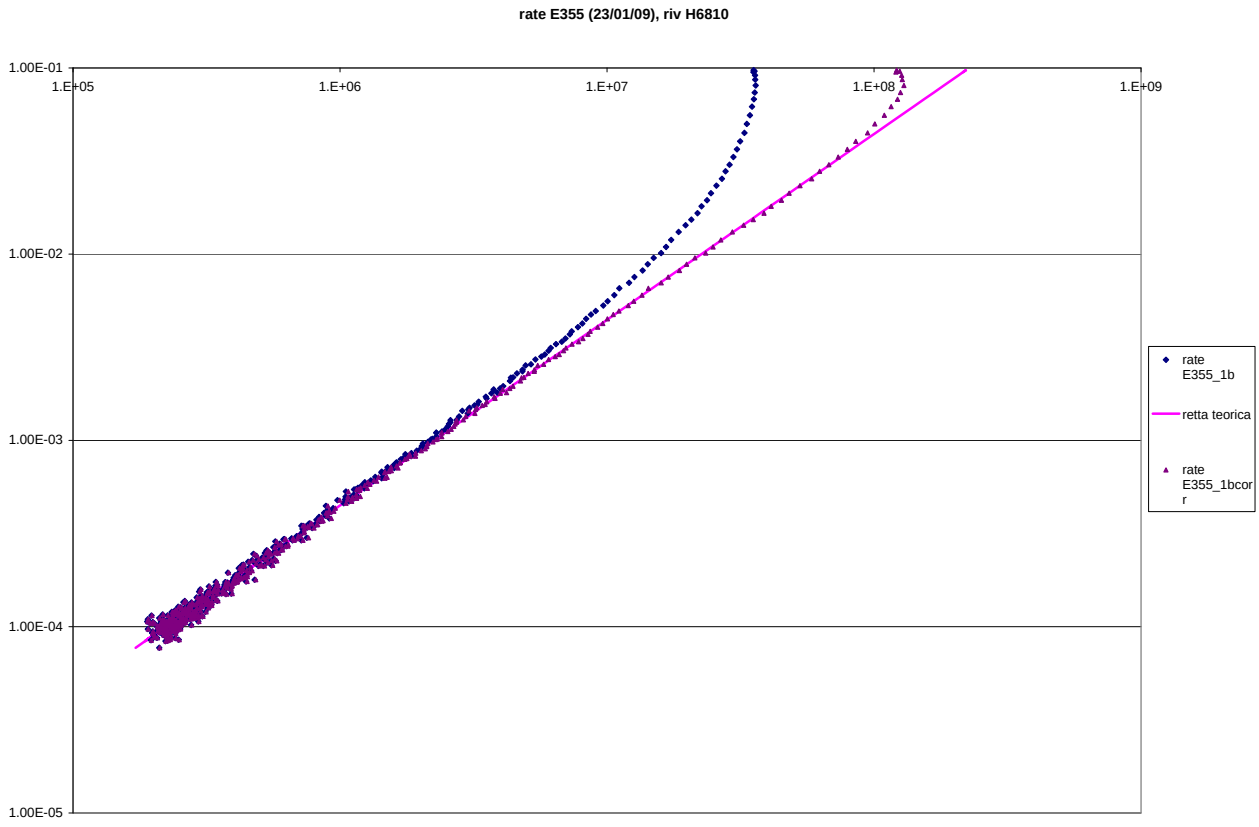

Fig.3.9: The digital signal of PMT_{10} not-corrected (blue curve) and corrected (purple curve) as a function of the analog one.

The dead-time was found to be 20 ns. The maximum rate of count reachable was found equal to 73 MHz

This procedure was repeated also for the other digital PMTs

Actually, the dead time correction cannot be applied to too high frequencies, and therefore the dynamic of a single detector is not wide enough to detect the signal coming from the whole sounded range. The splitting of the detection represents a solution to extend the dynamic range and to obtain a higher level of linearity.

In the following table it is reported the list of all the photomultipliers utilized in the detection system and the relative attenuations (the attenuation factor A is defined as A=-100logT, where T is the transmissivity of the filter) inserted before the input window:

UV elastic signal		
Low altitude PMT (PMT9)	Hamamatsu mod.R2079 select	Att:90
Low altitude acquisition	Analogical mode by digital Oscilloscope Tektronix (vertical resolution 10 bit, pass band 500 MHz)	
High altitude PMT10	Hamamatsu H-6180-01	Att.70
High altitude acquisition	Photon counting by EG&G Ortec MCS	
Green elastic signal (P-component)		
Low altitude PMT5	EMI mod.9202 QB	Att.0
Low altitude acquisition	Analogical mode by digital oscilloscope Tektronix (vertical resolution 10 bit, pass band 500 MHz)	
High altitude PMT4	Hamamatsu H-6180-01	Att.70
High altitude acquisition	Photon counting by EG&G Ortec MCS	
Green elastic signal (S-component)		
Low altitude PMT2	EMI mod.9202 QB	Att.0

Low altitude acquisition	Analogical mode by digital oscilloscope Tektronix (vertical resolution 10 bit, pass band 500 MHz)	
High altitude PMT3	Hamamatsu H-6180-01	Att.0
High altitude acquisition	Photon counting by EG&G Ortec MCS	
Raman signal N_2 (386)		
Low altitude PMT7	EMI mod.P25PC	Att.20
Low altitude acquisition	Photon counting by EG&G Ortec MCS	
High altitude PMT8	Hamamatsu H-6180-01	Att.0
High altitude acquisition	Photon counting by EG&G Ortec MCS	
Raman signal H_2O (407 nm)		
PMT5	Hamamatsu R1828-02	Att.0
Acquisition	Photon counting by EG&G Ortec MCS with Discriminator Philips threshold of 5 mV	
Raman signal N_2 (607 nm)		
PMT1	Metal package Photomultiplier tube R7400U Series	Att.0
Acquisition	Photon counting by EG&G Ortec MCS with Discriminator Philips threshold of 2 mV	

Table 3.5 Acquisition modalities and electron specifics about the ten different channels

The photon counting channels are acquired through MCS multiscaler boards up to an altitude of 30 Km, with a spatial resolution of 15 m, while the analogic channels are acquired through the oscilloscope until a distance of 7 Km, with a spatial resolution of 3m. Actually, the analog signals result utilizable between 300 m and 7 Km, while that one collected in photon counting regime extends from 1-2 Km up to 30 Km from the Lidar station. Therefore it is possible to find a range where the elastic signals acquired in the two different regimes overlap. It is in this range that we choose an altitude we use to merge the two signals, by taking the analog signal under and the photon counting signal above this altitude.

In this way, trough the simultaneous acquisition of the analog and digital signals, a wider dynamics is obtained, as is put in evidence in fig.3.16:

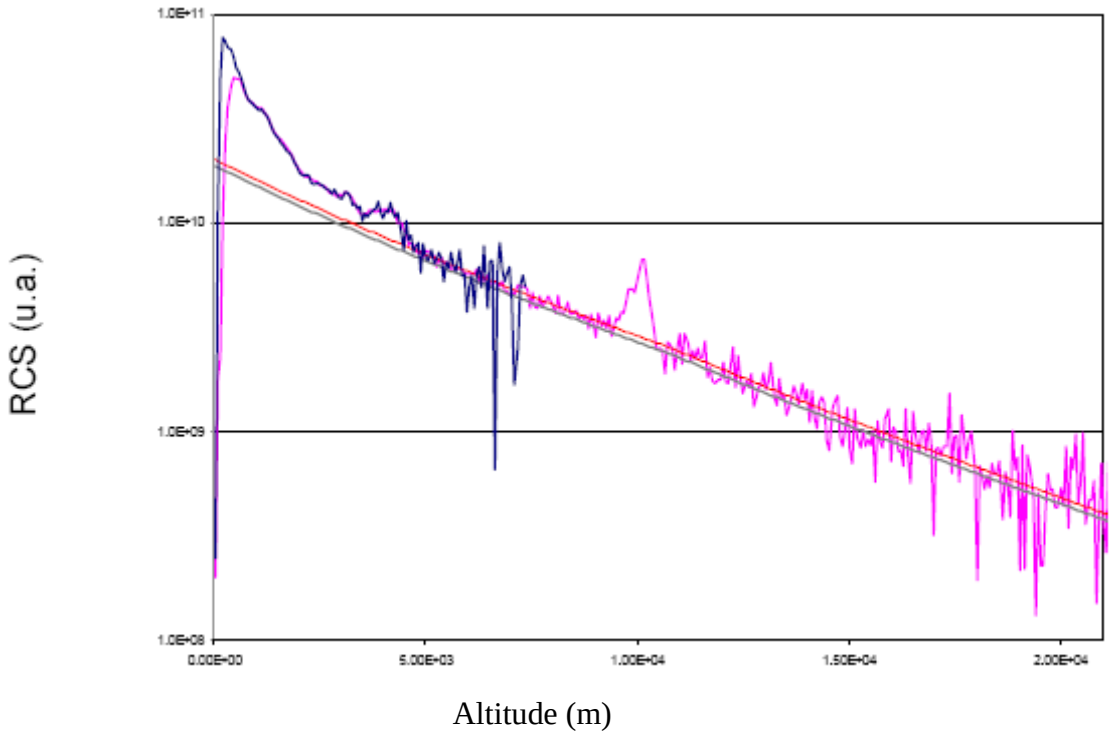

Fig.3.16 Dynamics extension of the signal trough the simultaneous acquisition in photon counting and in analog mode. The blue curve represents the RCS analog signal (optimized for the low altitudes) and the pink one is the digital one (optimized for the high altitude).

Raman signals

Because of their weak cross-section with respect to the elastic ones, the Raman signals are acquired only in night-time. The optical signal corresponding to the Raman scattering from

the nitrogen molecules at 387 nm is splitted, trough a glass beam splitted, in two different channels for high and low altitude detection. The signals corresponding to the nitrogen Raman scattering are acquired up to 30 Km of altitude, with a spatial resolution of 15 m (MCS broad).

Concerning the Raman wavelength at 407 nm, and at 607 nm, these are acquired in photon counting, but with only one detector, because usually these signals are weak, especially the signal at 407m. Although the acquired system allows reaching 30 Km of altitude, these signals rarely exceed the altitude of 7 Km for 407 nm and 15 Km for 607nm.

Multiscaler boards: The acquisition boards, the Multichannel scaler MCS, are devices that count the number of pulses received in a brief interval of time, known as dwell-time, in function of the delay from a trigger-signal; in our case this is a signal synchronous with the laser pulse generation. In our case the dwell-time is equal to 100 ns (corresponding to a spatial resolution of 15m) and we acquire signals for $200\mu s$, corresponding at a spatial range of 30 Km.

In the data analysis the spatial resolution is reduced to 60m.

3.5 Additional instrumentation: meteorological parameters' sensors

The lidar signal is strictly linked to the physical parameters of the atmosphere that influences its intensity trough the backscattering coefficient β and the extinction coefficient α. These last ones, as already described in the first chapter, depend from different parameters, like the molecular density, that can be put in relation with the atmospheric temperature and pressure, trough the equation of the perfect gases. It was showed that the temperature and pressure depend from the altitude in a complex way. This leads to the necessity to use atmospheric models that are widely described in literature. Anyway all these models require the knowledge of the temperature and pressure at ground, in our case at 118m above sea level.

Besides, also the wind speed and direction and relative humidity are systematically measured with a sample rate of 1 data point every minute.

All these meteorological informations are acquired trough a sounding system, installed on the roof of the laboratory. In fig. 3.17 is reported the scheme of the sonde and their

acquisition system: this last one supplies electrical signals that are digitally acquired by a module, Field-Point FP-A1-110 of the National Instrument, with 8 input channels, and a resolution of 16 bit. This module is characterized by an ADC (Analogical-Digital Converter), having as input the 5 parallel channels of the sonde and an interface RS232 that connect the serial exit to the ADC of the computer.

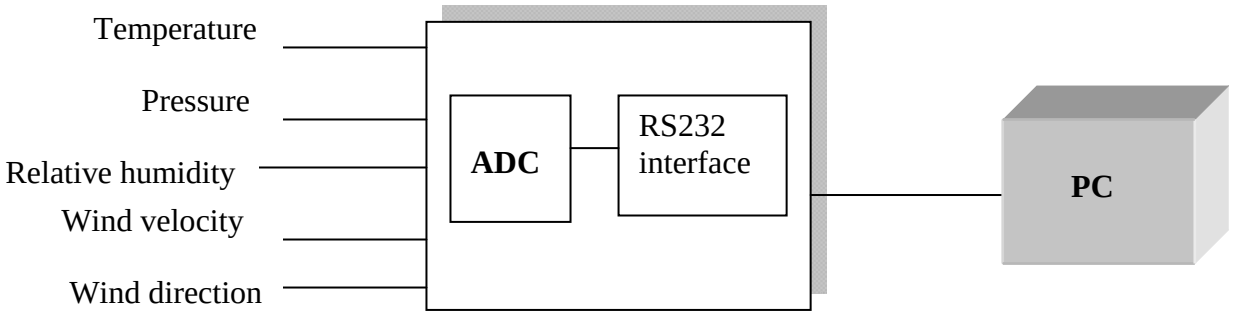

Fig.3.17 Scheme of the system constituted by the module FP-AI-110, that connects the sonde to PC

3.6 Description of a Lidar measurement

A measurement with the Lidar system can be splitted in a preliminary phase, consisting in the alignment of the system, and in a following step that is the real measurement.

The alignment of the system consists in searching the conditions that optimize the overlap between the laser beam and the f.o.v. of the telescope. The following step is the measurement.

A Lidar measurement consists of an average of 1200 measurements in one minute and then a sum over 30 minutes is performed. It's important to focus here that it's necessary to discard each measure in which the signal is affected by significant variations in the atmospheric conditions due to the presence of clouds. After the visualization of the different signals on the PC, we proceed to the subtractions of the background defined as the signal detected with a very high delay with respect to the laser pulse.

After that the analog and photon counting signals are merged together and a single signal, with a wider dynamic is obtained. This signal is then corrected for the overlap factor.

It is important to consider the fact that in the analysis of the lidar signals there are several error sources. In particular, the final backscattering profile is affected by an error that is determined by three principal factors:

1. the statistical error on the detected signals
2. the variability of the atmosphere
3. the uncertainty on the values of all the parameters that are used in the calculus of the backscattering profile.

The data analysis is based on two kinds of algorithm, Raman and Klett, applied to nocturnal and diurnal signals respectively. In both methods the vertical profile of the molecular density is needed. This profile is obtained trough the assumption of a theoretical atmosphere model, called “standard” [3.2].

Concerning the error of the signal, it was taken into account that the signal is an average of a series of signals. Therefore, the error was taken as the standard deviation of the average. This operation takes into account the temporal variability of the atmosphere. Actually, in general, the error on the signal results predominant with respect to that one on the density profile.

3.7 Conclusions

In Napoli a Multiparametric Raman Lidar system with a depolarization sensor was realized. A complete characterization of all the elements of the apparatus was done. This sensor is now operative for nocturnal and diurnal measurements in order to retrieve the optical properties of the atmospheric aerosols and clouds.

3.8 References

[3.1] W.R.Leo, *Techniques for Nuclear and Particle Physics Experiments,* Springer-Verlag

[3.2] International Civil Aviation Organization, *Manual of the ICAO Standard Atmosphere,* DOC 7488-CD, Third Edition, 1993, ISBN 92-9194-004-6

Chapter 4

Depolarization calibration procedures

This chapter is devoted to the problem of the depolarization's detection.
The alignment procedure of the P and S channels will be discussed and three calibration methods will be evaluated trough a sensitivity analysis performed by a numerical simulation, in order to obtain a reliable gain ratio of the system, and, finally, high level quality of Lidar depolarization measurements. In addiction a fourth calibration technique, that makes use of the total signal (P+S), will be presented.

4.1 The depolarization problem

It was showed in chapter 1, that the interaction with an ideal homogeneous sphere doesn't change the polarization state of the incident radiation. The Mie theory offers a rigorous description of the scattered phenomenon only for this simple case. In real life the particles of the atmosphere have some degree of membership to the "sphere-family" and some others to the "not-sphere family". Anyway when a linearly polarized laser source is scattered by a not spherical particle a depolarization appears.
The depolarization lidar technique makes use of this phenomenon by using a linearly polarized laser transmitter and a two-channel receiver capable of measuring the components of the return signal polarized parallel and perpendicular with respect to the transmitted beam. The signal splitting is typically accomplished using a polarizing beam splitter (PBS) that directs the perpendicular-polarized component of the backscatter signal to one channel and the parallel component to the other [4.1]. The calibrated ratio of these two components is known as the total depolarization ratio. Depolarization ratio measurements provide information about the shape and/or thermodynamic phase, (i.e. dry, liquid and ice phase of aerosols and clouds) of the particles in the scattering medium [4.2], and for this reason they have are of great interest in the atmospheric sciences. The depolarization technique dates back to the early 1970s, when the depolarization of backscattered laser light was show to provide effective discrimination between ice clouds and water clouds [4.3]. Recent analyses of cirrus clouds have used lidar-measured depolarization ratios to derive the effective shape

ratios of cirrus cloud particles [4.4]. Within the troposphere, polarization-sensitive Lidars are used to detect the presence of dust within the planetary boundary layer [4.5]. Depolarization ratios have also been used to identify and discriminate between volcanic ash and sulphuric acid droplets in the stratospheric aerosol plume produced by the eruption of Mount Pinatubo in 1991 [4.6]. Today, on a global scale, there is a relevant attention for depolarization measurements from the ground to be compared to the ones from the space, with the Calipso mission satellite, launched by NASA in 2006 [4.7] in order to deepen the knowledge of the multiple scattering effect and to correlate depolarization and extinction measurements.

In spite of the great interest in depolarization measurements, the effective realization of careful and calibrated depolarization measurements presents a lot of difficulties. Therefore accurate depolarization measurements constitute a relevant improvement of the existing Lidar systems. The realization methodologies, and first of all the possible calibration techniques, are object of discussion and the evaluation of them are the subject of several recent studies

4.2 The Lidar equation for the depolarization case

To study the depolarization from atmospheric aerosols and molecules a specific setup must be realized. In particular the Lidar receiving system should be able to select the parallel and the orthogonal components with respect to the initial direction of polarization of the laser source. The channel aligned with the initial direction of polarization of laser light is called “P-channel”, while the orthogonal one is called “S-channel”. The alignment procedure was described in the previous chapter.

The Lidar signals in the two channels have the following expressions:

$$P(z) = \frac{k_{//}}{z^2}\left[P_{//0}(\beta^a_{//}(z) + \beta^m_{//}(z)) + P_{\perp 0}(\beta^a_{\perp}(z) + \beta^m_{\perp}(z)) \right] e^{-2\tau} \tag{4.1}$$

$$S(z) = \frac{k_{\perp}}{z^2}[P_{//0}(\beta^a_{\perp}(z) + \beta^m_{\perp}(z)) + P_{\perp 0}(\beta^a_{//}(z) + \beta^m_{//}(z))] e^{-2\tau} \tag{4.2}$$

Where P and S refer to the power collected by the P and S channels respectively.

In the previous equations $k_{//}$ and $k_{\perp}$ are the efficiencies of the P and S channels respectively, $P_{//0}$ and $P_{\perp 0}$ are the initial powers of the laser source, and $P_{//0} / P_{\perp 0}$ is the degree of polarization of the laser source. It stands that $P_{//0} >> P_{\perp 0}$, therefore $P_{\perp 0}$ represents the initial depolarization of the laser source. The other symbols are already explained in chapter 2. Concerning the attenuation term, τ, written without subscripts, it is a reasonable hypothesis to neglect the effect of the polarization on it.

The depolarization ratio is defined as the ratio of the backscattering coefficient for perpendicular polarization to the parallel backscattering one, and can be obtained from the combination of (4.1) and (4.2):

$$\delta(z) = \frac{\beta_{\perp}^{a}(z) + \beta_{\perp}^{m}(z)}{\beta_{//}^{a}(z) + \beta_{//}^{m}(z)} = \left(\frac{S(z)}{P(z)} H - k \right) \cdot \left(1 - \frac{S(z)}{P(z)} H \cdot k \right)^{-1} \tag{4.3}$$

Where $H = k_{//} / k_{\perp}$ represents the calibration constant of the apparatus. In normal conditions a single term k can be used to take into account both the not perfect linearly polarized laser source and not perfectly aligned receiving system [4.8]. K is called from now on the instrumental depolarization.

The equation (4.3) was written in the general case. If we suppose a perfect linearly polarized laser source, and a perfectly aligned receiving system, the equation (4.3) assumes the simplified expression:

$$\delta(z) = \frac{S(z)}{P(z)} H \tag{4.4}$$

4.3 The calibration techniques

The calibration constant H is a necessary input to obtain the depolarization coefficient, and the accuracy of the calibration method is reflected in the quality of the depolarization measurements.

The theoretical part of my work consisted in the evaluation of different calibration techniques, one of them of recent introduction [4.9], in a quality comparison of the methods, in order to find the best and the most suitable one for our measurements conditions and our

apparatus. This work was carried out in co-operation with Dr. Yiming Zhao and Dr. Xiaomei Lu, from School of Electronic information Engineering, Beihang University, Beijing, China. They spent one year of their PhD in our laboratory, working on this subject.
We refer to the calibration techniques as:

1) Molecular or Rayleigh technique
2) 90° Technique
3) $\pm 45^{\circ}$ Technique
4) Three signals technique

In the following a general description and a detailed analysis of each of them will be done.

4.3.1 Molecular or Rayleigh technique

This calibration technique consists in the evaluation of the Lidar signals (parallel and orthogonal ones) in an atmospheric range free from aerosols. In fact, the depolarization of an aerosol free atmospheric layer is only due to molecular scattering and it can be exactly evaluated from the theory, here we will indicate as δ_{mol} the molecular depolarization.
If the Lidar signals are only due to molecular contribution they can be written as:

$$P_m(z) = k_{//}\left[P_{0//}\beta^m_{//}(z) + P_{o\perp}\beta^m_{\perp}(z)\right]e^{-2\tau} \tag{4.5}$$

$$S_m(z) = k_{\perp}\left[P_{0//}\beta^m_{\perp}(z) + P_{0\perp}\beta^m_{//}(z)\right]e^{-2\tau} \tag{4.6}$$

In a free-aerosol area the vertical profile of the depolarization coefficient is known, therefore, using eq.(4.3), (4.5) and (4.6) we can obtain the calibration constant from the following expression:

$$H = \frac{\sum_{i=1}^{n} P_m(z_i)}{\sum_{i=1}^{n} S_m(z_i)}\left(\frac{\delta_{mol} + k}{1 + k\cdot\delta_{mol}}\right) \tag{4.7}$$

Where $P_m(z)$ and $S_m(z)$ are the Lidar parallel and orthogonal signals in a free-aerosol range, and they are summed in the reference range to reduce the statistical variations, while δ_{mol} is the molecular depolarization, which value depends by the system characteristics and

by the temperature [4.10]. For our system the value of the molecular depolarization can be considered temperature independent, and its value is 0.00376 [4.10].

Anyway, performing only this calibration, the system depolarization remains unknown. Moreover this method requires the a-priori knowledge of the instrumental depolarization k.

Anyway, the advantage of this method is in the simultaneity of the calibration with respect to the measurement. The disadvantages are due to the fact that very often the aerosols are present also at medium altitude, therefore an aerosol free zone can only be found at very high altitude where the lidar signals are weak and the signal-to-noise ratio is very poor. This happens in a urban contest as in Napoli, where the atmospheric pollutants are in large amounts or when aerosols are carried by synoptic transport phenomena, like the transport of the Saharan dust from Africa that usually appears over Napoli also at medium altitudes (5-7km).

In fig.4.1 are showed the P-component RCS signal and the RCS molecular signal (RCS is the Range Corrected Signal, already mentioned in Chapter 2), normalized in a bad-supposed "clean atmospheric range", between 3 and 5 Km. The effective "clean atmospheric range" is after 8 Km. In fig.4.2 it is showed the consequence of this mistake, compared with a good calibration choice, that is reflected into a systematic error in the calibration constant.

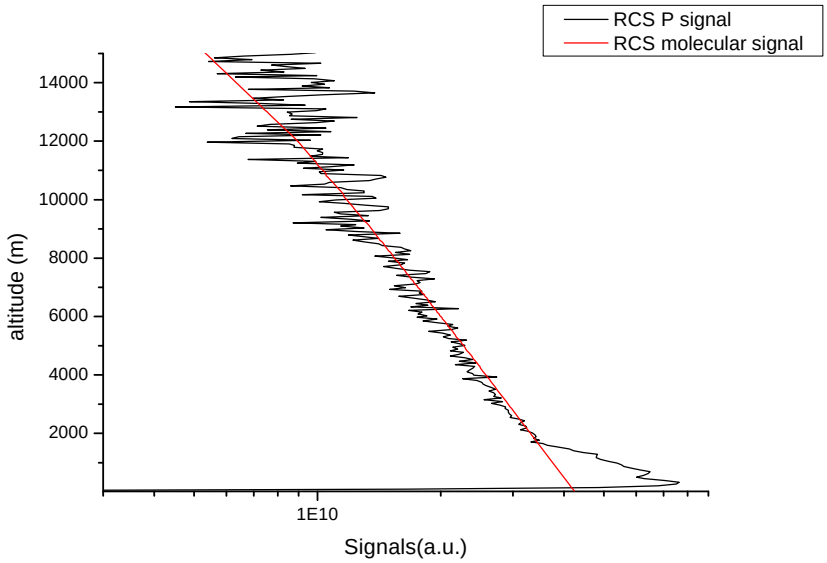

Fig. 4.1 P-component RCS (Range Corrected Signal) (black curve) and RCS Molecular Lidar signal (red line). The range where the normalization between the molecular and the P signal was done was taken between 3 and 5 Km. The real molecular signal is after 8 Km.

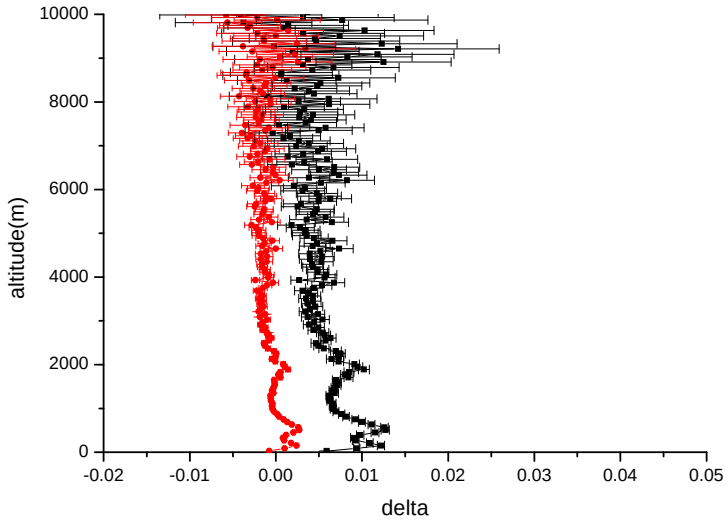

Fig.4.2 Depolarization ratio obtained with the calibration constant from the molecular method with a bad determination of the free aerosol range (red one) and the one obtained choosing the right range for the molecular calibration (black one) for an example of measurement of 17 September 2009

4.3.2. The 90° rotation technique

This calibration technique consists in the rotation of the laser source polarization by 90° and detecting the signals in the P and S channels in both angular positions. The signals, after the rotation, can be written in the following way:

$$P_2(z)=\frac{k_{//}}{z^2}\left[P_{0//}(\beta_{\perp}^{a}(z)+\beta_{\perp}^{m}(z))+P_{\perp 0}(\beta_{//}^{a}(z)+\beta_{//}^{m}(z))\right]e^{-2\tau(z)} \tag{4.8}$$

$$S_2(z)=\frac{k_{\perp}}{z^2}\left[P_{0//}(\beta_{//}^{a}(z)+\beta_{//}^{m}(z))+P_{0\perp}(\beta_{\perp}^{a}(z)+\beta_{\perp}^{m}(z)\right]e^{-2\tau(z)} \tag{4.9}$$

For this method the calibration constant has the following expression:

$$H=\sqrt{\frac{P_2(z)\cdot P_1(z)}{S_2(z)\cdot S_1(z)}} \tag{4.10}$$

Where P_1 and S_1 refer to the signals measured when the P-channel is aligned with respect to the initial direction of polarization of Lidar signals and S orthogonal with respect to it (regular measurements conditions, see equations 4.5 and 4.6)

The advantage of this method is the independence of the calibration constant by the altitude of the signals.

However, this formula is obtained under the hypothesis of a stable atmosphere between the two set of measurements. If the atmosphere changes sensitively systematic errors appear, as we will see later in the discussion of the theoretical simulations.

In the real case, especially in Napoli's contest, the atmospheric situation is very variable, so this technique was avoided.

4.3.3 The ± 45° rotation technique

The ± 45° rotation technique is a calibration method recently proposed by Freudenthaler et al. [4.9].

It consists in the rotation of the laser's direction of polarization of 45° in one direction and 45° in the opposite direction, and in the recording of the signals in P and S channels in both positions.

This method is based on the fact that the same amount of energy is sent to P and S two times, in the opposite directions.

The equations of the signals are the following ones:

$$P_2(z) = \frac{k_{//}}{z^2}\left[P_{//2}(\beta^a_{//}(z) + \beta^m_{//}(z)) + P_{\perp 2}(\beta^a_{\perp}(z) + \beta^m_{\perp}(z)) \right] e^{-2\tau(z)} \tag{4.11}$$

$$S_2(z) = \frac{k_{\perp}}{z^2}\left[P_{\perp 2}(\beta^a_{//}(z) + \beta^m_{//}(z)) + P_{//2}(\beta^a_{\perp}(z) + \beta^m_{\perp}(z)) \right] e^{-2\tau(z)} \tag{4.12}$$

when the laser is turned of +45°, and the following ones:

$$P_3(z) = \frac{k_{//}}{z^2}\left[P_{//3}(\beta^a_{//}(z) + \beta^m_{//}(z)) + P_{\perp 3}(\beta^a_{\perp}(z) + \beta^m_{\perp}(z)) \right] e^{-2\tau(z)} \tag{4.13}$$

$$S_3(z) = \frac{k_{\perp}}{z^2}\left[P_{\perp 3}(\beta^a_{//}(z) + \beta^m_{//}(z)) + P_{//3}(\beta^a_{\perp}(z) + \beta^m_{\perp}(z)) \right] e^{-2\tau(z)} \tag{4.14}$$

when the laser light is turned of -45°.

Where:

$$\begin{cases} P_{//2} = P_{//0} sin^2 \vartheta' + P_{\perp 0} \cos^2 \vartheta' \\ P_{\perp 2} = P_{//0} \cos^2 \vartheta' + P_{\perp 0} \cos^2 \vartheta' \\ P_{//3} = P_{//0} \cos^2 \vartheta'' + P_{\perp 0} \sin^2 \vartheta'' \\ P_{\perp 3} = P_{\perp 0} \cos^2 \vartheta'' + P_{//0} \sin^2 \vartheta'' \end{cases}$$

and ϑ'=+45° and ϑ''=-45°.

In the previous equations subscripts 2 and 3 refer to the two steps of the calibration procedure.

With this calibration technique the calibration constant has the following expression:

$$H = 0.5\left[\frac{P_2(z)}{S_2(z)} + \frac{P_3(z)}{S_3(z)}\right] \tag{4.15}$$

That represents the arithmetic mean of the ratio between S and P signals for the first and the second step of the calibration.

The advantages of this method are the possibility to use the signals for the calibration at every altitude, and the low sensitivity to the atmospheric changes.

4.3.4 The three signals technique

An additional calibration technique will be present in this paragraph. It makes use of the simultaneous detection of the total, the P and the S channels. In literature it was first proposed in 2003 [4.11]. As proposed this technique implies the knowledge a-priori of the optical characteristics of the receiving apparatus, concerning the effect on the polarization state of the radiation.

In the following this hypothesis is not assumed. The only assumption, (very strong actually), is that the role of the optical element splitting the total signal from the P and S signals in the receiving apparatus is polarization independent.

Under this hypothesis we can write the total elastic backscattering signal as a linear combination of S and P signals :

$$P_T(z) = G\left[P(z) + HS(z)\right] \tag{4.16}$$

In eq. (4.16) G is a constant value, $P(z)$ the Lidar signal collected by the P channel, expressed in eq.(4.1) $S(z)$ the Lidar signal collected by the S channel, expressed in eq.(4.2)

and H is again the calibration constant, defined as $H = \frac{k_{//}}{k_{\perp}}$, where $k_{//}$ and $k_{\perp}$ are the efficiencies of the P and S channels respectively.

If we perform a linear fit of the measured $P_T(z)$, with the function (4.16), S and P channels, we can retrieve the H constant. In this fit we must exclude the lowest altitudes from the calculus, in order to avoid the problems linked to the effects of the different overlap function of the detection channels.

It's important to focus here that this method can be applied only if a Lidar system can dispose of the P, S and the P_T channels, and also if the signal in P_T channel can be written as in (4.16). Therefore this calibration technique cannot be applied in Napoli Lidar system, where the total channel was not included in the realized setup, while it can be applied in Potenza Lidar setup, where this channel is present.

4.4 Sensitivity analysis of the calibration techniques

The simulation is a reliable tool for a sensitivity analysis, with the possibility to vary the initial conditions to test the performances of the different calibration techniques. It is based on a simulation of the real experimental conditions, supposing a known atmosphere (hypothesis of the simulation) and checking the results of the outputs with respect to the initial hypothesis. In the following a detailed description of the conditions and the results of the simulation will be done.

Air density and the Rayleigh scattering coefficient are simulated by a standard atmospheric model (U.S Standard Atmosphere) fitted to temperature and pressure values (20°C, 1bar) at the ground level. Up to 1.5 km of altitude, a typical planetary boundary layer (PBL) aerosol with $\beta \cong 1 \sim 5 \times 10^{-6}\ sr^{-1}\ m^{-1}$, LR=70~80sr, and an aerosol depolarization ratio of 0.03 [4.5] was simulated. Between 3~4 Km an aerosol layer characterized by LR=40sr and an aerosol depolarization ratio of 0.05 was supposed. Between 4.5~5 Km a Saharan desert mineral dust layer was simulated with LR=40sr, and aerosol depolarization ratio of 0.2 [4.9] for the second case was supposed. A cirrus cloud ($\beta = 8.10^{-6} sr^{-1} m^{-1}$, LR=30sr) and aerosol depolarization ratio of 0.3 [4.3] is also simulated in the 9~10Km altitude range. A vertical resolution of 60m is considered for the lidar signals. The depolarization ratio of the pure molecular contribution was chosen as 0.00376 [4.10].

The signals were simulated by choosing the apparatus parameters in order to reproduce the real conditions of measurements: the energy of the outgoing laser was fixed at 0.03J/pulse, considering the losses of the optical elements; the frequency of the laser equal is 20Hz, the overall system attenuation at 532 nm was considered equal to 0.01; the quantum efficiency of PMT was set different for the two channels, for P equal to 0.05 and equal to 0.1 for S. The radius of the telescope is 0.15m, the instrumental depolarization was considered 0.002, and the solar background equal to 0.1 in arbitrary units. The offset angle (the misalignment of P and S channel with respect to the laser direction of laser polarization) is fixed at 0.2 degree. The received signals from the two channels are simulated from the equation of the Lidar signals. In the simulated signals, only the statistic error was considered, so the variability of the atmosphere is neglected. The altitude range of the signals was taken from 30m to39990m. The signals were averaged over 10 minutes.

The aerosol depolarization ratio δ^a can be obtained from the equation (4.1) and (4.2):

$$\delta^a = \frac{(1+\delta^m)\delta R - (1+\delta)\delta^m}{(1+\delta^m)R - (1+\delta)} \tag{4.16}$$

[4.8].Where δ is total or volume depolarization coefficient, δ^m is the molecular depolarization ratio, and $R = \frac{\beta^m + \beta^a}{\beta^m}$ is called the backscatter ratio, where β^m is the total molecular backscattering coefficient and β^a is the total aerosol backscattering coefficient. Based on the equation of the elastic Lidar signals for the parallel and perpendicular components the signals can be simulated.

The total depolarization ratio, obtained from the output of the simulation, was compared with the hypothesis of the simulations (4.16).

The molecular method uses the molecular signal as the calibration signal. In (4.5) and (4.6) are reported the equations for channels S and P due only to molecular contribution. The calibration constant is expressed by the formula (4.7), that we write again here considering the subtraction of the background for both components:

$$H = \frac{\sum_{i=1}^{n} (P_m(z_i) - b_p)}{\sum_{i=1}^{n} (S_m(z_i) - b_s)} \left(\frac{\delta_{mol} + k}{1 + k \cdot \delta_{mol}} \right) \tag{4.17}$$

For this method it is very important to find a proper range free from aerosols. The background is calculated as the average of the signals at very high altitudes.

To this purpose the range was chosen as (25 Km, 30 Km).

From the fit of the signals with the molecular profile in a proper range we obtain the coefficients $a_{//}$ and $a\perp$.

$$P_m(z) = a_{//} P_{mol}(z) \tag{4.18}$$
$$S_m(z) = a_{\perp} P_{mol}(z) \tag{4.19}$$

Then the error of the gain ratio can be obtained as:

$$\Delta H = \sqrt{\left(\frac{\partial H}{\partial k}\Delta k\right)^2 + \left(\frac{\partial H}{\partial a_{\perp}}\Delta a_{\perp}\right)^2 + \left(\frac{\partial H}{\partial a_{//}}\Delta a_{//}\right)^2 + \left(\frac{\partial H}{\partial b_p}\Delta b_p\right)^2 + \left(\frac{\partial H}{\partial b_s}\Delta b_s\right)^2} \tag{4.20}$$

A graph of a typical well-done fit for P and signals, normalized to molecular level between 6 and 7 Km is reported in fig.4.3.

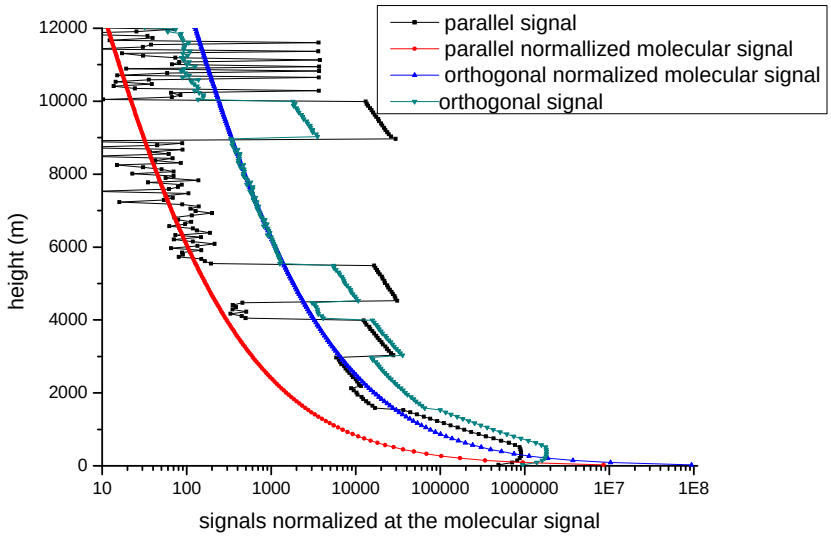

Fig.4.3 Parallel and orthogonal signals, normalized at the molecular one in the range between 7 and 7.5 Km

The second method calibration is obtained in two steps: 1) performing a regular

measurement and 2) by turning the laser by 90 degrees.

The two couples of signals in P and S channels are described by the equations (4.1)-(4.2) and (4.8)-(4.9).

We start supposing the atmosphere stable between the two measurements.

The gain ratio can be obtained from the equation (4.10), that is reported again here with the background subtraction from the measured signals:

$$H = \sqrt{\frac{(P_2(z) - b_{2p}) \cdot (P_1(z) - b_{1p})}{(S_2(z) - b_{2s}) \cdot (S_1(z) - b_{1s})}} \tag{4.21}$$

The error of the gain ratio in this case is calculated as:

$$\Delta H = \sqrt{\left(\frac{\partial H}{\partial P_2}\Delta P_2\right)^2 + \left(\frac{\partial H}{\partial b_{p2}}\Delta b_{p2}\right)^2 + \left(\frac{\partial H}{\partial P_1}\Delta P_1\right)^2 + \left(\frac{\partial H}{\partial b_{p1}}\Delta b_{p1}\right)^2 + \left(\frac{\partial H}{\partial S_2}\Delta S_2\right)^2 + \left(\frac{\partial H}{\partial b_{s2}}\Delta b_{s2}\right)^2 + \left(\frac{\partial H}{\partial S_1}\Delta S_1\right)^2 + \left(\frac{\partial H}{\partial b_{s1}}\Delta b_{s1}\right)^2} \tag{4.22}$$

In this case the calibration constant is independent on the range. Therefore, in principle, we can consider the signals at all altitudes and take the weighted average of the values of H. Anyway the signals at low altitudes that can be affected by overlap factors are excluded from the average.

Then the error on the gain ratio can be obtained from the propagation of the errors.

In the third method two couple of elastic signals were used as the calibration signals which were obtained by turning the laser by 45 degree in the two opposite directions. The calibration signals can be described by equations (4.11-4.14)

The gain ratio can be obtained as:

$$H = 0.5 \cdot \left(\frac{P_2 - b_{p2}}{S_2 - b_{s2}} + \frac{P_3 - b_{p3}}{S_3 - b_{s3}}\right) \tag{4.23}$$

In this case, the calibration is independent on the range. In order to reduce the statistical error the expression of the gain ratio 4.23 is replaced by the weighted average, considering the signals at every altitudes, but also here it will be excluded the low altitudes, where the signals can be affected by the overlap factors.

The total error on the gain ratio (calibration constant) is obtained from the propagation of the errors.

If the atmosphere remains stable, the error of the second method is similar to the one corresponding to the first method.

$$\Delta H(z) = \left(\begin{array}{l} (\frac{\partial H}{\partial P_2}\Delta P_2(z))^2 + (\frac{\partial H}{\partial P_3}\Delta P_3(z))^2 + (\frac{\partial H}{\partial S_2}\Delta S_2(z))^2 + (\frac{\partial H}{\partial S_3}\Delta S_3(z))^2 + (\frac{\partial H}{\partial b_{p2}}\Delta b_{p2})^2 + (\frac{\partial H}{\partial b_{p3}}\Delta b_{p3})^2 \\ +(\frac{\partial H}{\partial b_{s2}}\Delta b_{s2})^2 + (\frac{\partial H}{\partial b_{s3}}\Delta b_{s3})^2 \end{array} \right) \quad (4.24)$$

4.4.2 Analysis of the simulation

The results of the simulation for depolarization ratio are showed in the following figures for the different calibration methods.

In fig.4.4 the total depolarization ratio together with the exact value are reported. A range for the normalization at the molecular value was chosen from 6 to 8 Km.

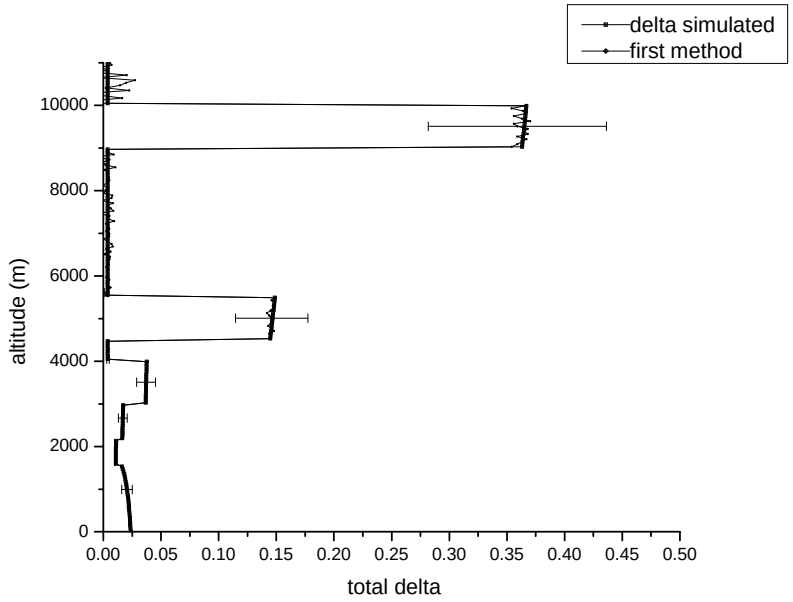

Fig. 4.4 Comparison of the total depolarization ratio vertical profile obtained by calibrating with molecular contribution and the simulated profile.

In figure 4.5 the comparison between the total depolarization ratio, obtained with the second method of calibration and the exact value are showed.

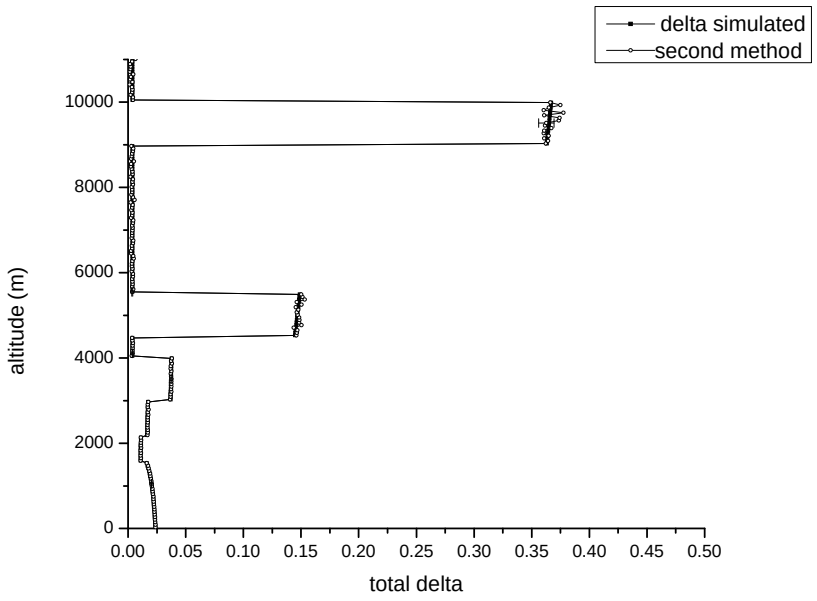

Fig.4.5 Comparison results between total depolarization ratio simulated and obtained using the second calibration technique based, supposing a no-change in atmosphere.

It is clearly evident that this calibration technique leads to lower error than the first one. Anyway, this method can be applied only if the atmosphere is stable during the calibration. To evaluate the sensitivity to atmospheric changes, a simulation of the atmospheric changes between the two set of measurements was performed by varying the aerosol backscattering coefficients in the following way:

$$\beta_{ac} = \beta_a + \beta_a \cdot 10\%(30\text{m} \sim 1470\text{m})$$
$$\beta_{ac} = \beta_a - \beta_a \cdot 10\%(3030\text{m} \sim 3990\text{m})$$
$$\beta_{ac} = \beta_a + \beta_a \cdot 10\%(4530\text{m} \sim 5490\text{m})$$
$$\beta_{ac} = \beta_a - \beta_a \cdot 10\%(9030\text{m} \sim 9990\text{m})$$

In fig.4.6 it is represented the graph of the total depolarization ratio in the case of the atmospheric changes

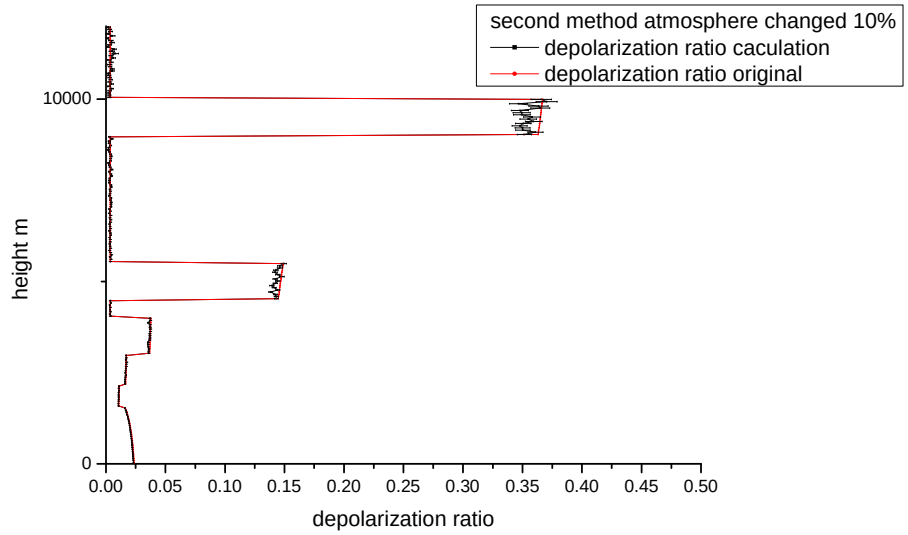

Fig.4.6 Comparison between total depolarization ratio simulated and that one obtained using the calibration technique based on polarization rotation of ninety degrees, supposing a 10% change in the atmospheric backscattering.

The relative error of total depolarization obtained from the two-steps or 90° rotation calibration procedure for the three aerosol layers is around 3% when the atmosphere is supposed stable. If a variability of the atmospheric parameters (i.e. the backscattering and extinction profiles) of about 10% is introduced, the relative error from the two steps method grows up to about 3%~9%.

The third calibration procedure requires two steps: a rotation of the polarization direction of the laser by 45 degree and a new rotation by 45 degree but in the opposite direction. Even though two steps are required, this calibration method results insensitive to atmospheric instability. In figure 4.7 the results obtained by applying the third calibration method to simulate signals are shown.

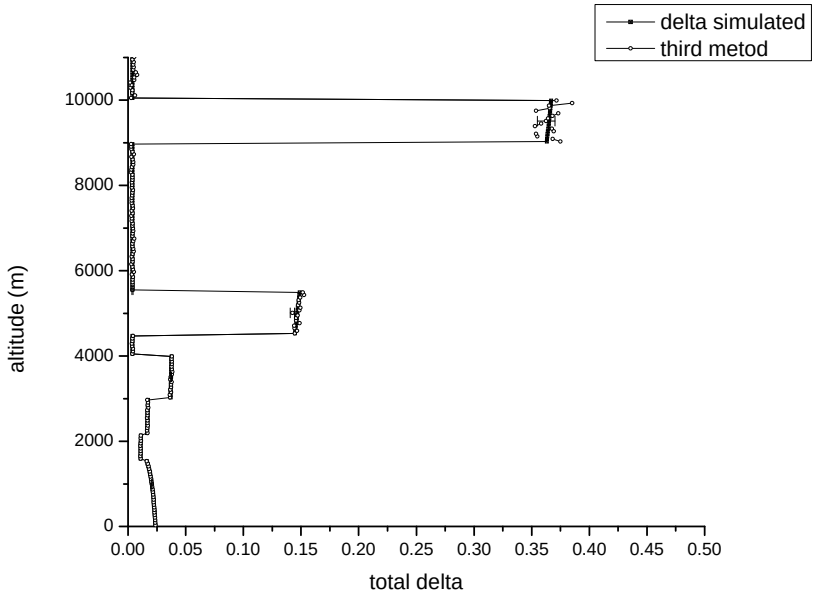

Fig. 4.7 Comparison results between total depolarization ratio simulated and obtained using by the three-steps calibration technique with a 10% of change in the atmosphere

The third method results to be almost independent on atmospheric variability. In fact, no appreciable changes in the results are obtained also if values of the atmospheric parameters are changed by 50%.

The figures 4.8, 4.9, 4.10 show the relative errors of the depolarization ratio coefficient as functions of the instrumental depolarization, at three different altitudes (3510m, 5010m, 9010m). These altitudes correspond to: an aerosol layer characterized by an aerosol depolarization ratio equal at 0.05 (3510m), a Saharan dust aerosol layer characterized by an aerosol depolarization ratio equal at 0.2 (5010m), and at the end , to a cirrus cloud layer with a depolarization ratio equal at 0.4 (9010m).

In general, the relative error on the depolarization ratio increases with the increasing of the instrumental depolarization.

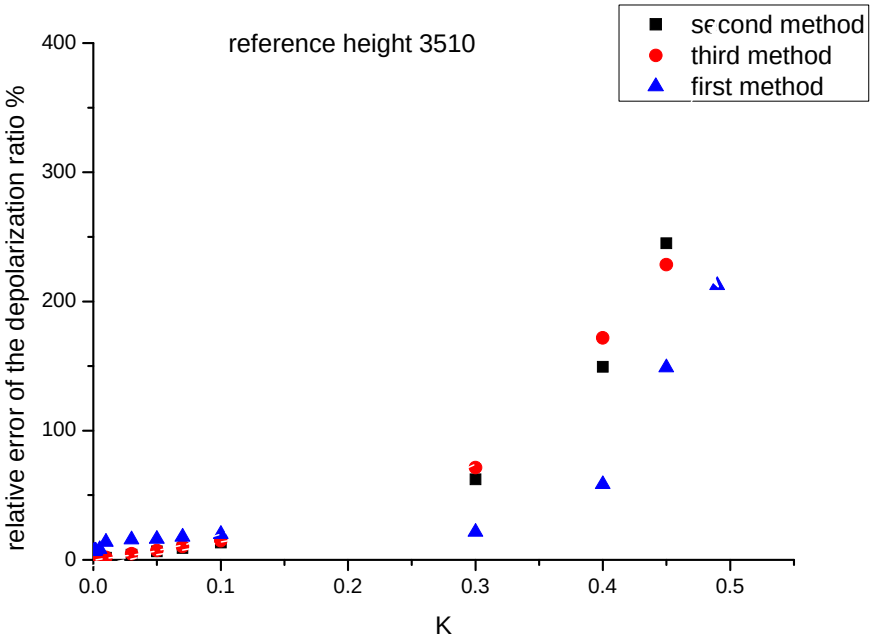

Fig.4.8 Relative error on depolarization ratio as a function of the instrumental depolarization at a height of 3510 m

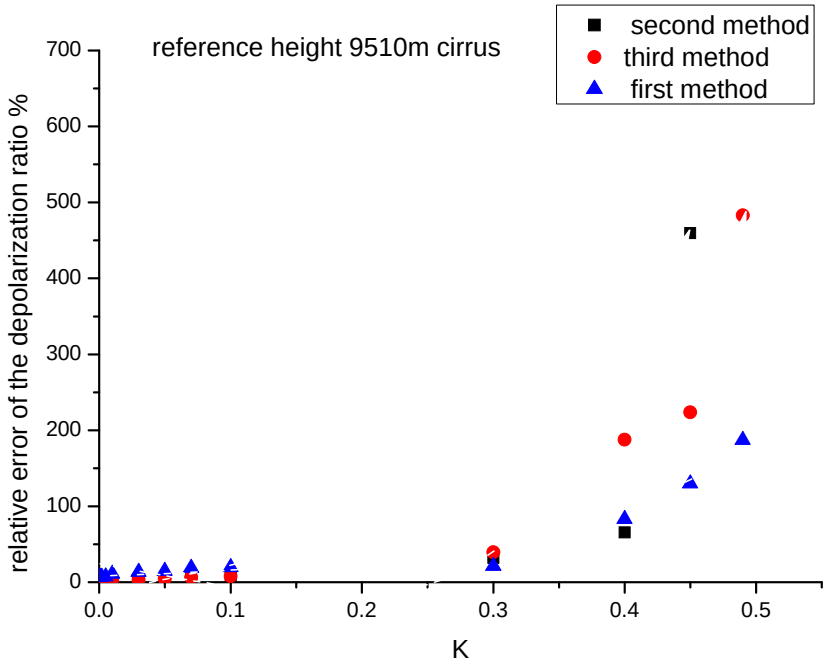

Fig.4.9 Relative error on depolarization ratio as a function of the instrumental depolarization at a reference height of 9510 m

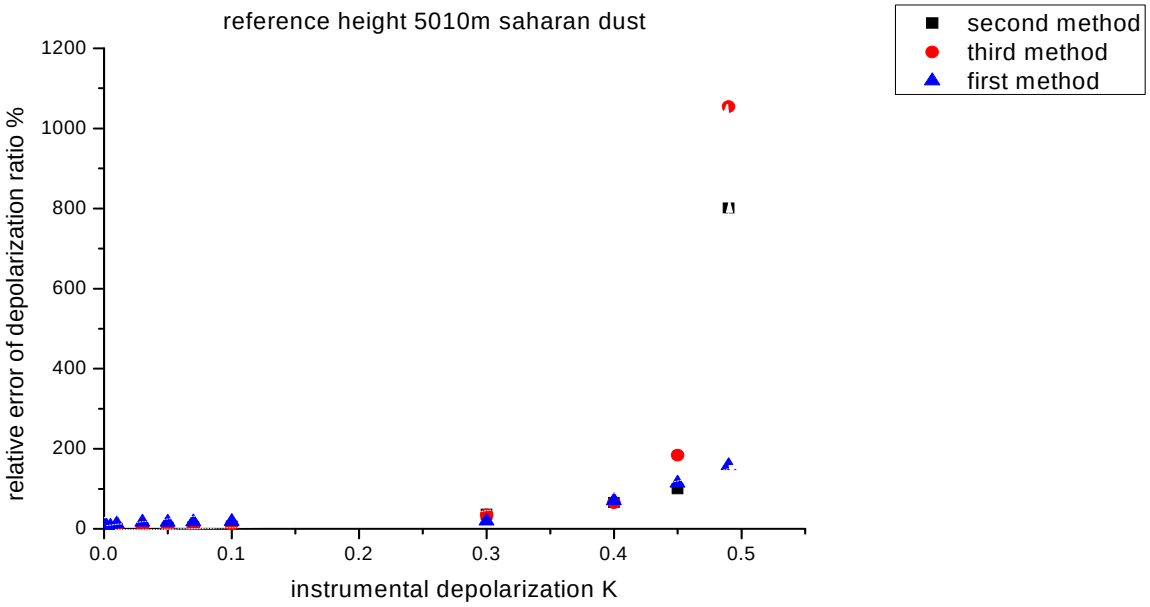

Fig.4.10 Relative error on depolarization ratio as a function of the instrumental depolarization at a reference height of 5010m for the three calibration techniques

The following figures show as the relative error on the depolarization ratio and of the gain ratio varies with the background for the three different aerosol layers. Obviously, the relative error will grow up with the increasing of background. Anyway for the first method the relative error of the depolarization ratio goes up most sharply with respect to the other methods. For the second and third method the relative error of the depolarization ratio will not exceed 5% at most. This means that for second and third method the relative error of the depolarization ratio is not so sensitive with respect to the background as the first one. For the other two aerosol layers the second method shows the lowest relative error on the depolarization ratio.

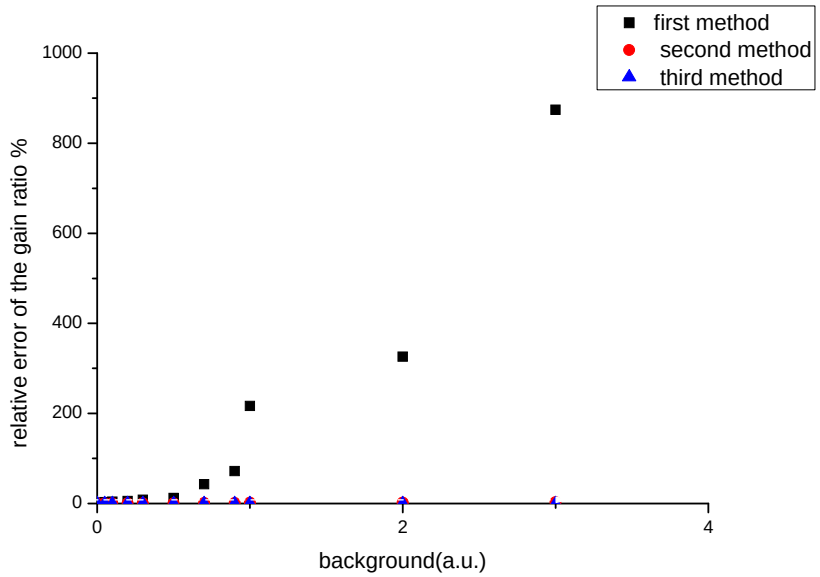

Fig.4.11 Relative error on gain ratio as a function of the background at a reference height of 5010m

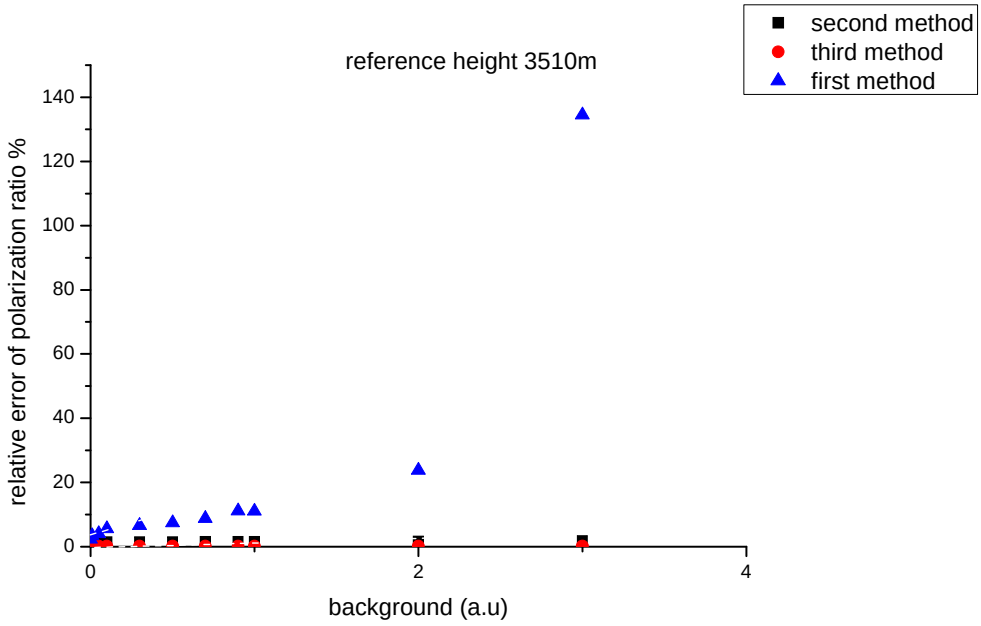

Fig.4.12 Relative error on the depolarization ratio as a function of the background at 3510 m

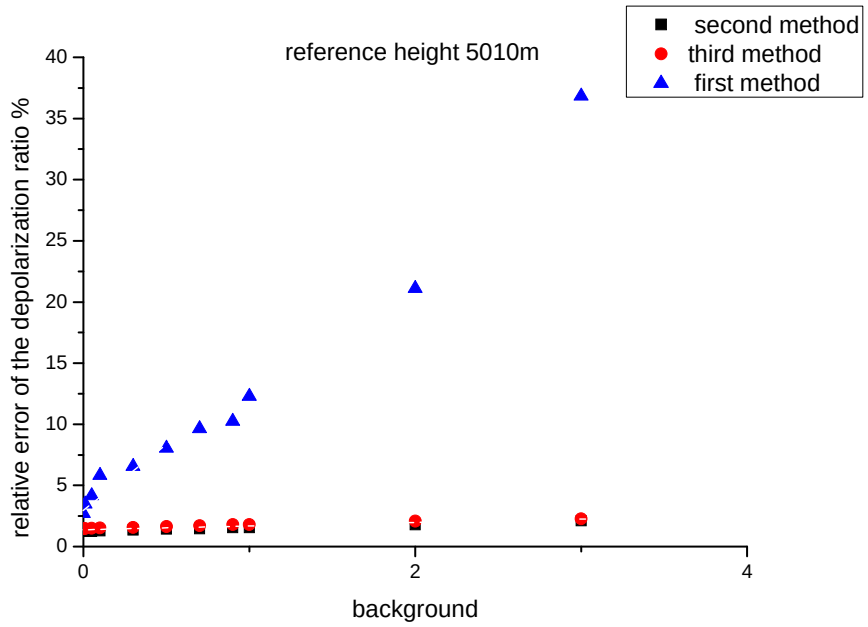

Fig.4.13 Relative error on the depolarization ratio as a function of the background at 5010m

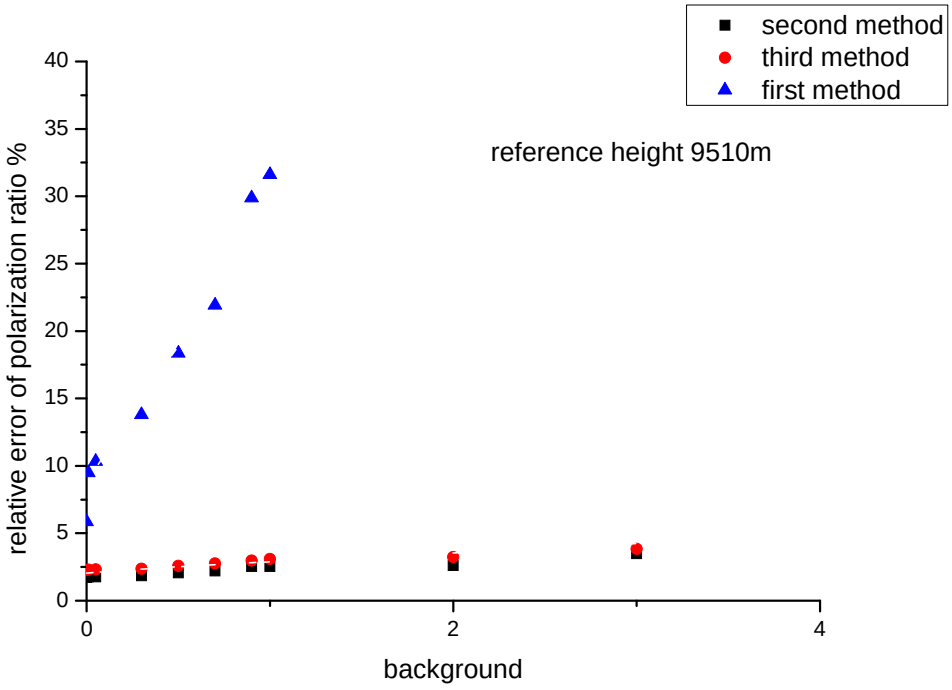

Fig.4.14 Relative error on the depolarization ratio as a function of the background at a reference height of 9510 m, for the three calibration methods

For each calibration method a proper range for the calibration should be chosen. In the following graphs the variability of the relative error on the gain ratio with respect to the amplitude of the range chosen for calibration is showed.

For the first case when the range is wider than 2000m, the relative error of the gain ratio does not change appreciably with the range amplitude, as showed in fig.4.15. Therefore, for the first case the range must be 2000m at least. For the second and third case the trend of the relative error on the gain ratio with respect to the amplitude of the range is decreasing. For the second case, the relative error of the gain ratio was $0.25\% < \Delta H < 0.32\%$, and for the third case $0.2\% < \Delta H < 0.27\%$ for amplitudes of the range between 1 and 7 Km..

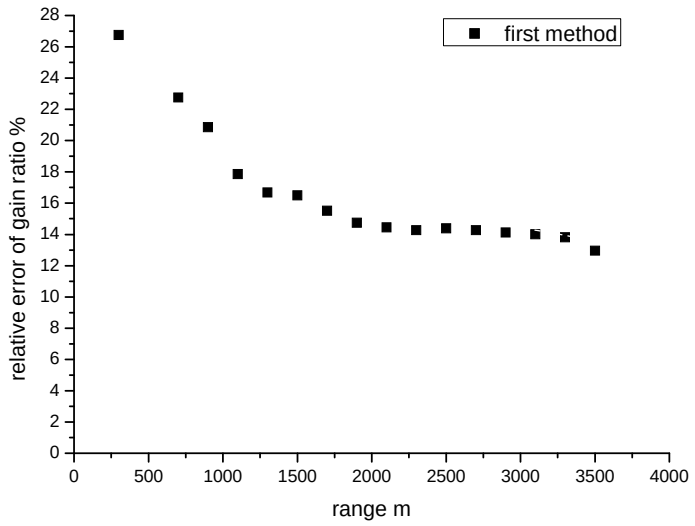

Fig.4.15 Relative error on the gain ratio vs. the amplitude of the range for the first calibration method.

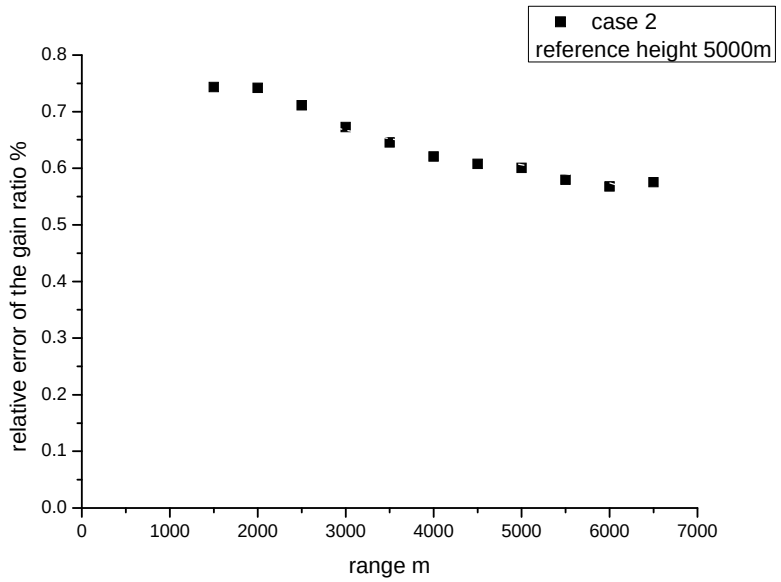

Fig4.16 Relative error on the gain ratio vs. the amplitude of the range for the second method

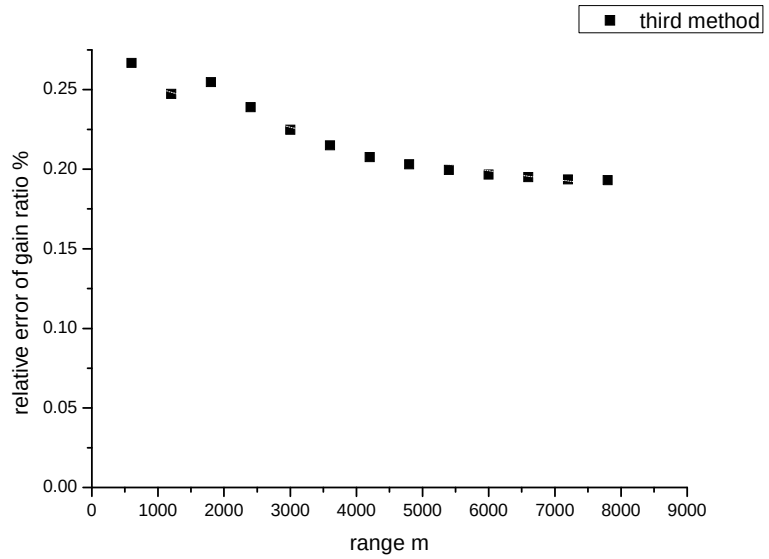

Fig.4.17 Relative error on the depolarization ratio vs. the amplitude of the range for the third method

On the basis of the results showed in the previous graphs, the amplitude of the range for the calibration was chosen as 2000m for the first method, 1000m for the second and third method. From the graph (4.19), it is evident that at the height of 9000m the relative error of the gain ratio achieved the first maximum. That is because this reference height was within the aerosol layer (a cirrus cloud in this case). For the first method the reference height

should be chosen in the layer without aerosol as the calibration signal was the molecular signal. At the high altitude, the error of the signal increases enormously, therefore the gain ratio also will have a bigger error. For the second and third methods the relative error of the gain ratio increases with the reference height. For the second method, there is the minimum point shown on the graph of fig.4.20, which was at the 4500m. This height corresponds to the aerosol layers. For the third method there is only one minimum at 9000m corresponding to the aerosol layer as shown in the graph 4.21. The relative error of the gain ratio varies with the reference height between $0 < \Delta H < 1.43\%$ and for the third method it is $0 < \Delta H < 2.72\%$. So both for the second and the third method the difference of the relative error of the gain ratio from the reference height is less than 3%.

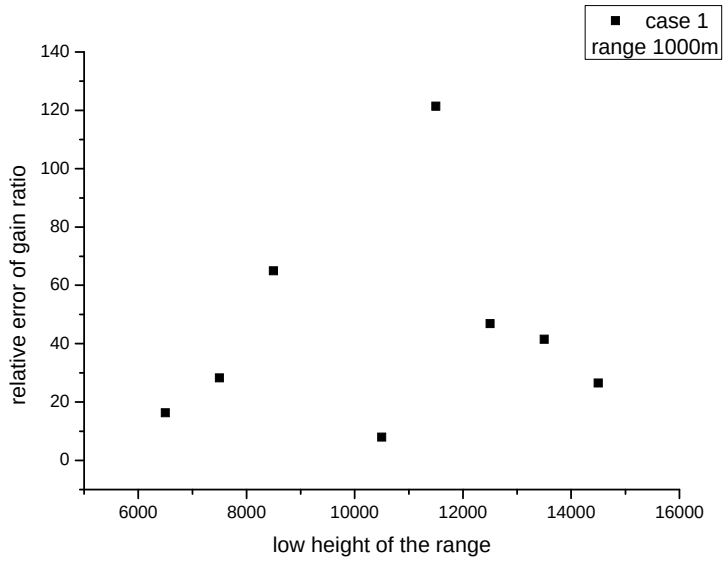

Fig.4 19 The relative error on the depolarization ratio vs. the range position for the first case

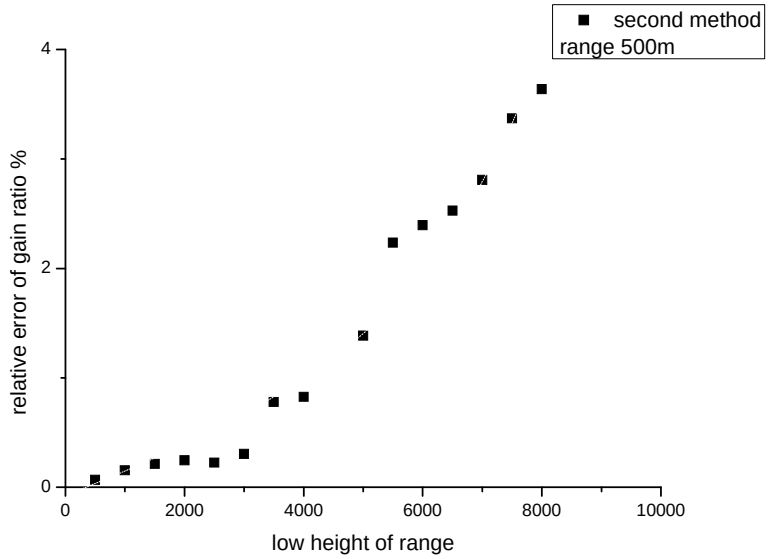

Fig4.20 The relative error on the depolarization ratio vs. the range position for the second method

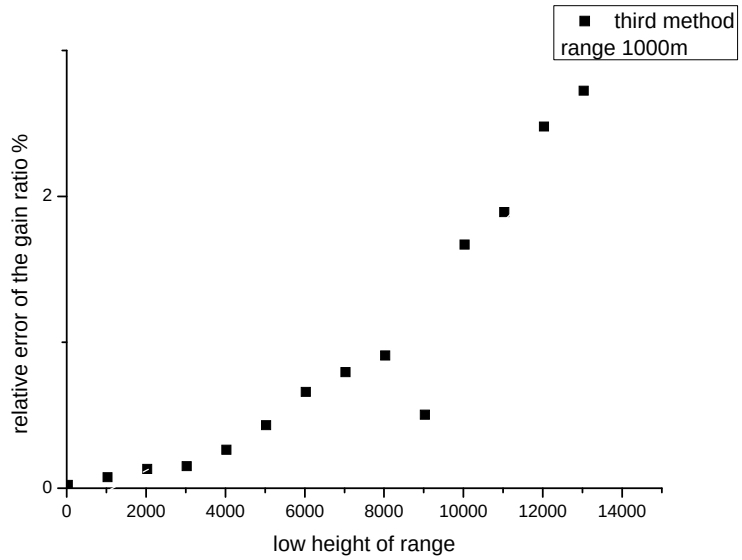

Fig4.21 The relative error on the depolarization ratio vs. the position of the range for the third method

For the third method another factor for the relative error also should be considered which is the error of the rotation angles. A variability of the rotation angle was simulated from 0 degree to 20 degrees and results are shown in the fig.4.22. The relative error of the depolarization ratio at the three different aerosol layers and the relative error of the gain ratio are all analyzed as functions of the error of the calibration angle. When the error of the

calibration angle is smaller than 5 degree, the relative error is lower than 2.7%. Above 5 degree the relative error of the gain ratio will increase sharply.

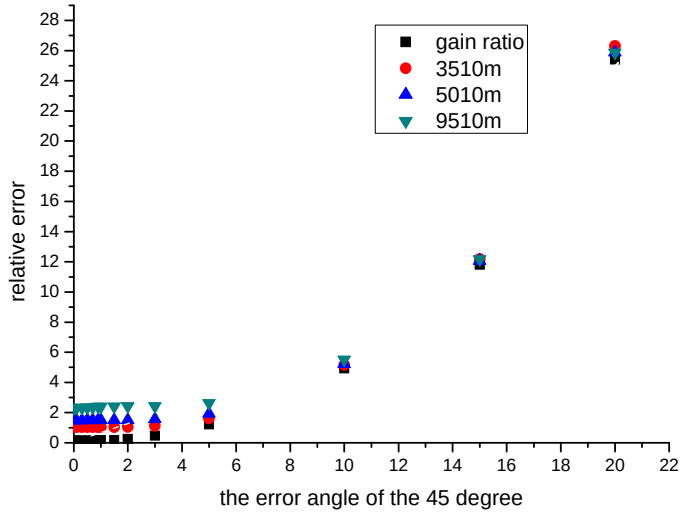

Fig.4.22 The relative error on the depolarization ratio and the gain ratio vs. the offset angle of the 45 degree

From the results of the simulation the offset angle, that is a measure of the misalignment between the receiver system and the direction of the propagation of the laser, will also introduce some errors.

For the first method the offset angle will introduce about 0.02% error. For second method it will introduce about 0.95% error. For third method it will introduce about 0.87%error. But if the offset angle is bigger than 0.5 degree the error from the offset angle will be more than 80% of the total error on the depolarization ratio.

4.5 Conclusion

In this chapter a comparative analysis of different calibration techniques to obtain total depolarization ratio from lidar simulated measurements is reported.

The first method performs an instantaneous calibration to the molecular backscattered signal by calibrating the signal on the molecular contribution in an aerosol free region. The advantage of this method is that the calibration is performed at the same time of each measurement. The main disadvantage is in the choice of the molecular range.

The second and the third methods are based on rotation of the polarization direction of the laser source by 90 degree and 45 degree in two opposite directions, respectively. These two methods need additional hardware in the optical path. Moreover, the second method is sensitive to atmospheric instabilities.

The three-steps method seems to be the most accurate and reliable in every atmospheric conditions.

The three signals method is a very powerful, useful and simultaneous calibration technique but it is limited by the characteristics of the apparatus.

4.6 References

[4.1] K.Sassen, 2000, *Lidar backscatter depolarization technique. Light Scattering by Nonspherical Particles,* M.I.Mishchenko, J.W.Hovenier and L.D.Travis, Academic Press, 393-416

[4.2] K.Sassen, 1991, *The polarization Lidar technique for cloud research: a review and current assessment.* Bull. American Society, **72,** 1848-1866

[4.3] R.M.Schotland, K.Sassen and R.Stone, 1971, *Observations by lidar of linear depolarization ratio for hydrometers,* J.Appl.Meteor.,**10,**1011-1017.

[4.4] V.Noel, H.Chepfer, G.Ledanois, A.Delaval and P.H.Flamant, 2002, *Classification of particle effective shape ratios in cirrus clouds based on the lidar depolarization ratio.* Applied Optics, **21,** 4245-4257.

[4.5] T.Murayama and Co-authors, 2001, *Ground-based network observation of Asian dust events of April 1998 in East Asia.* J.Geophys. Res., **107,** 8259, doi:10.1029/2001JD001303.

[4.6] D.M.Winker and M.T.Osborn, 1992, *Preliminary analysis of observations of the Pinatubo volcanic plume with a polarization-sensitive lidar.* Geophys. Res. Lett., **19,** 171-174.

[4.7] D.M.Winker, J.Pelon and M.P.McCormick, 2003: *The CALIPSO mission: Spaceborne lidar for observation of aerosols and clouds.* Proc.SPIE, **4893,** 1-11

[4.8] J.Biele, G.Beyerle and G.Baumgarten, 2000, *Polarization lidar: Correction of instrumental effects.* Optics Express **435,** Vol.7, No.12

[4.9] V. Freudenthaler et al., *Depolarization ratio profiling at several wavelengths in pure Saharan dust during SAMUM 2006,* 2009, Tellus, 61B, 165-179

[4.10] A.Behrendt and T.Nakamura, 2002, *Calculation of the calibration constant of polarization lidar and its dependency on atmospheric temperature.* Optics Express 805, Vol.10, No.16

[4.11] J.Reichardt et al., *Three-signal method for Accurate Measurements of Depolarization Ratio with Lidar,* 2003, Appl.Opt.4909-4913

[4.12] X.Wang,X.Lu,L.Nasti,Y.Zhao 2008, *Lidar measurements of aerosol depolarization ratio,* ***Chemical Engineering Transactions,*** Vol.16, ISBN 978-88-95608-03-7

Chapter 5

Calibration of the depolarization sensors of Pearl and Napoli Lidar systems

In this chapter the calibration techniques of the depolarization sensors applied at Potenza and Napoli Lidar systems will be discussed.
In the first part the calibration of the depolarization sensor in Napoli Lidar will be presented. An evaluation of the instrumental depolarization will be presented also.
In the second part, the PEARL (Potenza EARlinet Lidar) system will be described and the differences with respect to Napoli Lidar system will be highlighted. A description of the methodology and an explanation of the results I obtained during two months period (15 May-15 July 2009) of my PhD research time spent in C.N.R.-I.M.A.A.(Consiglio Nazionale delle Ricerche-Istituto di Metodologie per l'Analisi Ambientale) will be done.

5.1 Calibration of the depolarization sensor in Napoli

After the alignment procedure of the P and S channels, already described in chapter 4, the depolarization sensor of Lidar apparatus in Napoli was calibrated for the first time with $\pm 45°$ rotation technique on 30/04/2009, and real depolarization measurements started. In the fig.5.1 the temporal evolution of the gain ratio, obtained by the molecular and $\pm 45^0$ calibration procedures, is showed:

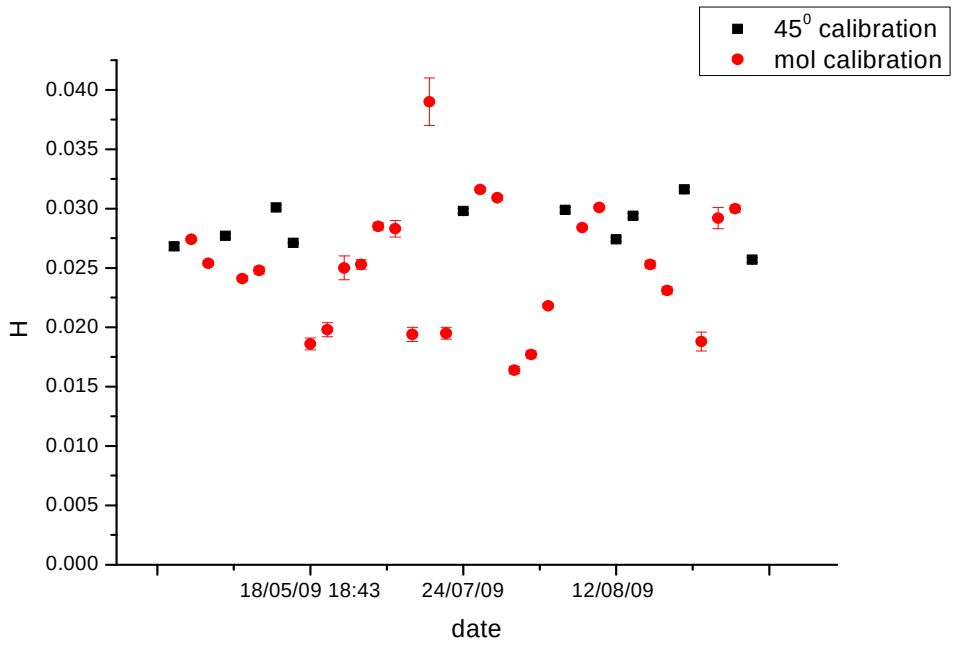

Fig.5.1 Temporal evolution of the gain ratio obtained with the $\pm 45^0$ calibration technique (black points) and with the molecular technique (red points) of the depolarization channels from 30/04/2009 to 07/09/2009

It's important to focus here that the errors on the single value of the calibration constant obtained by the $\pm 45^0$ calibration technique were calculated from the errors propagation starting from the errors on the signals used for the calibration. Therefore these errors do not take into account some factors:

1. the possible misalignment of the wave plate in the original position;
2. some possible imprecisions in the rotation steps
3. the sensibility error of the reader on the wave plate.

The best estimation of the constant is taken as the weighted average of these measurements.

Therefore, the average is $2.81 \cdot 10^{-2} \pm 6 \cdot 10^{-4}$. The error is taken as the standard deviation of the values.

In addition also the molecular calibration was performed for all those cases when the atmospheric conditions allow the determination of a "aerosol-free" range.

The average of values of the calibration constant from these measurements is $2.7 \cdot 10^{-2} \pm 1 \cdot 10^{-3}$. The two values of the calibration constants, obtained by the two

calibrations techniques for the first period of measurements are in agreement. Anyway, the molecular technique seems to be a calibration technique much less accurate than the $\pm 45^0$ calibration procedure and, in addition, it cannot be applied in each atmospheric condition as the other one.

After the end of September 2009 the system setup was modified, a new PMT, working in analog mode was added in the P-channel in order to extend the dynamic of the signal, and the attenuations of the channels were modified, then a new calibrations of the system was performed.
In fig. 5.2 the temporal evolution of the calibration constant, obtained by the two calibration techniques, is reported.

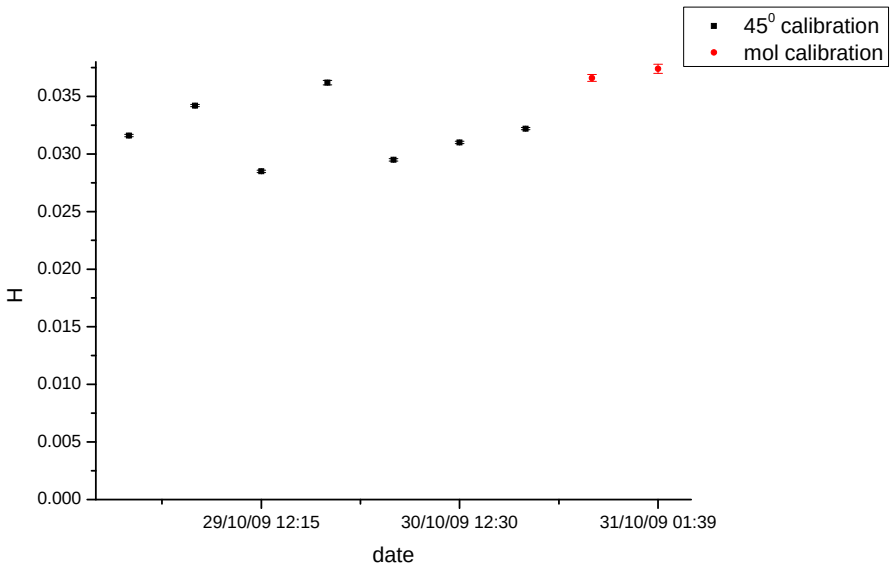

Fig.5.2 Temporal distribution of the gain ratio of the depolarization channels from 28/10/2009 to 30/10/2009

The best estimation of the constant for the $\pm 45^0$ technique is taken as the weighted average of these measurements. Therefore, it is $H = 3.1 \cdot 10^{-2} \pm 1 \cdot 10^{-3}$. Concerning the molecular calibration technique, because of the bad atmospheric conditions, it was applied only to two measurements. The best estimation of it is $H = 3.69 \cdot 10^{-2} \pm 4 \cdot 10^{-4}$.

Once obtained the calibration constant, it is also possible the evaluation of the instrumental depolarization *k.*

Considering the signals in a free-aerosol range, the overall instrumental depolarization, *k,* that includes the degree of polarization of the laser source, was obtained from the formula (see Chapter 4):

$$k = (\frac{S_m}{P_m} H - \delta_{mol})(1 - \frac{S_m}{P_m} H \delta_{mol})^{-1} \qquad (6.1)$$

In fig.5.3 is reported the distribution of all the values calculated for *k* for all the possible cases of measurements when this calculus was possible to perform:

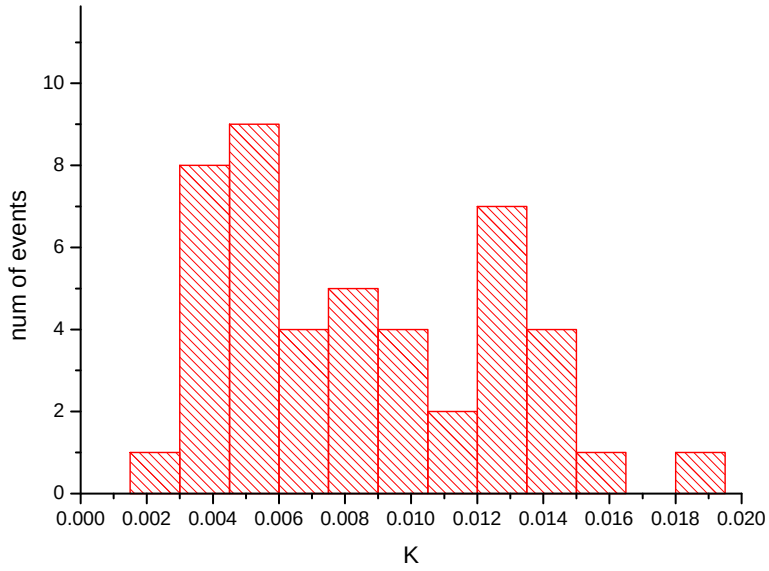

Fig. 5.3 Distribution of the k values of Napoli Lidar apparatus

The values of *k* vary from $1.61 \cdot 10^{-3}$ (under the value of the molecular depolarization) to $1.24 \cdot 10^{-2}$. The variability of *k* can depend by several factors: the variability of the room temperature , the different zero-position of the wave plate after each calibration procedure ($\pm 45^0$), and it is limited at the end by the error in the angular position of the wave plate. The interested reader can find in Appendix all the values founded for *k,* and for the calibration constant obtained with the two different and independent calibration procedures.

5.2 The Pearl setup

The PEARL system is a Multiparametric Raman Lidar system, with the presence of the depolarization channels for 532 nm and also of a channel for elastic signal detection at the 1064 nm wavelength.

In fig. 5.4 a scheme of the system is reported.

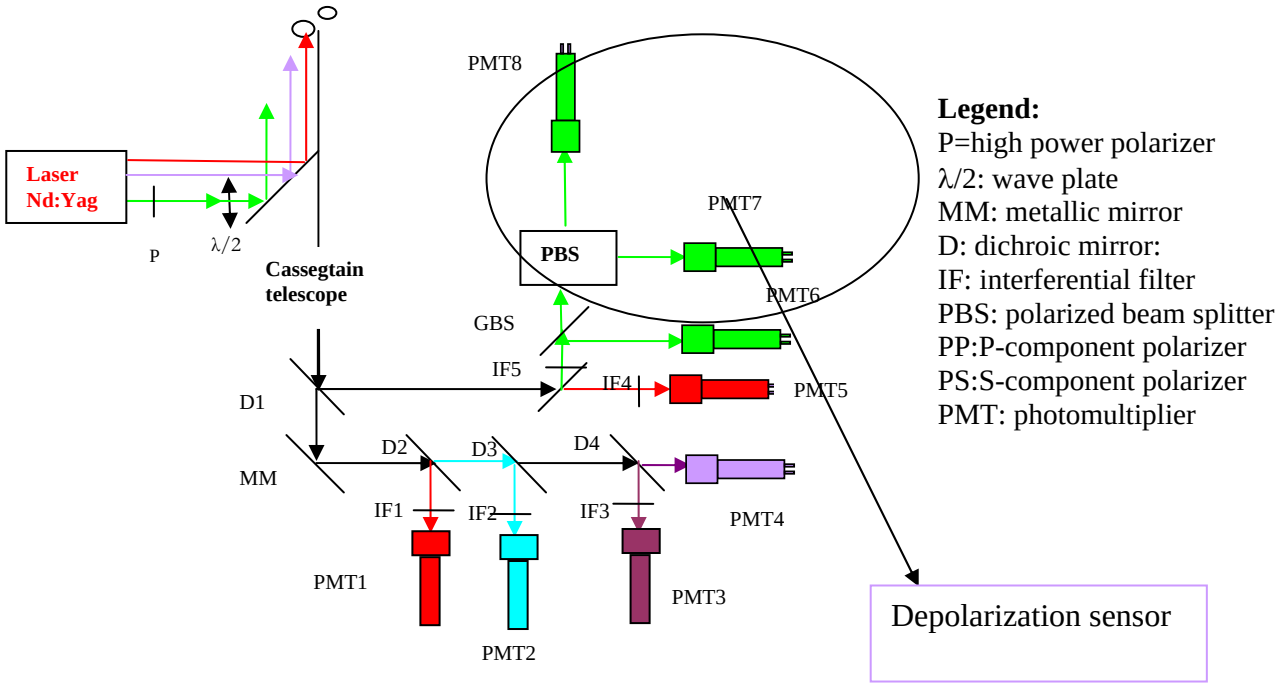

Fig.5.4 Pearl Lidar system

In table 1all the elements of the system and their function are reported:

Element	Function
D1	dichroic mirror: R: 532, 1064, T: 607,407,386,355
D2	dichroic mirror: R: 607, T: 407,386,355
D3	dichroic mirror: R: 407, T: 386,355
D4	dichroic mirror R: 386, T: 355
IF1	interferential filter @607 nm
IF2	interferential filter @ 407 nm

IF3	interferential filter @ 386 nm
IF4	interferential filter @1064 nm
IF5	interferential filter @ 532 nm
PMT1	photomultiplier@ 607 nm
PMT2	photomultiplier@407nm
PMT3	photmultiplier@386 nm
PMT4	photomultiplier@355nm
PMT5	APD avalanche photodiode @1064 nm
PMT6	photomultiplier@532nm (P+S)
PMT7	photomultiplier@532nm (P component)
PMT8	photomultiplier@532nm (S component)

Table 5.1 Principal element of the Pearl Lidar setup

The Lidar system in Potenza has two principal differences with respect to that one in Napoli:

1) in the transmission system there is a $\lambda/2$ wave plate which has been used to align the depolarization sensor with the polarization direction of the laser and then it has been fixed, therefore no 90° or $\pm 45°$ calibrations were possible to perform;
2) In the receiving system a beam splitter nominally not sensitive to the polarization state of the beam was inserted to separate the total backscatter radiation from the two polarized S and P components that were separated by a polarizing cube beam-splitter (PBS).

5.3 Calibration of the PEARL depolarization sensor

The Lidar group in Potenza performed depolarization measurements since September 2007. Anyway the data were not calibrated. In this situation I started to calibrate the system using the molecular method following the calibration procedure described in the previous chapter.
It's important to focus here that, as showed in the chapter 4, it is impossible to determine the system depolarization (k) using only the molecular calibration technique, therefore it is necessary to suppose that the laser beam is 100% linear polarized, that the alignment of the depolarization sensor is perfect and no influence of the optical elements in the polarization of the beam is present.
In fig 5.5 the values of the calibration constant obtained from data recorded from September 2007 to September 2008 performing the molecular calibration are showed. In order to have high quality signals in the present analysis only nocturnal measurements without low clouds have been selected.

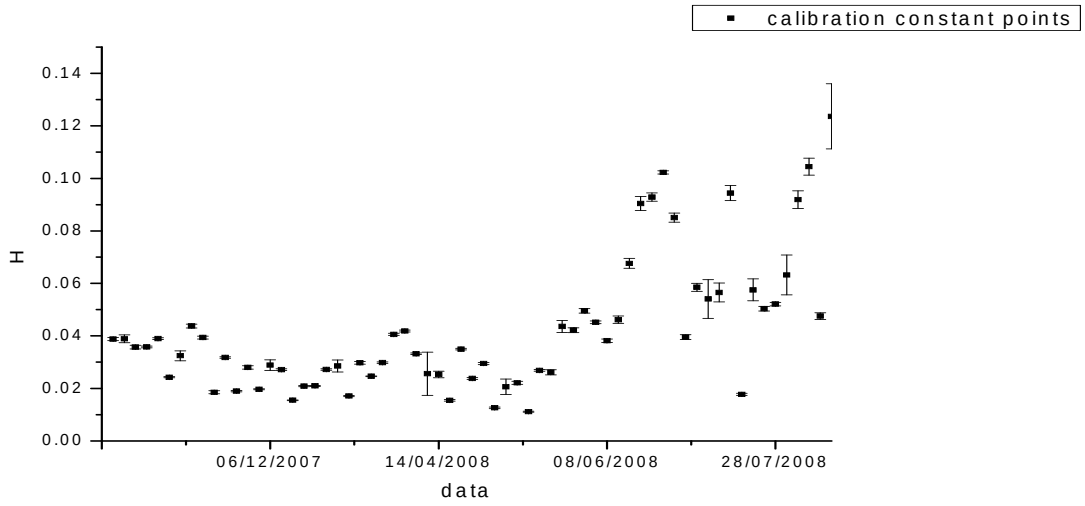

Fig.5.5 Temporal evolution of the calibration constant for Potenza Lidar apparatus from September 2007 to September 2008

The error on the single value of the constant is obtained from the propagation of the errors starting from the statistical errors on the signals. Therefore, it does not include the contribution of different conditions of each calibration: different range of calibration and some possible mistakes in the evaluation of the free-aerosol range. The average of the

values, excluding the instabilities of the system that appears in the last period (from May 2008), obtained from the calibration was: $2.4 \cdot 10^{-2} \pm 1 \cdot 10^{-3}$. Here the error is taken as the standard deviation of the values. In the last period some instabilities of the system appeared, due probably to some changes of the detectors' gain or of the attenuators.
When the instrumental conditions changed a new calibration was performed. In fig. 5.6 is showed the time dependence of the new calibration constant values.

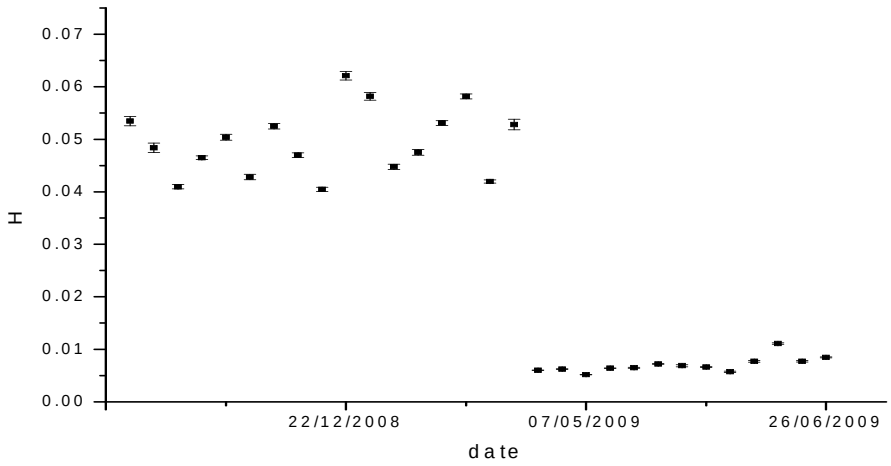

Fig.5.6 Temporal distribution of the calibration constant for Potenza Lidar apparatus from 29/09/2008 to 16/07/2009

The best estimation of the calibration constant for the second period was obtained again from the average before the 31 March 2009 (when another modification to the system underwent). The value of the constant this time is $4.7 \cdot 10^{-2} \pm 2 \cdot 10^{-3}$

In Potenza Lidar setup the depolarization sensor includes a so-called "total channel", therefore the calibration procedure that makes use of this channel, described in the previous chapter, was also tested and a comparison between the two techniques was done. If we calculate the total signal $T = P + HS$ where T is the total signal, P is the parallel and S is the orthogonal signal and H is the calibration constant obtained with the two different calibration techniques, we can compute the percentage deviation of these two composition signals as a function of the altitude. In the fig.5.7 the percentage deviation of the total signal

computed with the composition T of calculated with the molecular technique and the three signals technique is reported.

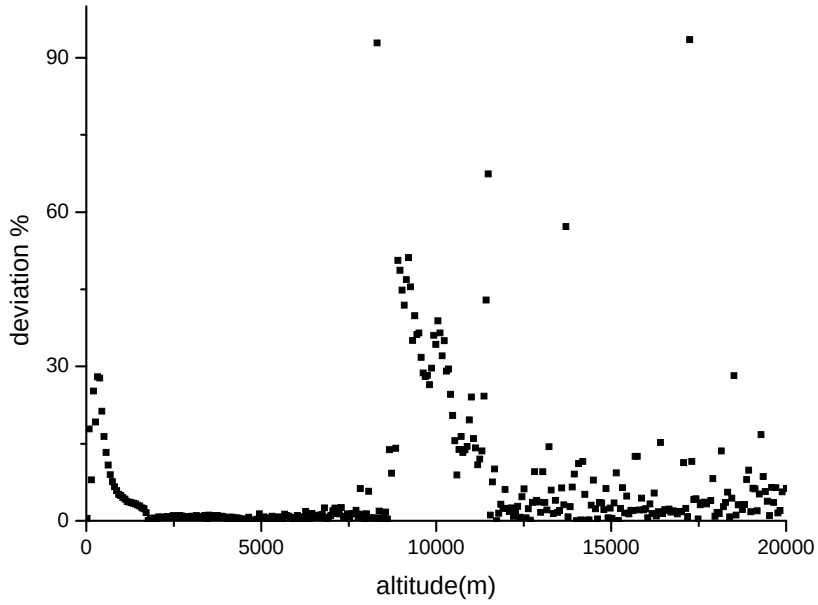

Fig.5.7 Percentage deviation as a function of the altitude between the calculated total signals (P+HS) obtained with the molecular calibration technique and the three signals calibration technique

The graph in fig.5.7 shows that where the depolarization is very strong (between 9 and 10 Km in this case, where a cirrus cloud is presented), the deviations between the two total signals obtained with the two different calibration techniques are on the order of 50% at maximum. If we change the molecular calibration constant in the range of variability determined by its maximum error the deviation vary from 40% to 60% at maximum.

This test shows that with a high probability the so-called “total signal” is actually a composition of S and P signals that underestimates the real contribution of S signal.

Therefore this test proves that this calibration technique can be applied only if the transfer function of the beam splitter is really independent by the polarization direction of the incident beam or if it can be measured with high accuracy.

5.4. Conclusions

In this chapter the calibration procedures explained in Chapter 4 were applied to two different depolarization sensors of different Lidar apparatus.

The two apparatus are the Multiparametric Raman Lidar of Napoli and the other is the PEARL system of Potenza.

In Potenza the molecular calibration technique was applied to calibrate nearly two years of depolarization measurements. Because of the presence of a third channel that nominally is the total signal, also a new calibration procedure was tested.

In Napoli the calibration procedures applied to the depolarization sensor of the Lidar apparatus were the molecular method and the $\pm 45^0$ technique. The second one seems to produce the most accurate results and also can be applied in every atmospheric conditions, as it was predicts in the simulation.

Chapter 6

Aerosol depolarization measurements

This chapter is devolved to the presentation of the first aerosol depolarization measurements in Napoli and in Potenza. In particular some relevant cases, followed by a brief discussion of the results, were selected from a collection of six months of measurements with the Multiparametric Raman Lidar in Napoli and nearly two years of measurements with the PEARL apparatus in Potenza.

6.1 Napoli aerosol depolarization measurements

In Napoli the aerosol depolarization measurements started on 30 April 2009.
In fig 6.1 is presented a very interesting case of observation.

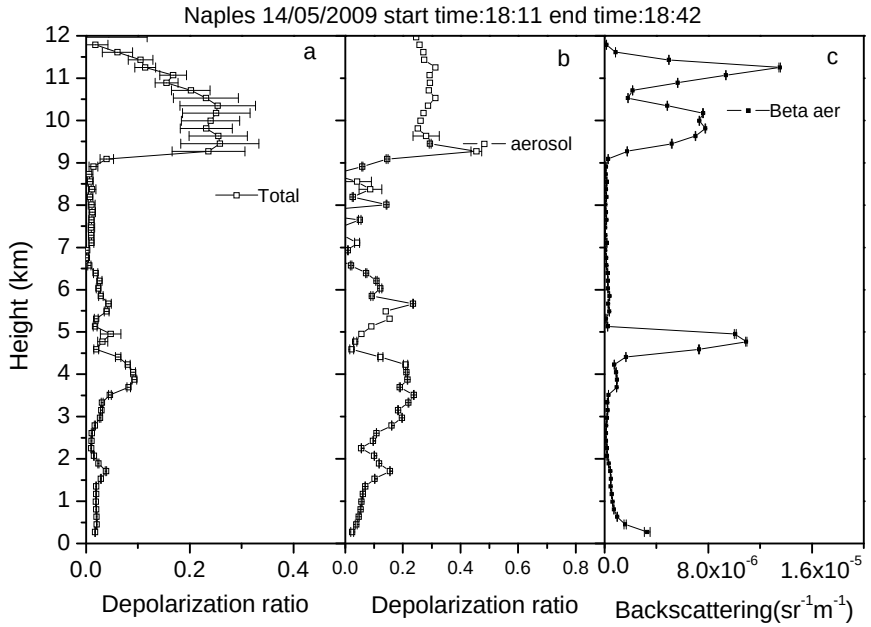

Fig,6.1 Napoli; total depolarization ratio (a), aerosol depolarization ratio (b), aerosol backscattering coefficient (c).Measurement case of 14 May 2009

In this example it is possible to distinguish different kinds of aerosol layers.

Up to 1 Km it is present a typical urban aerosol layer, that is characterized by low percentage of aerosol depolarization ratio [6.1], and a desertic dust layer from North Africa above the planetary boundary layer, between 2 and 4 Km, as it is evident in fig. 6.2, that shows the backward trajectories computed by NOAA Institute. The desertic dust is characterized by a relative low backscattering coefficient, but by a relative high depolarization coefficient, around 20% [6.2]. In addiction, between 4.5 and 5 Km there is evidence of a mixed phase clouds that backscatters a lot the signal but doesn't depolarize too much the backscattered radiation (only few percentages) [6.3]; between 9 and 12 Km a cirrus cloud, characterized by strong depolarization elements (ice crystals), depolarizes the backscattered radiation of about 40%[6.4].

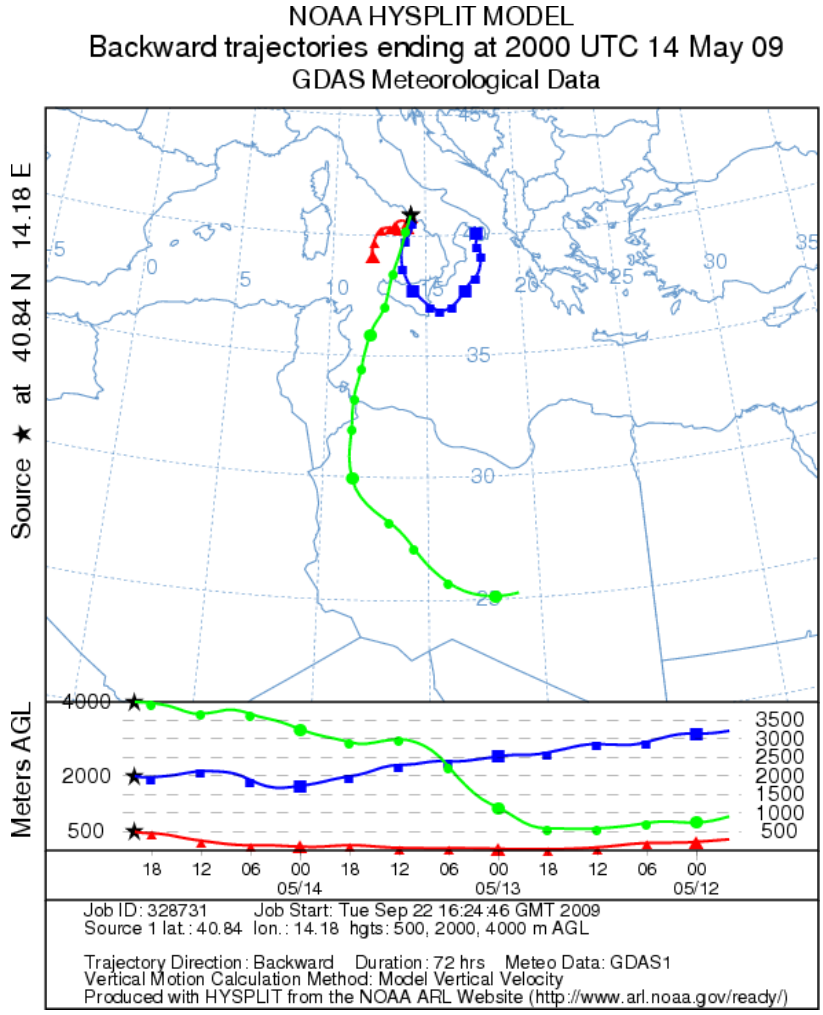

Fig,6.2 Backward trajectory plot computed by NOAA for a case of measurement of 14 May 2009

This measurements show how depolarization measurements are reliable tools to discriminate between the kind of aerosols (urban and natural aerosols) and between the phase of the clouds (mixed phase clouds from ice crystals clouds).
Another relevant case of measurement is reported in fig. 6.3 for a case of measurement of 24 May 2009.

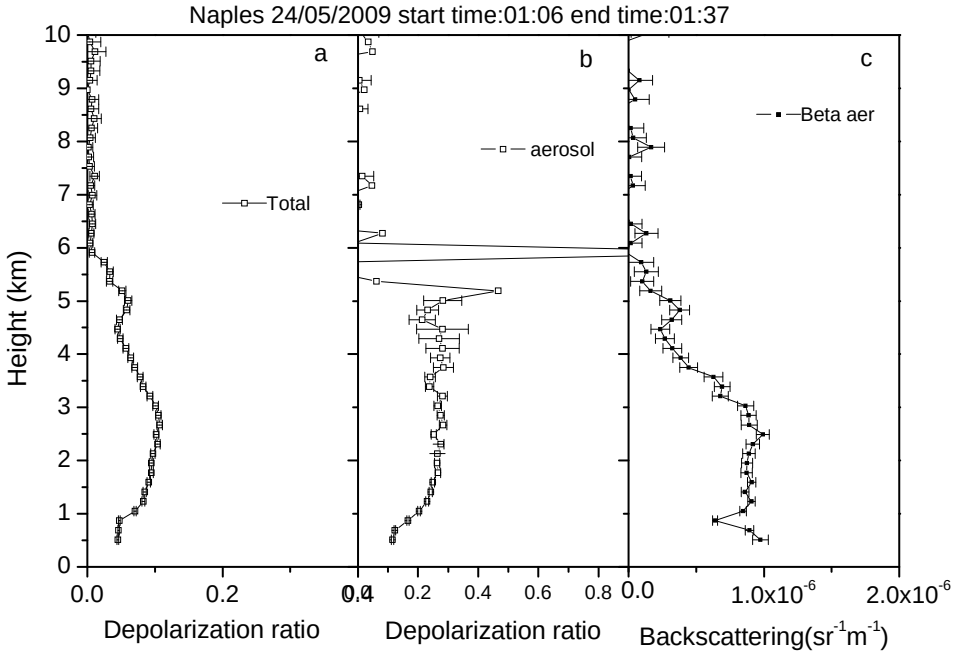

Fig,6.3 Napoli; total depolarization ratio (a), aerosol depolarization ratio (b), aerosol backscattering coefficient (c).Measurement case of 24 May 2009

This case shows an example of urban aerosol layer in the Planetary boundary layer, with a low values of depolarization ratio, and a well-defined desertic layer between 1 and 4 Km. Its aerosol depolarization ratio is around 30%, also compatible with the literature values [6.2]. In fig.6.4 are reported the backward trajectories, computed by NOAA Institute for this case of measurements.

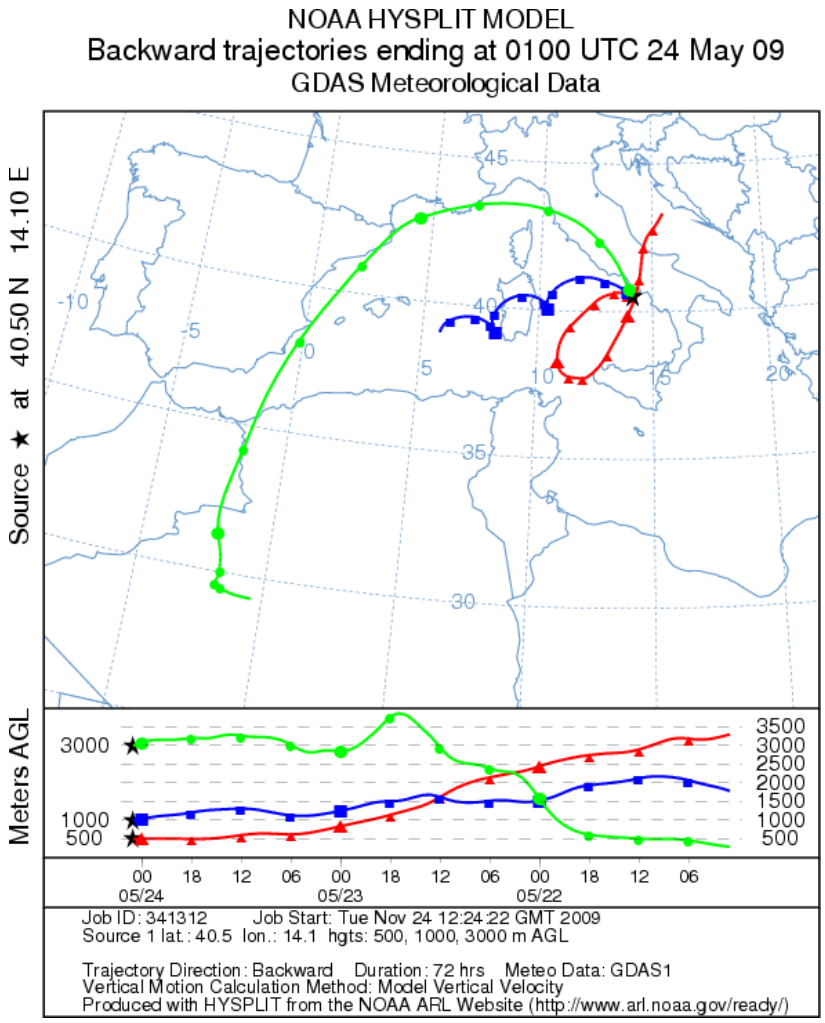

Fig.6.4 Backward trajectory plot computed by NOAA for a case of measurement of 24 May 2009

Finally, a most recent case of aerosol depolarization measurement is presented in fig.6.5.

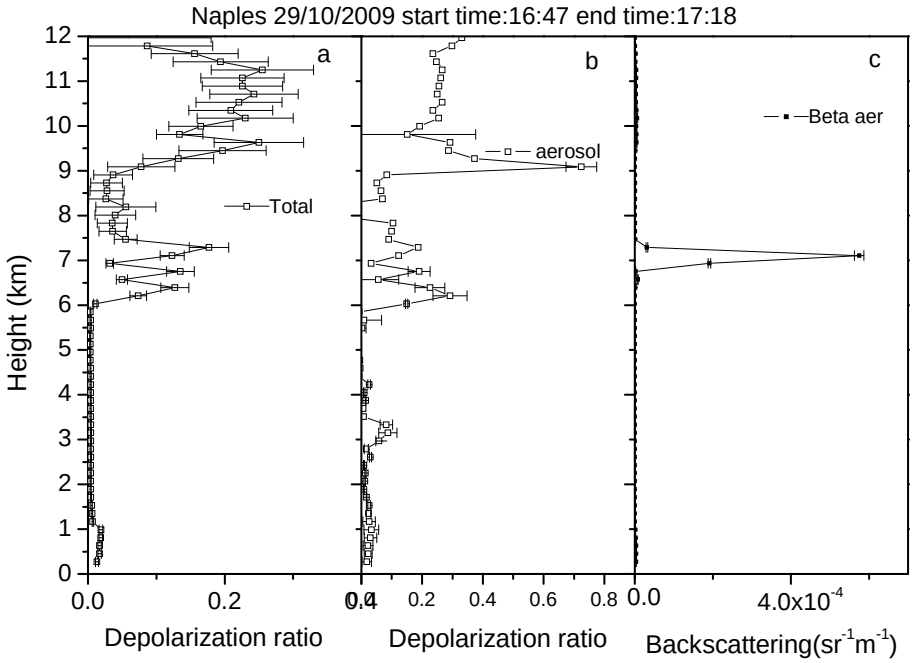

Fig.6.5 Napoli; total depolarization ratio (a), aerosol depolarization ratio (b), aerosol backscattering coefficient (c).Measurement case of 29 October 2009

This case shows the urban aerosol layer up to 1 Km. A long range of aerosol free atmosphere, a mixed phase cloud between 6 and 7 Km, characterized by a very high aerosol backscattering coefficient, and by a 10% of aerosol depolarization ratio. A 40% of aerosol depolarization ratio is also present between 9 and 12 Km.

6.2 Aerosol depolarization measurements in Potenza

In this paragraph some experimental results of the calibrated total and aerosol depolarization ratios, using data of Pearl Lidar station will be presented. In fig.6.6 it is showed a case of Planetary boundary layer aerosol (low depolarizing kind of aerosol) presented in the atmosphere up to 1 Km and a layer of Saharan dust between 2 and 5 Km; also a cirrus cloud, that is the strongest depolarization element is observed between 10 and 12 Km. The backward trajectories computed by the NOA Institute, showed that the layer between 2 and 5 Km is actually composed by Saharan particles.

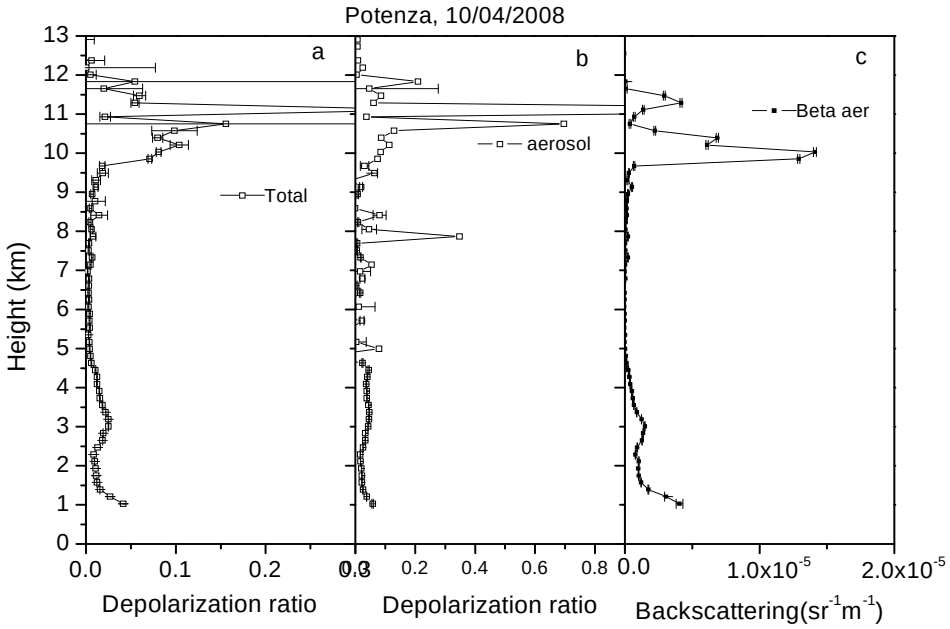

Fig.6.6 20 April 2008**,** Backscattering and total depolarization ratio of a measurement performed in Potenza

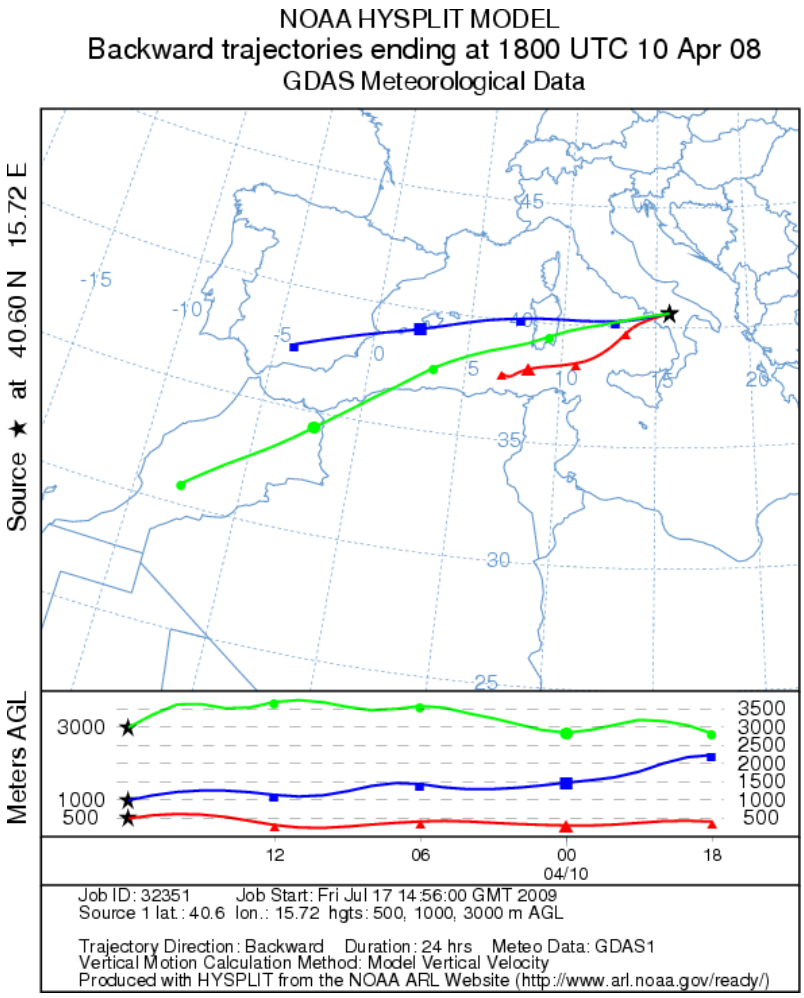

Fig. 6.7 Backward trajectories from NOAA

6.3 Conclusions

Some preliminary results of the total and aerosol depolarization ratio measurements, with the aerosol backscattering coefficients were presented in this chapter. The results show how the depolarization measurements are very useful tools in the discrimination of the kind of aerosols and in distinguish the phase of the clouds.

6.4 References

[6.1] Murayama, T. et al., *Depolarization ratio measurements in the atmospheric boundary layer by Lidar in Tokyo,* 1996, J.Meteorol. Soc. Japan **74,** 571-578

[6.2] Freudenthaler, V. et al., *Depolarization ratio profiling at several wavelengths in pure Saharan dust during SAMUM 2006,* 2009, Tellus **61B,** 165-179

[6.3] Sassen, K, *The polarization lidar technique for cloud research: a review and current assessments,*1991, Bull.Am.Meteorol.Soc.**72,** 1848-1866

[6.4] Schotland, R. et al., O*bservations by lidar of linear depolarization ratio for hydrometeors, 1971,* J.Appl.Meteorol. **10,** 1011-1017

Conclusions

In Napoli a Multiparametric Raman Lidar system, enhanced with the depolarization sensor, was designed and realized to improve the performance of the already Raman Lidar apparatus of the Laboratory of Atomic Physics and Laser Application in Physics Department of University Federico II.

From 30 April 2009 the depolarization measurements are available.

A key question in obtaining accurate depolarization measurements is in performing a careful calibration of the depolarization channels.

A particular relevance to this aspect was posed in this PhD work, through the theoretical evaluation of the performances of different calibration procedures by a numerical simulation.

In Napoli, experimentally, two procedures are applied and finally the $\pm 45^0$ rotation technique appears the most reliable and effective in each atmospheric condition.

In Potenza, where a period of two months was spent in I.M.A.A.-C.N.R. Institute, the depolarization sensor, already present in the Lidar apparatus was calibrated and a new technique was applied. In total nearly two years of data were analyzed.

In particular, the Napoli Lidar system, with the addition of the calibrated depolarization channel, is now able also in discriminating the aerosols' shape in atmosphere and in distinguishing the phase of the clouds. At present, in Europe only three Lidar stations can provide high-quality depolarization data: Hamburg, Munich and now Napoli.

The possibility to rotate the direction of polarization of the laser appears a really useful characteristic in order to obtain optimal depolarization measurements.

The critical points are constituted by the alignment between the receiving system and the laser and the right position of the wave plate.

About the real measurements, the effect of the solar background on the depolarization results appears more critical for the molecular calibration and for the evaluation of the instrumental depolarization. As it can be seen in the Appendix the calibration constant obtained by the molecular technique and the instrumental depolarization were evaluated mostly in night time. Anyway, the $\pm 45^0$ calibration procedure can be applied in any atmospheric conditions.

In future the Napoli Lidar system, with the depolarization sensor, will be able to do correlation studies with the other Lidar stations in Europe also in terms of the evaluation of the shape of aerosols, and the influence of transport phenomena. On a global scale, the aerosol's properties observed over Napoli, can be compared to the satellite Lidar system, like Calipso, equipped with Caliop (Cloud-Aerosol Lidar with Orthogonal Polarization) observations, to validate the satellite data.

Some specific studies about the correlation between multiple scattering, in terms of the optical depth, and depolarization coefficient are also in progress.

Appendix

Date	Calibration Constant H (±45° method)	Instrumental depolarization K	Calibration Constant H (molecular method)
30/04/09	2.68E-2 ± 3E-4		
01/05/09 00:02		1.02E-2 ± 4E-4	
01/05/09 00:33			2.74E-2 ± 1E-4
01/05/09 01:06		1.10E-2 ± 3E-4	
01/05/09 01:38			2.59E-2 ± 2E-4
01/05/09 02:09		1.2E-2 ± 2E-3	
06/05/09	2.77E-2 ± 2E-4		
08/05/09 00:00		1.19E-2 ± 2E-4	
08/05/09 00:31			2.41E-2 ± 2E-4
08/05/09 01:03		1.22E-2 ± 8E-4	
08/05/09 01:35			2.48E-2 ± 3E-4
08/05/09 02:06		1.24E-2 ± 9E-4	
08/05/09 12:00	3.01E-2 ± 2E-4		
11/05/09 18:20		6.3E-3 ± 4E-4	
13/05/09 09.21	2.710E-2 ± 8E-5		
14/05/09 18:11		1.2E-2 ± 1E-3	
18/05/09 18:43			1.86E-2 ± 5E-4
24/05/09 00:00		8E-3 ± 1E-3	
24/05/09 00:33			1.98E-2 ± 6E-4
24/05/09 01:06		8E-3 ± 1E-3	
24/05/09 01:38			2.5E-2 ± 1E-3
24/05/09 02:09		7.1E-3 ± 9E-4	
04/06/09 18:49			2.53E-2 ± 4E-4
09/06/09 00:06		5.4E-3 ± 8E-4	
09/06/09 00:37			2.85E-2 ± 3E-4
09/06/09 01:09		5.4E-3 ± 6E-4	
09/06/09 01:56			2.83E-2 ± 7E-4
11/06/09 18:53		4.8E-3 ± 8E-4	
18/06/09 00:00			1.94E-2 ± 6E-4
18/06/09 00:31		1.0E-2 ± 1E-3	
18/06/09 01:03			3.9E-2 ± 2E-3
18/06/19 01:34		9E-3 ± 1E-3	
18/06/09 02:05			1.95E-2 ± 5E-4
24/07/09	2.98E-2 ± 2E-4		
27/07/09 00:02		5.7E-3 ± 1E-4	
27/07/09 00:35			3.16E-2 ± 2E-4
27/07/09 01:13		5.4E-3 ± 1E-4	
27/07/09 01:48			3.09E-2 ± 2E-4
27/07/09 02:19		5.9E-3 ± 1E-4	
27/07/09 11:43			1.64E-2 ± 3E-4
27/07/09 12:14		1.20E-2 ± 5E-4	

27/07/09 12:46			1.77E-2 ± 3E-4
27/07/09 13:17		9.7E-3 ± 4E-4	
27/07/09 19:03			2.18E-2 ± 2E-4
30/07/09	2.99E-2 ± 2E-4		
05/08/09 00:01		8.7E-3 ± 4E-4	
05/08/09 00:32			2.84E-2 ± 1E-4
06/08/09 01:03		8.5E-3 ± 4E-4	
06/08/09 01:35			3.01E-2 ± 1E-4
06/08/09 02:06		8.2E-3 ± 2E-4	
12/08/09	2.74E-2 ± 2E-4		
21/08/09	2.94E-2 ± 2E-4		
28/08/09 00:04		1.3E-2 ± 1E-3	
28/08/09 00:35			2.53E-2 ± 3E-4
28/08/09 01:07		1.4E-2 ± 1E-3	
28/08/09 01:38			2.31E-2 ± 3E-4
28/08/09 02:09		1.4E-2 ± 1E-3	
28/08/09	3.16E-2 ± 2E-4		
03/09/09 18:00		1.37E-2 ± 1E-3	
06/09/09 00:01			1.88E-2 ± 8E-4
06/09/09 00:32		1.8E-2 ± 5E-3	
06/09/09 01:03			2.92E-2 ± 9E-4
06/09/09 01:38		1.58E-2 ± 8E-4	
06/09/09 02:00			3.00E-2 ± 3E-4
07/09/09 15:06	2.57E-2 ± 2E-4		
07/09/09 17:50		1.48E-2 ± 5E-4	

Table 1 Summary of the calibration informations on Napoli Lidar system's depolarization sensor for the period from 30 April 2009 to 07 September 2009

Date	**Calibration Constant H (±45° method**)	**Instrumental depolarization K**	**Calibration Constant H (molecular method)**
28/10/09 11:09		7.2E-3 ± 5E-4	
28/10/09 13:11	3.16E-2 ± 1E-4		
28/10/09 15:01	3.42E-2 ± 1E-4		
28/10/09 16:20		3.6E-3 ± 1E-4	
29/10/09 11:29		1.26E-2 ± 5E-4	
29/10/09 12:15	2.85E-2 ± 1E-4		
29/10/09 13:25		5.1E-3 ± 5E-4	
29/10/09 13:59		3.9E-3 ± 4E-4	
29/10/09 16:48		1.61E-3 ± 7E-5	
29/10/09 17:25	3.62E-2 ± 2E-4		
30/10/09 10:44	2.95E-2 ± 1E-4		
30/10/09 12:30	3.10E-2 ± 1E-4		
30/10/09 13:08		3.7E-3 ± 3E-4	

30/10/09 23.25	3.22E-2 ± 1E-4		
31/10/09 00:05		4.14E-3 ± 9E-5	
31/10/09 00:36			3.66E-2 ± 3E-4
31/10/09 01:08		3.58E-3 ± 9E-5	
31/10/09 01:39			3.74E-2 ± 4E-4
31/10/09 02:11		3.52E-3 ± 9E-5	
31/10/09 11:00		6.1E-3 ± 3E-4	
31/10/09 11.31		5.3E-3 ± 3E-4	
31/10/09 12:02		5.0E-3 ± 2E-4	
31/10/09 12.33		4.0E-3 ± 2E-4	
31/10/09 13:05		3.7E-3 ± 2E-4	

Table 2 Summary of the calibration informations on Napoli Lidar system's depolarization sensor for the period from 28 October 2009 to 31 October 2009

Acknowledgments

I really want to tank all the patient people that support me during this three years of PhD studies, a really particular period of my life.

In particular I'd like to thank first of all my tutor, Prof. Nicola Spinelli. He helped me in developing the criticism concerning the methodology, the evaluation and the final expression of the relevant results of my scientific work. I'm also grating to my co-tutor Dr.Xuan Wang for his high quality scientific and practise support and to the coordinator of this PhD cycle, two actually, Prof. Abbate and Prof. Andreone for the precious devices they gave me during the course.

During the first year of my PhD I spent three months period in Bologna to attend two doctoral courses about the physics of the planetary boundary layer, the diffusive processes that occur in atmosphere and the meteorological dynamic.

I was a guest of the C.N.R.-I.S.A.C. (Istituto per le Scienze Atmosferiche e Climatiche), where I developed some meteorological models of the Planetary boundary layer, starting from experimental results used as the input values. For this works I really want to thank Prof. Francesco Tampieri and Dr.Alberto Maurizi.

During the second year of my PhD I worked together with two Chinese PhD students. Their capability in calculus helped me in obtaining reliable results for the simulations, presented in Chapter4.

I'm also grateful to the students that helped me in the various steps of the experimental phase: the rebuilding of the receiving system, the characterization of all the optical components, the pile-up corrections of the PMTs and the data analysis. The alignment procedure of the depolarization sensitive channels also required a lot of work, especially the realization and the calibration of the depolarization sensor.

For the period spent in Potenza I have to thank all the Lidar group, for their support and for the availability of the row data they gave me to calibrate the depolarization sensor of their apparatus.

At the last, but not the least, I'd like to say THANK YOU to my family, that support me from the beginning to the end, especially during the difficult moments.